Methods[1]

Expedition 343/343T Scientists[2]

Chapter contents

[1] Expedition 343/343T Scientists, 2013. Methods. *In* Chester, F.M., Mori, J., Eguchi, N., Toczko, S., and the Expedition 343/343T Scientists, *Proc. IODP,* 343/343T: Tokyo (Integrated Ocean Drilling Program Management International, Inc.). doi:10.2204/iodp.proc.343343T.102.2013
[2] **Expedition 343/343T Scientists' addresses.**

Introduction

This chapter documents the procedures and methods employed in the shipboard work described in the *Expedition Reports* section of the Expedition 343/343T *Proceedings of the Integrated Ocean Drilling Program* volume. Methods for shore-based analysis of Integrated Ocean Drilling Program (IODP) Expedition 343/343T samples and data will be described in individual scientific contributions to be published elsewhere. All shipboard scientists contributed to the completion of this volume.

Numbering of sites, holes, cores, and samples

Sites drilled by the D/V *Chikyu* are numbered consecutively from the first site (drilled by the *Chikyu* during IODP Expedition 314) with the prefix "C" because the site is drilled using the Japan Agency for Marine-Earth Science and Technology (JAMSTEC)/Center for Deep Earth Exploration (CDEX) platform. A site refers to one or more holes drilled while the ship is positioned within 300 m of the first hole, and a letter suffix distinguishes each hole drilled at the same site. The first hole drilled at a given site is assigned the site number modified by the suffix "A," the second hole takes the site number and the suffix "B," and so forth. (Fig. **F1**).

The cored interval is measured in meters below seafloor according to the depth determined by the procedures described in IODP Depth Scales Terminology version 2 (**www.iodp.org/program-policies/**). This depth scale is equivalent to the Ocean Drilling Program (ODP) depth scale meters below seafloor (mbsf). In general, depth below seafloor is determined by subtracting the water depth estimated from the initial drill pipe measurement to the seafloor from the total drill pipe measurement. The depth interval assigned to an individual core begins with the depth below seafloor at which coring began and extends to the depth to which coring advanced. Each coring interval is generally ≤9.5 m, which is the length of a core barrel; however, coring intervals may be shorter.

Cores taken from a hole are numbered sequentially from the top of the hole downward. Core numbers and their associated cored intervals are unique in a given hole. Generally, maximum recovery for a single core is 9.5 m of sediment in a plastic liner (6.6 cm internal diameter) plus ~0.2 m (without a plastic liner) of sediment in the core catcher, a device at the bottom of the core barrel that prevents loss of the core while the barrel is retrieved from the

doi:10.2204/iodp.proc.343343T.102.2013

hole. In certain situations, recovery may exceed the 9.5 m maximum. In soft sediment, this is normally caused by core expansion resulting from depressurization.

Recovered cores are divided into 1.5 m sections that are numbered serially from the top of each core. When full recovery is obtained, these sections are numbered from 1 to 7, with the last section usually being shorter than 1.5 m. When a recovered core is shorter than the cored interval, the top of the recovered core is equated with the top of the cored interval by convention to achieve consistency in handling analytic data derived from the cores. All sections recovered are placed immediately adjacent to each other in the core tray. Samples and descriptions of cores are designated by distance, measured in centimeters from the top of the section to the top and bottom of each sample or interval. By convention, when a core is described, material recovered from the core catcher is placed below the last section and labeled with the suffix "CC." In sedimentary cores, core catcher sections are treated as separate sections. The core catcher is placed at the top of the cored interval when material is recovered only in the core catcher. However, information supplied by the drillers or logging may allow more precise interpretation of the correct position of core catcher material within an incomplete recovered core interval.

Complete sample identification numbers include the following information: expedition, site, hole, core number, core type, and section number, followed by the interval in centimeters measured from the top of the section. For example, the sample identification "343-C0019E-17R-1, 4–7 cm" indicates a 3 cm sample removed from the interval between 4 and 7 cm below the top of Section 1 of Core 17 ("R" designates that this core was taken with the rotary core barrel [RCB]) in Hole E at Site C0019 during Expedition 343.

Core handling

The following sections describe in detail the flow of core from the drill floor through the laboratory. Core handling during Expedition 343 followed the general core flow procedure implemented during recent IODP expeditions on the *Chikyu*. (Expedition 331 Scientists, 2011; Expedition 322 Scientists, 2010). Modifications were made to the core flow when necessary to ensure that core sections of particular interest to the expedition (e.g., principal slip surfaces or zones) were not damaged. The specific core flow for this expedition is illustrated in Figure **F2.**

Core cutting area

Rotary cores were recovered from the drill site in 9.5 m long segments. As soon as the core was retrieved on deck, the core catcher was delivered to the core cutting area. A ~150 cm^3 (~5 cm whole round) sample of material taken from the core catcher was preserved for micropaleontologic analysis, and the rest of the core catcher material was packed into a core liner and entered into the general core flow. Each core segment was then carefully transferred to the core cutting area. The recovered core length and the total length of void space were then measured and entered into the J-CORES database, along with core identification information, drilling advance, and depth information (Expedition 331 Scientists, 2011).

Prior to cutting the core into 1.5 m sections, a visual inspection was made to try to identify structurally important features to avoid cutting directly through lithologic contacts or structures. If a structurally important feature was identified, the locations of divisions between core sections were modified to ensure the structure was not disturbed. The length of the modified sections was ≤1.4 m, the maximum length of core that can be run through the 3-D X-ray computed tomography (CT) scanner (GE Medical System LightSpeed Ultra 16). The core was then cut into sequentially numbered sections. A 5 cm^3 sample was taken from the bottom of the first core section for headspace gas analysis. A 1 cm^3 sample was taken from the bottom of each section to test for the presence of hydrogen gas. Pertinent members of the science party then decided on the preferred order of the X-ray CT scanning, such that sections of the core that appeared to contain enough intact rock to facilitate time-sensitive whole-round core (WRC) sampling for interstitial water, microbiology, and anelastic strain recovery were scanned first.

Core processing deck

Each core section was imaged using the X-ray CT scanner, with priority given to sections containing the proposed time-sensitive WRCs. X-ray CT scans were performed on complete sections, and data were reviewed in real time by the X-ray CT watchdog, a structural geologist, who used the scans to approve the location of each WRC sample. If the watchdog identified a feature of specific interest to the expedition coincident with a proposed WRC location, the core section in question was set aside and a second section from which time-sensitive WRC samples could be taken was scanned. After approval of time-sensitive WRC locations by the X-ray CT watchdog,

these samples were cut for immediate analysis. The remaining core sections were then allowed to rest in order to reach thermal equilibrium with the temperature in the laboratory (~0–1 h, or until core temperature reached ~20°C). Once equilibrium was reached, the sections were scanned for gamma ray attenuation (GRA) density, *P*-wave velocity (PWV), magnetic susceptibility, noncontact resistivity (NCR), and natural gamma radiation (NGR) using the multisensor core logger system (Geotek, Ltd.) for whole-round (MSCL-W) analysis. MSCL-W analysis was conducted at 4 cm intervals for GRA, PWV, magnetic susceptibility, and NCR and at 15 cm intervals for NGR. Core sections possibly containing features of structural interest identified by the X-ray CT watchdog were scanned at the highest resolution possible given time constraints and the length of the core section, up to a maximum resolution of 1 mm for GRA, PWV, magnetic susceptibility, and NCR and 25 mm for NGR. If high-resolution MSCL-W analysis appeared to confirm the presence of a structurally important feature, a structural WRC was cut, sealed, and placed in –4°C storage for separate processing (with advice and consent of the Co-Chief Scientists). The rest of the core was returned to the general core flow.

Following MSCL-W analysis, the X-ray CT and MSCL-W scans were oriented with respect to two longitudinal lines drawn on the core liner that demarcated the working half from the archive half. WRC samples were then taken for analyses that were not time sensitive. After all WRC samples were taken, the core section was split lengthwise along the lines delimiting the archive and working halves, which were then sent for further processing.

Working half

Hard rock thermal conductivity measurements were conducted on the working half of the core. After these measurements, the following time-sensitive physical properties samples were taken as close together as possible:

- ~3–5 cm^3 samples for moisture and density (MAD),
- 8 cm^3 cube for discrete electrical resistivity and discrete PWV measurements, and
- 8 cm^3 cube for elastic wave velocity measurements under high-pressure conditions.

MAD samples were taken once per section; in some cases more samples were taken if the section contained more than one distinct lithology. Cubic samples for resistivity and discrete PWV were taken once per core, depending on core quality. A total of five cubic samples were used for elastic wave velocity measurements under high pressure. The locations of these samples were carefully chosen to ensure they did not coincide with areas of particular structural interest. Visual core description (VCD) of the working half of the core primarily focused on structural geology, although lithologic units of interest were also noted. Members of the science party representing geochemistry, physical properties, core description, microbiology, and paleomagnetism then used the VCD observations to determine discrete sampling locations for

- Spinner magnetometer measurements,
- X-ray fluorescence (XRF) and X-ray diffraction (XRD),
- Carbonate and carbon-nitrogen-sulfur (CNS) analyses,
- Unconfined compressive strength (UCS) and grain size, and
- Personal sample requests.

The samples for XRF and XRD analyses were located as close as possible to the time-sensitive physical properties samples already taken from the core. Once all locations were agreed upon, the samples were taken from the core and processed (for detailed methodologies related to a specific analysis, please refer to the appropriate section below). The working half was then wrapped in plastic film, shrink wrapped, and placed in cold storage (–4°C).

Archive half

Nondestructive digital photo image scanning and color spectrophotometry were carried out on the archive half using the photo image logger (MSCL-I) and the color spectroscopy logger (MSCL-C), respectively (Expedition 331 Scientists, 2011). The archive half was then sent to the core description scientists for visual core description. Description of the archive half focused primarily on lithologic description, but features of possible structural interest were noted so that their complement could be identified in the working half for additional description, measurement, and subsampling, if warranted. Minuscule samples (approximately the amount that could easily be picked up on the end of a toothpick) were taken from the archive half in areas of lithologic interest for smear slide analysis. Selected sections of the archive half were sent back through the X-ray CT scanner to document any structural damage done to the core during core splitting or as a result of desiccation during description. The archive half was then wrapped and sealed following the same procedures described above for the working half.

Logging while drilling

During Expedition 343, three logging-while-drilling (LWD) and measurement-while-drilling (MWD) tools were deployed by Schlumberger Ltd. under contract with Mantle Quest Japan Company Ltd. LWD tools measure in situ formation properties with instruments that are located in special drill collars immediately above the drill bit. LWD measurements are made shortly after the hole is opened with the drill bit and before continued drilling operations adversely affect in situ properties and borehole stability. Fluid invasion into the borehole wall is also reduced relative to wireline logging because of the shorter elapsed time between drilling and taking measurements. MWD tools measure downhole drilling parameters and assure communication between tools. During drilling operations, these measurements are combined with surface rig floor parameters for easier drilling monitoring and quality control (QC). Most LWD data are recorded to downhole memory and retrieved when the tools reach the surface, whereas MWD data and a selection of LWD data are transmitted through the drilling fluid within the drill pipe by means of a modulated pressure wave (mud pulsing) at a rate of 2 bits per second (bps) and monitored in real time. The LWD and MWD tools used during Expedition 343 include several of Schlumberger's VISION series tools, namely geoVISION and arcVISION, in addition to their MWD TeleScope tool. Figure **F3** shows the configuration of the LWD/MWD bottom-hole assembly (BHA). The set of measurements recorded from LWD/MWD tools are listed in Tables **T1** and **T2.**

Systems and tools

Depth tracking system

LWD data interpretation requires specific and precise depth measurements that connect the logging data to formations in the subseafloor. Because LWD tools record data only as a function of time, the Maxwell surface system that is installed on board the *Chikyu* has software that records the time and depth of the drill string below the drill floor, as well as the rate of penetration (ROP).

Accurate and precise depth tracking requires independent measurements of (1) position of the traveling block and top drive system in the derrick; (2) heave of the vessel because of wave action, swells, or tides; and (3) activity of the motion compensator. These measurements are automatically recorded during drilling. The depth of the drill string and ROP are determined from the length of the BHA and drill pipe and the position of the top drive in the derrick. The configuration of these components is illustrated in Figure **F4.**

Measurement while drilling (TeleScope)

MWD was critical to successful drilling during Expedition 343, as it provided real-time two-way communication between LWD tools and the surface and enabled scientists to monitor drilling operations, estimate borehole conditions, and detect a target fault while drilling. The MWD TeleScope tool (Fig. **F5**) transmits real-time measurement data from the MWD tool and selected LWD tools uphole through the drilling fluid (in a process known as mud-pulse telemetry). A list of the real-time LWD/MWD/recorded mode parameters is given in Table **T2.** A modulator in the tool generates a continuous 12 Hz pressure wave within the drilling fluid and changes the phase of this signal (frequency modulation) to transmit the data. Drilling fluid pulses are recorded on two pressure transducers mounted on the standpipe manifold (SPT1) and the gooseneck of the standpipe (SPT2), where they are automatically decoded and uncompressed using the horizon signal processing module (HSPM) and the Maxwell system by the field engineer. The 8¼ inch (21 cm) diameter MWD TeleScope tool was used during Expedition 343. This tool is similar to the PowerPulse but allows data transfer to occur up to 4 times faster by using the Orion II MWD/LWD telemetry platform.

In the MWD fluid pulsing system, pulse rates range from 1 to 12 bps, depending primarily on water depth and fluid density. During Expedition 343, pulse rates of 2 bps were applied for MWD operations because of the ultra-deepwater environment. The TeleScope tool acquires operational and drilling mechanics data, including collar rpm, drilling fluid turbine rpm, stick and slip, and axial and torsional vibration. The TeleScope tool also contains a drilling fluid turbine that powers the entire LWD string when drilling fluid is circulated at a sufficient flow rate (between 300 and 580 gallons per minute or 18–37 L/s in the TeleScope tool in the case of Expedition 343). Additional tool specifications appear in Figure **F5C.**

arcVISION

The arcVISION tool (array-resistivity compensated) (Fig. **F5B**) measures propagation resistivity. Electromagnetic waves are both attenuated and phase-shifted when they propagate in an electrically conductive medium; the degree of attenuation and phase shift depends on the resistivity of the formation (Bonner et al., 1995, 1996). Phase-shift resistivity has relatively high vertical resolution and a shallow depth of investigation, whereas attenuation

resistivity has lower vertical resolution and a greater depth of investigation. The dual-frequency (2 MHz and 400 kHz) array of coils in the arcVISION tool makes 10 phase shifts and 10 attenuation measurements at 5 transmitter-receiver separations of 16, 22, 28, 34, and 40 inches (40.6, 55.9, 71.1, 86.4, and 101.6 cm), which correspond to several depths of investigation (Table T3). For a given frequency, the vertical resolutions of phase-shift resistivities, measured at different transmitter-receiver separations, are similar. In addition to the resistivity tools, arcVISION measures natural gamma radioactivity of the formation. The gamma ray sensor has a measurement range of 0–250 gAPI, with an accuracy of 3% corresponding to a statistical resolution of ±2 gAPI at 100 API and ROP of 30 m/h (Table T4). The arcVISION tool also measures the pressure and temperature of the borehole fluid in the annulus, which are converted to equivalent circulating density (ECD) (density of circulating drilling fluid when pumping). Downhole pressure is a crucial parameter for detecting any inflow from the formation into the borehole or obstruction of the borehole because of collapse of the borehole walls, characterized by an increase in pressure. Monitoring of downhole pressure also allows us to detect pressure decreases associated with loss of circulation to permeable formations or faults.

geoVISION

The geoVISION tool (also known as resistivity at the bit or geoVISION resistivity) provides laterolog-type (focused-resistivity type) resistivity measurements of the formation and high-resolution electrical resistivity images of the borehole wall (Fig. F5A). The tool uses two transmitter coils and a number of electrodes to obtain several measurements of resistivity (Bonner et al., 1996):

- Bit resistivity: the geoVISION tool is connected above the drill bit and uses the lower portion of the tool and the bit as a measuring electrode. This allows the tool to provide a bit resistivity measurement with a vertical resolution of 12–24 inches (30–60 cm). The lower transmitter coil generates a current that flows through the bit and into the formation, returning to the drill collar farther up the tool string. By measuring the axial current through the bit for a given voltage, resistivity near the bit is determined by Ohm's law.
- Ring resistivity: the upper and lower transmitter coils produce currents in the collar that flow out of the tool at the ring electrode. A 1½ inch (3.8 cm) electrode located 129 cm from the bottom of the tool provides a focused lateral resistivity measurement with a vertical resolution of 2–3 inches (5–7.6 cm) and a depth of investigation of ~7 inches (17.8 cm).
- Button resistivity: the same focusing process used in measuring the ring resistivity is applied to determine the resistivity at three 2 inch (5 cm) button electrodes longitudinally spaced along the tool. Button resistivity measurements made as the tool rotates in the borehole are stored and processed to produce a resistivity image of the borehole wall. The button electrodes measure resistivity at three depths of investigation into the borehole wall of ~1, 3, and 5 inches (2.5, 7.6, and 12.7 cm), generating three resistivity images: shallow, medium, and deep. The tool's orientation system uses Earth's magnetic field as a reference to determine the tool position with respect to the borehole as the drill string rotates, thus allowing azimuthal resistivity measurements.

During Expedition 343, the geoVISION tool sampled image data every 10 s. To maintain appropriate sampling intervals matching the vertical resolution of the measurement and record high-quality data to important target depths, the recommended ROP was reduced to 15–20 m/h, or ~5 cm every 10 s, in the interval below 500 mbsf.

The geoVISION tool also contains a scintillation detector that provides an azimuthal total natural gamma ray measurement. The gamma ray sensor has a range of operability of 0–250 gAPI and an accuracy of ±7% corresponding to a statistical resolution of ±3 gAPI at 100 API and an ROP of 30 m/h. Its depth of investigation is between 5 and 15 inches. Gamma ray measurements are acquired at 90° resolution as the geoVISION tool rotates. See Table T5 for further geoVISION specifications.

Shipboard data flow and quality check

For each LWD/MWD operation, two types of data were collected: (1) real-time data that include all MWD data and selected LWD data and (2) LWD data recorded downhole and stored in the tool's memory. Data are originally recorded downhole at a preset sampling interval, and no depth information is recorded in the tool. The depth-referenced version is obtained after merging the time (downhole) with the time-depth relationship recorded on the surface by the Maxwell system. All the depth-converted data for LWD/MWD are provided in digital log information standard (DLIS) format by the field engineers.

After determining the position of the mudline on the gamma ray log, all logging data were depth shifted to the seafloor (LWD depth below seafloor [LSF]). The depth-shifted versions of the LWD/MWD data are available in DLIS format, and the main sca-

lar logs were extracted and converted into log ASCII standard (LAS) files. All files were distributed to the shipboard scientists through the shipboard intranet data servers. Analyses, integration results, and reports produced by the shipboard scientists were archived on the server for further distribution. The geoVISION resistivity image data were processed on board the *Chikyu* using Schlumberger's GeoFrame (version 4.4) software package and imported into GeoMechanics International's GMI and Paradigm's Geolog software for further structural analysis. Normal data flow is illustrated in Figure F6.

Logging staff scientists used drilling control logs to identify the sequence of drilling events and assess any possible impact on data quality. Drilling control logs include drilling surface parameters (e.g., ROP, surface weight on bit [SWOB], hook load [HKLD], and standpipe pressure [SPPA]) and downhole drilling parameters (e.g., collar [bit] rotation [CRPM], hole deviation [HDEVI], radial shock rate [SKR_R], tangential shock rate [SKR_T], shock peak [SHKPK], and stick-slip indicator [SLIP]). Elapsed time of the main geophysical measurements after bit penetration, including annular pressure and temperature logs, were also assessed to identify any anomalous zones. Tool rotation was also checked; it must be higher than null and lower than 250 rpm to allow good quality azimuthal measurements and associated images. In zones of high stick-slip, even if CRPM is set to a typical value of 100 rpm, it can greatly vary locally (and exceed 250 rpm), resulting in lower quality images.

Log characterization and lithologic interpretation

LWD measurements provide in situ petrophysical information on sediment, rock, and pore fluids while the hole is being drilled. These measurements are sensitive to changes in composition, texture, and structure. Changes in the log response are commonly associated with geological unit boundaries. This section addresses the characterization of LWD measurements and imaging tool response, focusing on dividing the well logs into log units. Once representative petrophysical properties for the log units were defined, they were incorporated in the log-based lithologic units. For Expedition 343, the aim was to provide a preliminary assessment of expected lithostratigraphy from LWD data prior to coring.

Log characterization and identification of log units: qualitative analysis

The LWD logs were separated into log units by qualitative examination of the log responses and downhole trends: the variation in log shape and magnitude, peak amplitude and frequency, as well as thorough examination of the image logs. Natural radioactivity, resistivity, and borehole images were the main input logs for determining unit boundaries. In addition to defining and characterizing the log units, the logging team identified any compositional features/variation within each unit and interpreted them in terms of geological features (unit boundaries, transitions, sequences, and likely lithologic composition).

Log-based geological/lithologic interpretation

After log characterization and classification, logs were lithologically and geologically interpreted using a combination of log characteristics and borehole images for Site C0019. Compositionally influenced logs, such as NGR, were used to determine unit-scale to bed-scale lithology. In particular, the identification of sand-rich intervals, clay-rich intervals, or alternating beds of sand and clay was a primary element of the interpretation. Resistivity logs were used to identify lithologies with different physical properties, such as mudstone and chert. Borehole images provided useful information on mesoscopic features, such as bedding, sedimentary structures, bed boundaries, and faults. Ground-truthing of these interpretations was done by correlation with core data from Hole C0019E.

Physical properties and hydrogeology

Resistivity logs provide information on in situ physical properties at scales of tens of centimeters to tens of meters and are used to infer the porosity and density of rocks in the absence of other measurements. Comparison of the deep and shallow buttons also provides indications on the permeability of the formations. This data set provides important information for the characterization of lithologic units, deformation, states of consolidation, and hydrogeologic conditions. It is also used to correlate core, seismic, and downhole log data. We present the logs as a function of depth and describe their features and variation, taking into account information from the gamma ray log, structural geology, and seismics. Sharp variations in physical properties are of particular interest, as they can be indicators of a fault zone and its activity. We derived an estimated porosity from the resistivity logs and an estimated density from the estimated porosity. The different parameters used to compute these logs were adjusted by comparing them with values measured on recovered cores.

Estimation of temperature profile

The downhole temperature (T) was calculated using a constant thermal conductivity (TC) of 1.1 W/(m·K) and a surface heat flow (HF) of 45 mW/m² as documented in Yamano et al. (2008). The calculation is based on the following law:

$$T = \mathrm{HF/TC} \times Z + \mathrm{T_0}, \quad (1)$$

where a surface temperature (T_0) of 1.3°C was used based on measurements made with temperature sensors (see **"Observatory and downhole measurements"**) and Z is the depth below seafloor.

Estimation of porosity from resistivity logs

We used Archie's law to derive a porosity (ϕ) log from the resistivity:

$$F = 1/\phi^m, \quad (2)$$

where F is the formation factor and m is the so-called cementation factor. The cementation factor depends on rock type and is more closely related to texture than to cementation. This value was calibrated using the core measurements.

The formation factor was calculated as

$$F = R/R_f, \quad (3)$$

where R is the LWD measured deep resistivity and R_f is the fluid resistivity. We used the deep resistivity measurement here because it has a penetration depth sufficiently large to minimize the effects of seawater invasion. We assumed that the pore fluid was similar to seawater. The formula used to calculate the seawater resistivity (σ_f) as a function of the temperature (in °C) is described by Bourlange et al. (2003):

$$\sigma_f = 5.32 \times [1 + 0.002 \times (T - 25)]. \quad (4)$$

Estimation of density from the porosity log

An estimated bulk density (ρ_b) log was calculated from the estimated porosity log using the following equation:

$$\rho_b = \phi(\rho_w - \rho_g) + \rho_g, \quad (5)$$

where

ϕ = porosity,
ρ_g = grain density, and
ρ_w = water density.

We assumed a constant grain density (ρ_g) of 2.50 g/cm³ and a constant water density (ρ_w) of 1.024 g/cm³. This grain density value is in good agreement with measurements made on cores recovered from the deep-sea terrace of the Japan Trench (Sacks, Suyehiro, Acton, et al., 2000).

Structural analysis: bedding, fractures, and faults

Structural analysis was performed primarily on geoVISION resistivity images using GMI Imager (GeoMechanics International Inc.) software. This software package presents resistivity image data of the borehole wall as a planar "unwrapped" 360° image. The software also allows visualization of the data in a 3-D borehole view alongside correlative log curve data. The orientation of planar surfaces cutting the borehole (bedding, fractures, and faults) is defined by fitting a sinusoid to the unwrapped image. In identifying bedding, care must be taken to avoid horizontal artifacts caused by problems in data acquisition that appear as sharp horizontal lines. We distinguished fractures and faults from bedding by looking for crosscutting relationships between the faults and fractures and the bedding. Where crosscutting relationships were absent, we looked for contrasting orientations between the faults and fractures and the bedding. The fractures and faults were classified as to whether they were conductive, resistive, or undetermined/unclassified. Where resolved, the thickness of faults and fractures was noted. Rare offsets of preexisting faults or bedding allows some faults to be identified as normal, strike-slip, or reverse. The software records the data and displays plots of these features.

Borehole wall failure analysis

Borehole breakouts and tensile fractures are two types of drilling-induced borehole wall failure that form when the state of local stress field at the borehole wall exceeds rock/sediment strength (Zoback, 2007). In a vertical borehole, breakouts form along the borehole in the direction of the minimum horizontal stress (S_{hmin}) and perpendicular to the maximum horizontal stress (S_{Hmax}). Breakouts are recorded in resistivity images as two parallel conductive vertical features 180° apart. Drilling-induced tensile fractures (DITFs) may form in conjunction with breakouts or independently. DITFs form perpendicular to S_{hmin}, 90° from the azimuth of the breakouts. DITFs occur when the hoop stress, or the stress tangent to the circumference of the borehole wall, exceeds rock tensile strength (in terms of absolute value of stress). Where the tensile strength of sediment is negligible, the occurrence of DITFs is an indicator of tensile hoop stress at the borehole wall. We recorded the orientation and width of breakouts with the available image analysis software (all three borehole im-

ages [shallow, medium, and deep] were considered) and determined the maximum and minimum horizontal stress orientations. We compared breakout distribution and width observed and measured on electrical images with lithology derived from all log data and drilling parameters.

Finding faults

The principal goal of this expedition was to sample and instrument the fault zone associated with the Tohoku-oki earthquake. Although the borehole is located so that it crosses the fault zone, we must determine the depth of intersection from analysis of log data. The protocol used for locating this fault is detailed in the following sections.

Conductive and resistive faults and fractures and resistive structures

A conductive fracture or fault is indicative of a low-density, fluid/seawater-rich feature that could represent a young fracture or fault. Resistive structures are indicative of a collapsed fabric with lower fluid/seawater content than the surrounding rocks. Either a conductive fracture or a resistive structure could represent something that formed recently and is still dilated (conductive) or has collapsed (resistive). Irregular masses of high conductivity associated with horizontal planar high-conductive intervals have been interpreted as hydrofracture zones (Chang et al., 2010).

Patterns of bedding, fractures, faults, and breakouts

Changes in the abundance and orientations of bedding, small-scale fractures and faults, and breakouts may be indicative of a major fault zone in the logged section. Faults, especially weak faults, can produce discontinuities in the fault-parallel components of normal stress that result in changes in the orientation and development of minor structures. Borehole breakout patterns are especially useful in identifying abrupt changes in stress associated with faults (Saffer, McNeill, Byrne, Araki, Toczko, Eguchi, Takahashi, and the Expedition 319 Scientists, 2010), as breakouts provide information on the in situ stress at the time the hole is drilled. In contrast, faults and fractures may record present or past stress conditions.

Log curve data

Variations in geophysical properties measured by logging are commonly associated with fault zones. For example, fracturing of the rock can decrease the resistivity because of the greater content of conductive fluid. In addition, faults with large displacement can incorporate or juxtapose contrasting rock types, which can be apparent in resistivity and gamma ray logs.

Drilling parameters

Faults can be characterized by fluid flow (Vrolijk et al., 1991), which may be sensed by annular pressure while drilling (APWD) and annular temperature while drilling measurements. Torque may also increase in fault zones where material has fallen into the annulus, restricting rotation. Faults create loose material; moreover, flow from fluids can encourage spalling of this material, which when introduced into the borehole can increase torque.

Lithology

Visual core descriptions

We followed conventional ODP and IODP procedures for recording sedimentologic information on a section-by-section basis using VCD forms (Mazzullo and Graham, 1988; Mazzullo et al., 1988). Core descriptions were transferred to section-scale templates using the J-CORES database software and then converted to core-scale descriptions using Strater software.

The previous drilling record in the Japan Trench area suggested we would encounter hemipelagic to pelagic siliciclastic sediment with various admixtures of siliceous microfossils and volcaniclastic material (Scientific Party, 1980). Accordingly, we adopted a sedimentologic classification scheme specific for this area that could be applied with reasonable accuracy by shipboard personnel.

Expedition 343 sedimentary classification focuses on siliciclastic, siliceous microfossil, and volcaniclastic components. Pebbles, fossils, concretions, and nodules were logged as lithologic accessories except where pebbles (>2 mm) make up a significant component of a bed, in which case the bed was logged as gravel. Classification schemes for siliciclastic, siliceous microfossil, and volcaniclastic sediment are presented in Figure **F7.** Similar to the methodology of the Expedition 308 Scientists (2006), we modified the classification of Shepard (1954) to describe the texture of the <0.2 mm siliciclastic components of the sediment, with the division between sand and silt at 64 µm and between silt and clay at 4 µm. These classifications are driven by the principal component, siliceous microfossils or volcaniclastic sediment, with modification as necessary by a secondary component. In our modified classification scheme, sediment identified as ashy mud, ashy clay, ashy silt, and ashy silty sand are grouped into the ashy mud

log unit. Likewise, sediment identified as siliceous mud, siliceous clay, siliceous silt, and siliceous silty sand are grouped into the siliceous mud log unit. Slope deposits may be mixed because of mass transport; where such synsedimentary deposits were unambiguously identified in the core, the intervals were logged as "sedimentary breccia."

Consistency between operators and across the two work shifts was maintained throughout the operation. The initial core was examined by all X-ray CT, sedimentology, and structural geology scientists, and agreement was reached as to the initial descriptive framework. At each shift change, the departing scientists reported their findings from that day and detailed new features and interpretations to be adopted in the future. The working nomenclature was then updated at the beginning of each shift following the meeting.

The graphic lithology column on each VCD form plots to scale all beds that are at least 2 cm thick. Interlayers that are <2 cm thick are identified as laminae and are represented by graphic symbols in the sedimentary structures column instead of lithologic units in the graphic lithology column. Figure F8 displays all the graphic patterns used to represent the sedimentary lithologies and sedimentary structures encountered during Expedition 343. Also shown are the symbols for internal sedimentary structures and accessories, soft-sediment deformation structures, bioturbation, and severity of core disturbance in sedimentary rock (see **"Structural geology"** for a description of drilling disturbance). The graphic lithology column follows the sedimentary classification above. Bioturbation intensity in deposits was noted as light (bedding preserved), moderate (bedding disturbed), or heavy (bedding obliterated).

The description of lithology necessarily overlapped with the structural description, particularly in cases where deformation fabrics (either sedimentary, tectonic, or drilling induced) formed an essential defining characteristic of the rock type. See **"Structural geology"** for a discussion on the terminology for deformation fabrics that may be primary or secondary (e.g., breccia texture and scaly fabrics).

Smear slides

The archive half of the core was sampled near the top and base of each core, as well as at regular intervals and at changes in lithology or areas of particular interest for smear slide analysis. Smear slides are useful for identifying and reporting basic sediment attributes (texture and composition), but the results are not quantitative. We estimated the abundances of biogenic, volcaniclastic, and siliciclastic constituents with the help of a visual comparison chart (Rothwell, 1989), recognizing that smear slide analysis involves multiple sources of error. Sand-sized particles may be underrepresented because of loss in smear slide preparation, and it is difficult to quantitatively estimate the grain size of fine fractions. Thus, it would be misleading to report values as absolute percentages. Instead, our descriptive results are reported as visual percentage estimates with values grouped into the following range categories:

D = dominant (>60%).
A = abundant (>30%–60%).
C = common (>5%–30%).
P = present (>1%–5%).
R = rare (0.1%–1%).
T = trace (<0.1%).

The relative abundance of major components was also validated by XRD (see **"X-ray diffraction"**).

The sample location for each smear slide was entered into the J-CORES database with a sample code of "SS" using the Samples application. The position of each sample is shown on the VCD slide editor column of the VCD application. We tabulated data in an Excel spreadsheet because data entry into the J-CORES database is prohibitively time consuming and the program will not accept ranges of values for individual compositional categories.

X-ray diffraction

We completed routine bulk powder XRD analyses using a Philips PANalytical CubiX PRO (PW3800) diffractometer. The principal goal was to identify mineral phases in the samples and estimate spatial trends in sediment composition. Most of the samples were selected from intervals adjacent to whole-round samples, and most are part of sampling clusters with associated physical properties and carbonate analysis. A few additional samples were collected periodically from where less frequent or unexpected lithologies were encountered, such as volcanic ash. Samples were freeze-dried, crushed with a ball mill, and mounted as randomly oriented bulk powder. The instrument settings were as follows:

Generator = 40 kV and 45 mA.
Tube anode = Cu.
Wavelength = 1.54184 Å (CuKα).
Step spacing = 0.01°2θ.
Rate = 1.0 s/step.
Slits = automatic.
Measuring diameter = 10 mm.
Scanning range = 2°2θ to 60°2θ.

We used Panalytical X'Pert software for data processing. Bulk powder XRD data were used to assist with core-log integration.

The modal mineralogy of the sediment was estimated from bulk powder XRD spectra using a least-squares best-fit approach. Reference spectra for curve matching were restricted to four spectra (quartz, plagioclase, calcite, and total clay), following the methods employed during IODP Expedition 316 (Expedition 316 Scientists, 2009a). These reference spectra were selected and calibrated to the known sediment compositions for Expedition 316, and the applicability of the same reference spectra for Expedition 343 samples is untested. Therefore, we report only general approximations of the relative proportional mineralogy. These approximations also do not allow for detection of other known components of the sediment, such as glass or alkali feldspar from volcanic sources or opaline biogenic silica, and therefore should be considered to be upper bounds.

X-ray fluorescence

Whole-rock quantitative XRF spectrometry analysis was undertaken on core samples for the major elements. Samples of 10 cm^3 were taken from the working half of the core next to samples for XRD and carbonate analysis. Samples were freeze-dried, crushed with a tungsten ball mill, and fused with 4.5 g of SmeltA12 flux for 7 min at 1150°C to create glass beads. Loss on ignition was measured using weight changes by heating at 1000°C for 3 h. Analyses were performed on the wavelength dispersive XRF spectrometer Supermini (Rigaku) equipped with a 200 W Pd anode X-ray tube at 50 kV and 4 mA.

Major elements were measured using the fused-glass bead method and are presented as weight percent oxide proportions (Na_2O, MgO, Al_2O_3, SiO_2, P_2O_5, K_2O, CaO, TiO_2, MnO, and Fe_2O_3). Processed data were uploaded into the J-CORES database as a comma-delimited data file. Data are reported as total counts on the peak and as semiquantitative oxide weight percents.

X-ray fluorescence scanning

Whole-rock semiquantitative XRF spectrometry analysis was undertaken for major elements and trace elements on core material (Na, Mg, Al, Si, P, S, K, Ca, Ti, V, Cr, Mn, Fe, Cu, Ni, Zn, and Zr) in small targeted areas of the core, focusing on unconformities, veins, cemented and altered intervals, or shear surfaces. Semiquantitative element scanning of core sections was undertaken using the onboard JEOL TATSCAN-F2 energy dispersive spectrometry (EDS)-based split-core scanner equipped with a cryogenic Si semiconductor and a 76 mm beryllium window (Sakamoto et al., 2006). The target for the X-ray generation is rhodium, which can generate X-rays with five times higher intensity compared to the standard EDS-based scanner. A rock standard (JSd-2) of the National Institute of Advanced Industrial Science and Technology (Geological Survey of Japan [GSJ]) was used as the reference material for semiquantitative analysis. Table **T6** lists the results and standard deviations for the standard sample.

The diameter of the collimator that detects the incident X-ray beam is 0.8 mm, and the penetration depth on the sample is ~1.1 mm. Although the distance between the sample surface and detector critically affects the intensity of X-rays, XRF scanning is a highly useful, albeit nonroutine, element of shipboard analysis.

Split-core digital photography

The Geotek MSCL-I (with Geoscan IV line-scan imaging camera) was used to capture continuous digital imagery of the archive half for analysis and description. The line-scan system for split-core imaging reduces the optical distortion from the lens or variations of lighting downhole. The camera is a three charge–coupled device system where a light reflected from the sample surface passes through the lens and is split into three paths (red, green, and blue) by a splitter beam in the camera. The camera provides 16-bit red-green-blue (RGB) color TIFF formatted images with a spatial resolution of 100 pixels/cm.

The MSCL-I was used shortly after core splitting in an effort to avoid time-dependent color changes resulting from sediment drying and oxidation. Cores were prepared by careful removal of bumps and dust on the split core face. Camera calibration was performed using Spectralon (SRS-99; Labsphere), a high diffuse reflectance material for white calibration, and a gray card (miniature gray-scale card) consisting of white, 18% gray, and black. A QC measurement was performed before each sample, after the white/black calibration, and after 24 h of routine work.

Working information about the measurements was logged in the measurement log sheet (MLS). These data included core/type/section, date, operator, aperture, curated length, section length, section length + 7 cm, the J-CORES database operator, and shared folder. Scanned images and data were uploaded to the J-CORES database so that image files could be observed through the Composite Log Viewer. Available files included the original high-resolution image with gray-scale and ruler, as well as reduced JPEG images cropped to show only the section-half surfaces. All measurement data, calibration data, setup files, and MLSs were archived to the shared folder on board.

Structural geology

X-ray computed tomography

X-ray CT imaging provided real-time constraints for the core logging and sampling strategies of Expedition 343. The following explanation of our methods was derived from the laboratory measurement manual (X-ray CT Scanner, version 3.00, 31 July 2007) prepared by CDEX/JAMSTEC for shipboard use. The laboratory measurement manual is based on GE Healthcare (2006), Mees et al. (2003), and Nakano et al. (2000).

The X-ray CT instrument on the *Chikyu* is a GE Yokogawa Medical Systems LightSpeed Ultra 16 capable of generating sixteen 0.625 mm thick image slices every 0.5 s, the time required for one revolution of the X-ray source around the sample (see Table **T7** for operating parameters). As a result of the high scanning rate, 1.5 m sections of core were typically imaged in <3 min. Data generated for each core consist of core axis–normal planes of X-ray attenuation values with dimensions of 512 × 512 pixels, with the size of each pixel being 0.188 mm × 0.188 mm. Data were stored as Digital Imaging and Communication in Medicine (DICOM) formatted files.

Background

X-ray intensity (I) varies as a function of X-ray path length and the linear attenuation coefficient (LAC) of the target material as

$$I = I_0 \times e^{-\mu l}, \quad (6)$$

where

I = transmitted X-ray intensity,
I_0 = initial X-ray intensity,
μ = LAC of the target material, and
l = X-ray path length through the material.

LAC is a function of chemical composition and density of the target material. The basic measure of attenuation, or radiodensity, is the CT number given in Hounsfield units (HU) and is defined as

$$\text{CT number} = [(\mu_t - \mu_w)/\mu_w] \times 1000, \quad (7)$$

where μ_t is the LAC for the target material and μ_w is the LAC for water.

The distribution of attenuation values mapped to an individual slice comprises the raw data that are used for subsequent image processing. Successive 2-D slices yield a representation of attenuation values in 3-D pixels, referred to as voxels. Visualizations are generally accomplished by varying the manner in which the distribution of CT numbers is assigned to 256 shades of gray, or a color palette. In general, high CT numbers correspond to bright colors in CT images, representing relatively high bulk density (low porosity) or increase in elements (e.g., Fe) of high atomic number. Onboard analysis of CT images was made using both the Advantage Workstation (Lightspeed Ultra 16, General Electric Medical Systems) and the OsiriX v.2.7.5 32-bit DICOM viewer running on a Macintosh (OSX 10.6).

Analytical standards used during Expedition 343 were air (CT number = –1000), water (CT number = 0), and aluminum (2477 < CT number < 2487) in an acrylic core mock-up. All three standards were run once daily after air calibration and once each week both before and after air calibration. For each standard analysis, the CT number was determined for a 24.85 mm² area at fixed coordinates near the center of the cylinder.

X-ray CT scan data usage

X-ray CT scans were used routinely during Expedition 343 to

- Provide an assessment of core recovery and liner integrity for drilling operations;
- Determine the appropriate locations for whole-round sampling;
- Provide the only data archive of core sections that were taken for whole-round samples prior to VCD;
- Identify the location of subtle features that warrant detailed study and special handling during VCD and sampling;
- Support VCD in real time through display on one of the computers in the core description lab;
- Determine 3-D geometry, cross-cutting, and other spatial relations and the orientation of primary and secondary structures; and
- Distinguish drilling-induced breccia from tectonic breccia (described later).

All WRC sections were screened during X-ray CT scan observation to avoid destructive testing on core samples that might contain critical structural features. Screening also ensured selection of whole-round samples with minimal drilling disturbance (essential for microbiology, inorganic geochemistry, and physical and mechanical properties) and provided an assessment of whole-round homogeneity. X-ray CT scanning was done immediately after core cutting so that time-sensitive whole-round samples (e.g., those for interstitial water and microbiological analyses) could be included in this screening process.

Fractures and other planar features that could be identified in the X-ray CT scans were oriented directly from the imagery by measuring strike in the slice view (perpendicular to the core axis) and one or

more apparent dips in axial sections (e.g., coronal and sagittal) (Fig. F9). X-ray CT scanning helped reveal features that were cryptic or indistinguishable during VCD.

X-ray CT scans proved to be useful for identifying sedimentary and tectonic features prior to visual core description. 3-D structure orientation in the core reference frame could easily be determined from CT scan sections, whereas performing the same measurement on the cores generally required cutting orthogonal faces. Furthermore, structures such as shear zones could be classified by contrast in CT number, which is likely related to porosity changes or chemical alteration within shear zones. Structural and stratigraphic observations are incorporated into the structural geology and lithostratigraphy sections.

X-ray CT scan data have multiple uses, from early assessment of cores to description and synthesis. For this reason, several hundred gigabytes of scan data (~825 Mb/m) were stored on a local database at the OsiriX interpretation station. These data were later archived to tape and stored on terabyte disks.

Visual core description

Our methods for documenting the structural geology of Expedition 343 cores largely followed those given by the Expedition 316 structural geologists (Expedition 316 Scientists, 2009a). We documented the deformation observed in the split cores by classifying structures, determining the depth extent, measuring orientation, and recording kinematic information. The collected data were hand-logged at the core table and then entered into both a local spreadsheet and the J-CORES database. Where possible, the orientation data were also corrected for rotation related to drilling on the basis of paleomagnetic declination and inclination information.

Core description and orientation data collection

Each structure was recorded manually on a structural description sheet, which was modified from that used during IODP Expedition 322 (Fig. F10). We found that this modified sheet was particularly useful in recording orientation data for linear structures (e.g., striations on fault planes). Core measurement protocols followed those employed during Expedition 316, which were in turn based on previous ODP procedures developed at the Nankai accretionary margin (i.e., ODP Legs 131 and 190). We used a plastic protractor for orientation measurements (Fig. F11). Structural measurements were made on the working half of the split core, which provided greater flexibility to remove and cut (if necessary) pieces of the core for more careful study and measurement.

Orientations of planar and linear features in cored sediment were determined relative to the core axis, which was vertical in the core reference frame, and the "double line" marked on the center of the working half of the split core liner, which was 0° in the core reference frame. To determine the orientation of a plane, two apparent dips of the planar feature were measured in the core reference frame and converted to a plane orientation given as either a strike-and-dip or a dip-and-dip direction using a spreadsheet (Fig. F12). This approach had the advantage of increasing data processing efficiency and reducing errors in transferring and retyping data (e.g., by using both R. Allmendinger's Stereonet program [www.geo.cornell.edu/geology/faculty/RWA/programs.html] and a spreadsheet). One apparent dip was typically represented by the intersection of the planar feature with the split face of the core and quantified by measuring the dip direction and angle in the core reference frame. Typical apparent dip measurements had a trend of 90° or 270° and ranged in plunge from 0° to 90°. The second apparent dip was usually represented by the intersection of the planar feature and a cut or fractured surface at a high angle to the split face of the core axis. In many cases, the cut surface was either parallel or perpendicular to the core axis. In the former case, the apparent dip lineation would trend 000° or 180° and plunge from 0° to 90°, whereas in the latter case, the trend would range from 000° to 360° and plunge 0°. Linear features observed in the cores were always associated with planar structures (typically faults or shear zones), and their orientations were determined by measuring either the trend and plunge in the core reference frame or the rake (or pitch) on the associated plane. All of these data were recorded on the log sheet with the appropriate depths and descriptive information.

Rotations were induced during RCB coring, as is common in ocean drilling. Paleomagnetic data were used routinely to correct drilling-induced rotation of the cored sediment. The new cryogenic magnetometer was not installed on the *Chikyu* until after Expedition 343, so paleomagnetic correction was conducted using the spinner magnetometer.

Orientation data analysis based on the spreadsheet

During Expedition 343, we adopted the modified Expedition 322 spreadsheet template for orientation data calculation in the core reference frame (e.g., Fig. F12). The core reference frame was such that the top of the core was oriented vertically upward, the core-

splitting plane was 90°/270° and vertical, and the double-lined side of the working half of the core liner pointed toward 0° (Fig. F9).

Calculation of plane orientation

For planar structures (e.g., bedding or faults), two apparent dips on two different surfaces (e.g., one being the split core surface, which is 90°–270° and vertical, and the other being the 0°–180° vertical surface) were measured in the core reference frame as azimuths (measured clockwise from 0°, looking down) and plunges (Fig. F13). An xyz coordinate system was defined in such a way that the positive *x*-, *y*-, and *z*-directions coincided with 0°, 90°, and vertical downward, respectively (Fig. F9). If the azimuths and plunges of the two apparent dips were given as (α_1, β_1) and (α_2, β_2), respectively, as in Figure F13, then the unit vectors representing these two lines, v_1 and v_2, were

$$v_1 = \begin{pmatrix} l_1 \\ m_1 \\ n_1 \end{pmatrix} = \begin{pmatrix} \cos\alpha_1 \cos\beta_1 \\ \sin\alpha_1 \cos\beta_1 \\ \sin\beta_1 \end{pmatrix} \quad (8)$$

and

$$v_2 = \begin{pmatrix} l_2 \\ m_2 \\ n_2 \end{pmatrix} = \begin{pmatrix} \cos\alpha_2 \cos\beta_2 \\ \sin\alpha_2 \cos\beta_2 \\ \sin\beta_2 \end{pmatrix}, \quad (9)$$

where *l*, *m*, and *n* represent the *x*-, *y*-, and *z*-components of the vectors.

The unit vector normal to this plane (v_n) (Fig. F13) was then defined as follows:

$$v_n = \begin{pmatrix} l_n \\ m_n \\ n_n \end{pmatrix} = \frac{v_1 \times v_2}{|v_1 \times v_2|}, \quad (10)$$

where

$$v_1 \times v_2 = \begin{pmatrix} \begin{vmatrix} m_1 & m_2 \\ n_1 & n_2 \end{vmatrix} \\ \begin{vmatrix} n_1 & n_2 \\ l_1 & l_2 \end{vmatrix} \\ \begin{vmatrix} l_1 & l_2 \\ m_1 & m_2 \end{vmatrix} \end{pmatrix} = \begin{pmatrix} m_1 n_2 - m_2 n_1 \\ n_1 l_2 - n_2 l_1 \\ l_1 m_2 - l_2 m_1 \end{pmatrix}. \quad (11)$$

The azimuth (α_n) and plunge (β_n) of v_n were given by

$$\alpha_n = \tan^{-1}(m_n/l_n) \quad (12)$$

and

$$\beta_n = \sin^{-1} n_n. \quad (13)$$

The dip direction (α_d) and dip angle (β) of this plane were α_n and 90° + β_n, respectively, when $\beta_n < 0°$ (Fig. F14A). They were $\alpha_n \pm 180°$ and 90° – β_n, respectively, when $\beta_n \geq 0°$ (Fig. F14B). The right-hand rule strike of this plane (α_s) was then given by α_d – 90° (Fig. F14).

Calculation of slickenline rake

For a fault with slickenlines, the apparent rake angle of the slickenline (ϕ_a) was measured on the fault surface from either the 90° or 270° direction of the split core surface trace (Fig. F15). Fault orientation was measured as described above. Provided that v_n and v_c were unit vectors normal to the fault and split core surfaces, respectively, the unit vector of this intersection line (v_i) was perpendicular to both v_n and v_c and therefore defined as follows:

$$v_i = \begin{pmatrix} l_i \\ m_i \\ n_i \end{pmatrix} = \frac{v_n \times v_c}{|v_n \times v_c|}, \quad (14)$$

where

$$v_c = \begin{pmatrix} 1 \\ 0 \\ 0 \end{pmatrix} \quad (15)$$

and

$$v_n \times v_c = \begin{pmatrix} \begin{vmatrix} m_n & 0 \\ n_n & 0 \end{vmatrix} \\ \begin{vmatrix} n_n & 0 \\ l_n & 1 \end{vmatrix} \\ \begin{vmatrix} l_n & 1 \\ m_n & 0 \end{vmatrix} \end{pmatrix} = \begin{pmatrix} 0 \\ n_n \\ -m_n \end{pmatrix}. \quad (16)$$

Knowing the right-hand rule strike of the fault plane (α_s), the unit vector (v_s) toward this direction was then

$$v_s = \begin{pmatrix} \cos\alpha_s \\ \sin\alpha_s \\ 0 \end{pmatrix}. \quad (17)$$

The rake angle of the intersection line (ϕ_i) measured from the strike direction was given by

$$\phi_i = \cos^{-1}(v_s \times v_i) \quad (18)$$

because

$$v_s \times v_i = |v_s||v_i|\cos\phi_i = \cos\phi_i, \ \therefore |v_s| = |v_i| = 1. \quad (19)$$

The rake angle of slickenline (ϕ) from the strike direction was $\phi_i \pm \phi_a$, depending on which direction the apparent rake was measured from and which direction the fault plane dips toward. ϕ_a was subtracted from ϕ_i when the fault plane dipped toward 270° and ϕ_a was measured from either the top or 090° direction (Fig. F16A) or when the fault plane dipped toward 90° and ϕ_a was measured from either the bottom or 090° direction (Fig. F16B). Conversely, ϕ_a was added to ϕ_i when the fault plane dipped toward 90° and ϕ_a was measured from either the top or 270° direction (Fig. F16C) or when the fault plane dipped toward 270° and ϕ_a was measured from either the bottom or 270° direction (Fig. F16D).

Azimuth correction based on paleomagnetic data

Provided that a core was vertical, its magnetization was primary, and its bedding was horizontal, its paleomagnetic declination (α_p) represented the magnetic north direction where its inclination (β_p) was ≥0° (Fig. F17A), whereas it represented the magnetic south direction where $\beta_p < 0°$ (Fig. F17B). The dip direction and strike of a plane in the geographic reference frame (α_d* and α_s*) therefore were

$$\alpha_d^* = \alpha_p - \alpha_d \quad (20)$$

and

$$\alpha_s^* = \alpha_p - \alpha_s, \quad (21)$$

where

$$\beta_p \geq 0° \quad (22)$$

and were

$$\alpha_d^* = 180° + \alpha_p - \alpha_d \quad (23)$$

and

$$\alpha_s^* = 180° + \alpha_p - \alpha_s, \quad (24)$$

where

$$\beta_p < 0°. \quad (25)$$

J-CORES structural database

Structural data were entered in the J-CORES database VCD program (Fig. F18). These data include a visual (macroscopic and/or microscopic) description of core structures at a given section index and a record of planar structures in the core reference frame. We recorded the data first on paper logs and then transferred the data into the J-CORES database at a later time. Data were also entered into a spreadsheet (Fig. F12) for postacquisition processing.

Data entry through the VCD program proceeded as follows:

1. We recorded the expedition, site, hole, core, and section for which data were going to be read/written.
2. We selected the data to work with (i.e., deformation structure description), clicked on Hire, and then OK.
3. We selected a structure ID (e.g., bedding, fault, etc.) or created a new structure ID, selected the section interval in which the structure was observed, and filled in the parameters related to the particular structure (e.g., comments and planar data) (Fig. F18).

After saving, data were automatically uploaded to the *Chikyu* server and could be retrieved afterward as text or an Excel file for further processing.

Description and classification of structures

In general, we described and classified the structures observed using the terminology of J-CORES and Expedition 316, which in turn was based on the J-CORES VCD scheme and ODP Legs 131 (Taira, Hill, Firth et al., 1991), 156 (Shipley, Ogawa, Blum, et al., 1995), 170 (Kimura, Silver, Blum, et al., 1997), and 190 (Moore, Taira, Klaus, et al., 2001). However, for clarity we define the terminology used to describe fault-related rocks, as well as the basis for differentiating between natural and drilling-induced features and interpreting formation by gravitational or tectonic processes below.

Deformed sediment and rocks

Breccia is composed of fragments that have clearly rotated with respect to each other. The presence of a matrix may be difficult to ascertain because of pervasive intrusion of this incohesive material by drilling mud or washing away by circulating fluids near the core surface. Brecciated fragments are typically angular to subangular and commonly have polished and striated surfaces. Scaly fabric occurs in clay-rich rocks that are composed of phacoids whose surfaces make up an anastomosing network of curviplanar, striated

shear surfaces. The intensity of the fabric is a function of several parameters (strain, composition, etc.) but will be described as weak, moderate, or intense.

The recognition of natural breccia and gouges in cores is of primary importance because it constitutes a straightforward way to identify fault zones and, more precisely, principal slip zones that host the maximum displacement. This recognition, easily done in the field, appears to be less trivial in cores, mainly because of frequent drilling-induced or splitting-induced brecciation and/or drilling mud injection; both processes tend to produce structures that mimic those found in nature. During Expedition 343, the distinction between natural and drilling-induced breccia was based on the following set of observations:

- Fragments observed in natural breccia commonly show polished or striated surfaces, whereas the fragments in drilling-induced breccia commonly lack such features, except for "spiral" slickenlines resulting from the coring process.
- Natural breccia is commonly bounded by, and grades into, less fractured rock, and the fracture fabrics in the bounding rocks display preferred orientations.
- Natural breccia is marked by low contrast in CT images between clasts and matrix with high CT numbers, whereas CT images of drilling-induced breccia are marked by spherical voids and bright clasts in a much darker matrix with low CT numbers (Expedition 316 Scientists, 2009b).

The distinction between natural gouge and drilling-induced mud is delicate. Drilling mud commonly occurs along biscuiting boundaries, at the periphery of cores, or as veins injected across core pieces, perpendicular to the core axis. The transition between drilling mud and surrounding rock is typically sharp. Drilling mud commonly includes small (2 mm to 1 cm) fragments of nearby rock. Natural gouge might form a gradual transition zone with surrounding rock, which consists in most cases of fault breccia or microbreccia. Fragments are either nonexistent or are of very small size (<1 mm long).

Multichannel seismic reflection data and the geologic setting of the Tohoku-oki subduction zone suggest the structural complexity in the toe region of the frontal prism could result from slumping, sliding, and faulting. Sedimentary breccia may be present. Thus, especially for this expedition, it was essential to distinguish fault-related tectonic structures from gravitational deformation structures. Natural breccia of tectonic and sedimentary origin is commonly difficult to distinguish, particularly in core samples. During Expedition 343, the origin of a breccia layer was established by integrating the textural observations (documented independently) and the stratigraphic context as follows:

- Sedimentary breccia may display erosional bases and/or depositional tops (e.g., fining-upward sequences).
- Tectonic breccia may grade from protobreccia to breccia, whereas this feature is absent in sedimentary breccia.
- Sedimentary breccia typically contains a wider range of clast compositions.
- The fragments in sedimentary breccia tend to lack polished or striated faces that are common in tectonic breccia.

Minor faults

It may be difficult to distinguish natural faults from drilling-induced faults. Helicoidal striated surfaces or polished surfaces showing striations that diverge outward most likely indicate drilling-induced fracturing resulting from the torque exerted by the bit on sediment. In contrast, faults that display more planar geometries, parallel lineations, and orientations compatible with preferred orientations displayed by multiple faults nearby are likely natural features. Deformation bands are also considered natural deformation features, even though they rarely exhibit striated surfaces. Lastly, when the orientation data are corrected for drilling-related rotations using the paleomagnetic data, natural minor faults are expected to display preferred orientations, whereas drilling-induced faults are expected to yield randomly distributed orientations.

Structural sample protocols

Structural fabrics observed in soft or partially lithified sediment often need special handling to preserve them for observation, particularly in clay-rich lithologies. One of the major scientific objectives of Expedition 343 is to clarify the characteristics of fault zones active during large earthquakes. In particular, the identification of principal slip zones from recovered cores is crucial for understanding deformation mechanisms and the role of fluid during earthquake rupture. If thin (potentially on the order of millimeters in thickness) slip zones are bounded by fragile rocks (i.e., a fault damage zone), conventional core splitting using a water-cooled saw will result in destruction of the original structures. To protect possible important structures and preserve WRC sampling for other purposes (e.g., squeezing interstitial water for geochemical and microbiological analyses), we deployed the following protocol, which was based on special handling of "critical intervals" de-

veloped by Expedition 316 scientists for treatment of thin dark gouges in the megasplay fault zone and the frontal thrust zone.

First, we checked CT images of recovered cores to find noticeably brighter or darker bands, taking the spatial resolution of the CT image into consideration (the size of each pixel is 0.188 mm × 0.188 mm). From these, we chose critical intervals that should be preserved as WRCs. In particular, we carefully examined crosscutting relationships between lithologic surfaces and fractures to select possible recent slip zones. Thereafter, critical intervals to be preserved as whole-round samples were confirmed by the Co-Chief Scientists and Expedition Project Manager. Soon after such permission was granted, the shipboard scientists developed a research and sample-processing plan. Once all whole-round samples were taken, the cores were carefully split longitudinally into archive and working halves using an ethanol-cooled saw. Visual structural description and nondestructive measurements were performed on the split cores, and then samples for structural, chemical, physical properties, and mineralogical analyses were taken from the working half.

X-ray diffraction sampling

Bulk powder samples were acquired from core smoothing or trimming activities or were independently sampled to isolate individual horizons of interest. Samples were centrifuged for clay separation as required, dried, and ball-milled to <10 µm particle size according to standard shipboard protocols.

Maintenance of moisture content for essential samples

Certain requests for samples required particular treatment to maintain moisture content as close as possible to the recovered state because dessication may affect clay-rich samples (e.g., of fault gouge). This dessication may

- Affect delicate features of microstructural interest and introduce new structures (e.g., microcracks) that could be mistaken for primary features;
- Permanently affect permeability, and possibly cohesive strength, so that subsequent rock mechanics investigations yield misrepresentative results; and
- Result in changes in the structural arrangement of clay minerals (of interest for textural studies).

Three different protocols were adopted in these cases, depending on the intended end use of the sample:

1. For samples of microstructural interest, alcohol and LR White resin impregnation was used.
2. For whole-round samples of interest for physical properties measurements, whole rounds were packed into plastic liners, sponges dampened with distilled water or seawater were placed against the sample ends, and then the ends were capped and sealed with tape. These samples were stored in a moisture-controlled refrigerator as soon as possible.
3. For clay fabric studies, samples were extracted from the cut surface (in the case of split core) or a core surface carefully scraped clean of any drilling mud (for whole rounds) before visual core description was undertaken. These samples were ~1 cm^3 and were cut out with a spatula to have a V-shape with the apex pointing downhole (similar to the procedure followed by San Andreas Fault Observatory at Depth [SAFOD] and Deep Fault Drilling Project [DFDP-1]). These samples were placed in small plastic bags, which were then placed in plastic "bottles" to provide protection from crushing, and placed in a refrigerator. In an effort to preserve sample moisture, plastic wrap was used to cover and seal the split core except when temporarily removed as necessary for sample description.

Biostratigraphy

Identification of microfossils found in the core was used to help date the sediment. Radiolarian zones are given in the North Pacific zonation of Kamikuri et al. (2004, 2007) wherever possible. Absolute ages of bioevents are also provided by Kamikuri et al. (2004, 2007).

Biostratigraphy analyses were generally carried out on material from the core catcher for each core, although a few cores did not have a suitable amount or quality of sample to enable microfossil identification.

Sample preparation for microscopic examination followed the standard techniques described by Sanfilippo et al. (1985). Samples were treated with hydrogen peroxide (20% H_2O_2) and sodium pyrophosphate (5% $Na_4P_2O_7$) and heated to boiling. Hydrochloric acid (HCl) was added to dissolve calcareous components where necessary. Disaggregated particles were wet-sieved through a 63 µm mesh sieve. Remaining residues were removed and dried. Undisaggregated sediment was treated again. The clean particles were strewn on glass slides and mounted with Entellan-New. Slides were examined with a transmitted light microscope at a magnification of 100× to 400×. The first 100 specimens encountered on one slide were counted, after which

slides were scanned to determine whether other taxa were present.

Preservation of the radiolarian assemblage was based on the following categories:

G = good (radiolarians show no sign of dissolution with only minor fragmentation).
M = moderate (radiolarians show evidence of moderate dissolution with obvious fragmentation).
P = poor (radiolarians show signs of a high degree of dissolution with very few intact specimens).

Paleomagnetism

Paleomagnetic and rock magnetic investigations on board the *Chikyu* during Expedition 343 were primarily designed to determine the characteristic remanence directions for use in a tectonic study. Paleomagnetic measurements were performed only on discrete minicores and cube samples taken from the working halves. Routine measurements on archive halves collected during Expedition 343 were conducted with the superconducting rock magnetometer (SRM) during Expedition 343T.

Laboratory instruments

The paleomagnetism laboratory on board the *Chikyu* houses a large (7.3 m × 2.8 m × 1.9 m) magnetically shielded room, with its long axis transverse to the length of the ship. The total magnetic field inside the room is ~1% of Earth's magnetic field. The shielded room houses the magnetometers and other instruments described in this section and is large enough to comfortably handle standard IODP core sections (~150 cm in length).

Superconducting rock magnetometer

The long-core SRM (2G Enterprises, model 760) unit is ~6 m long with an 8.1 cm diameter access bore. A 1.5 m split core liner can pass through a magnetometer, an alternating field (AF) demagnetizer, and an anhysteretic remanent magnetizer. The system includes three sets of superconducting pickup coils, two for transverse moment measurement (*x*- and *y*-axes) and one for axial moment measurement (*z*-axis). The noise level of the magnetometer is $<10^{-7}$ A/m for a 10 cm^3 volume rock. The magnetometer includes an automated sample handling system (2G804) consisting of aluminum and fiberglass channels designated to support and guide long-core movement. The core itself is positioned in a nonmagnetic fiberglass carriage that is pulled through the channels by a rope attached to a geared high-torque stepper motor. A 2G600 sample degaussing system is coupled to the SRM to allow automatic demagnetization of samples up to 100 mT. The system is controlled by an external computer and enables programming of a complete sequence of measurements and degauss cycles without removing the long core from the holder.

Prior to Expedition 343, the SRM was upgraded to enable operation without liquid helium. Installation of the upgraded SRM onto the *Chikyu* was planned during the port call at Shimizu, Japan, before Expedition 343. However, because of the shortened port call, the installation was postponed until after the completion of Expedition 343. Thus, for paleomagnetism studies during Expedition 343, we could only measure remanent magnetization of discrete samples with the spinner magnetometer. Continuous paleomagnetic measurements using the archive halves of the core were performed during Expedition 343T in July.

Spinner magnetometer

A spinner magnetometer, model SMD-88 (Natsuhara Giken Co. Ltd.), was utilized during Expedition 343 for remanent magnetization measurement. The noise level was ~5×10^{-7} mAm^2, and the measurable range was from 5×10^{-6} to 3×10^{-1} mAm^2. Two holders were prepared for the measurements, one (small or short) for weak samples and the other (large or tall) for strong samples. Five standard samples with different intensities were prepared to calibrate the magnetometer. Standard cylindrical samples (2.5 cm diameter × 2.2 cm long) taken with a minicore or 7 cm^3 Natsuhara cubes were measured in three or six positions with a typical stacking of 64–256 spins. The measurement sequence took ~1 min for three positions.

Alternating field demagnetizer

The DEM-95 AF demagnetizer (Natsuhara Giken Co. Ltd.) is set for demagnetization of standard discrete samples of rock or sediment. The unit is equipped with a sample tumbling system to uniformly demagnetize up to a peak AF of 180 mT.

Thermal demagnetizer

The TDS-1 thermal demagnetizer (Natsuhara Giken Co. Ltd.) has a single chamber for thermal demagnetization of dry samples over a temperature range of room temperature to 800°C. The chamber holds up to 8 or 10 cubic or cylindrical samples, depending on the exact size. The oven requires a closed system of cooling water, which is conveniently placed next to the shielded room. A fan next to the µ-metal cylin-

der that houses the heating system was used to cool samples to room temperature. The measured magnetic field inside the chamber was <20 nT.

Pulse magnetizer

The MMPM10 pulse magnetizer (Magnetic Measurement Ltd., United Kingdom; **www.magnetic-measurements.com/**) can produce a high magnetic field pulse in a sample. The magnetic field pulse is generated by discharging a bank of capacitors through a coil. A maximum field of 9 T with a 7 ms pulse duration can be produced by the 1.25 cm diameter coil. The other coil (3.8 cm diameter) generates a maximum field of 2.9 T.

Anisotropy of magnetic susceptibility

The Kappabridge KLY 3S (AGICO Inc.) magnetic susceptibility meter is designed for anisotropy of magnetic susceptibility (AMS) measurements. Data are acquired from spinning measurements around three mutually perpendicular axes. The deviatoric susceptibility tensor can then be computed. An additional measurement for bulk susceptibility completes the sequence. The sensitivity for AMS measurements is 2 × 10^{-8} SI. Intensity and frequency of the applied field are 300 mA/m and 875 Hz, respectively. This system also includes a temperature control unit (CS-3/CS-L) for temperature variation of low-field magnetic susceptibility of samples.

Discrete samples and sampling coordinates

A total of 56 discrete cubic samples (~7–8 cm^3) or minicores (~11 cm^3) were taken from the working halves in order to determine paleomagnetic direction, primarily for tectonic studies. Sampling frequency depended on the properties of the core material (e.g., to avoid flow-in, coring disturbances, etc.) and the distribution of interbedded lithologies. For the most part, paleomagnetic sampling concentrated on hemipelagic mudstones as the dominant lithology. The standard IODP core coordinate system was used, in which the +*x*-axis is the vertical upward direction when the core (archive half) is on its curved side, the +*y*-axis is the direction to the left along the surface of the archive halves when looking upcore, and the +*z*-axis is the downcore direction (Fig. **F19**).

Measurements

Stepwise demagnetization experiments on discrete paleomagnetic samples were conducted using the AF demagnetizer to isolate various magnetic components of the samples. Whenever possible, demagnetization was continued up to 120 mT until an unambiguous and reliable determination of direction of the stable component of magnetization was achieved.

Remanent magnetization of archive halves was measured at 2 cm intervals using the 2G long-core SRM during Expedition 343T. We adopted AF demagnetization levels of 15 and 20 mT because AF demagnetization results of discrete samples showed that AF demagnetization below 15 mT was insufficient for removing drilling-induced magnetization of the cores drilled during this expedition. However, we adopted AF demagnetization at 5, 10, 15, and 20 mT for Core 343-C0019E-17R, from which no discrete paleomagnetic samples were measured.

In addition to standard paleomagnetic measurements, bulk magnetic susceptibility and AMS of the discrete paleomagnetic samples were measured using the Kappabridge KLY 3S magnetic susceptibility meter.

Paleomagnetic reorientation of cores

Azimuthal orientation of drilled core material is of prime importance when modeling directional properties of rock formations. Paleomagnetic core reorientation has been successfully used for a number of years (e.g., Fuller, 1969; Kodama, 1984; Shibuya et al., 1991; Parés et al., 2007). The procedure is based on determining the direction of stable remanent magnetization (either viscous remanent magnetization or primary magnetization) with respect to a common reference line that is marked lengthwise along the core. Assuming a moderate sedimentation rate of ~5 cm/k.y. and a magnetization lock-in depth of ~10 cm, a typical sample depth interval of 2.5 cm might be enough to average the secular variation of the geomagnetic field, and the paleomagnetic direction roughly points in the direction of geographic north. During Expedition 343, the characteristic remanent magnetization (ChRM) direction, calculated using principal component analysis (Kirschvink, 1980), was used to reorient the blocks with important deformation structures (see **"Structural geology"**).

Data reduction and software

Data reduction (Zijderveld demagnetization plots and equal area projections) was conducted using visualization software called "Progress" for Mac OSX programmed by H. Shibuya (Kumamoto University, Japan). Principal component analysis (Kirschvink, 1980) was also performed by using Progress software to determine ChRM directions.

Physical properties

Physical properties measurements provide fundamental information required to characterize lithologic units and allow for the correlation of coring results with downhole logging data. A variety of techniques and methods were used to characterize Expedition 343 core samples. Prior to sampling and interpretation, X-ray CT images were captured for all cores. After the CT scans were completed, GRA density, magnetic susceptibility, NGR, PWV, and electrical resistivity were measured using the MSCL-W after thermal equilibration with room temperature (~20°C). After that, cores were split in two longitudinally: one archive half and one working half for sampling and analysis. Thermal conductivity measurements were made on working halves using the TeKa thermal conductivity meter in half-space mode. For unconsolidated sediment, electrical resistivity was measured by inserting a four-pin electrode into the surface of working halves. For consolidated sediment, PWV and electrical resistivity were made on discrete cube samples in the *x*-, *y*-, and *z*-directions to evaluate anisotropy of velocity and resistivity. In addition, unconfined compressive strength (UCS) tests were performed on 1.98 cm diameter minicores using a manual hydraulic press (Carver Inc., model 30-12). MAD properties were determined for discrete samples collected from working halves, using a custom-built motion-compensated shipboard balance system and a Quantachrome penta-pycnometer. Particle size distribution on unconsolidated sediment was analyzed by a multiwavelength laser particle analyzer (Beckman Coulter, model LS13320). Details and procedures for each physical properties measurement are described below.

MSCL-W

GRA density

Bulk density can be used to estimate the pore volume in sediment and evaluate the consolidation state of sediment. GRA density is an estimate of bulk density based on the attenuation of a gamma ray beam. The beam is produced by a ^{137}Cs gamma ray source at a radiation level of 370 MBq within a lead shield with a 5 mm collimator, which is directed through the WRC. The gamma ray detector on the opposite side of the core from the source includes a scintillator and an integral photomultiplier tube to record the gamma radiation that passes through the core. Bulk density (ρ_b) is determined from GRA by

$$\rho_b = [\ln(I_o/I)]/\mu d, \quad (26)$$

where

I_o = gamma ray source intensity,
I = measured intensity of gamma rays passing through the sample,
μ = Compton attenuation coefficient, and
d = sample diameter.

The Compton attenuation coefficient (μ) and I_o are provided by the MSCL-W and are treated as constants, so ρ_b can be calculated from I.

The gamma ray detector is calibrated with sealed calibration cores (one standard core liner filled with distilled water and aluminum cylinders of various diameters). To establish the calibration curves, gamma ray counts were taken through each aluminum cylinder for 60 s. Each aluminum cylinder has a density of 2.7 g/cm^3, and d is 1, 2, 3, 4, 5, or 6 cm. The relationship between I and μd is

$$\ln(I) = A(\mu d) + B + C, \quad (27)$$

where A, B, and C are coefficients determined from the calibration. GRA density measurements on the core samples were conducted every 4 cm for 4 s. The spatial resolution of each measurement is 5 mm.

Magnetic susceptibility

Magnetic susceptibility is the degree to which a material can be magnetized by an external magnetic field and therefore provides information about sediment composition. The measurements were made using a Bartington MS2C loop sensor with an 8 cm diameter. An oscillator circuit in the sensor produces a low-intensity (~140 A/m RMS), nonsaturating, alternating magnetic field (0.565 kHz). Bringing any material within the influence of this field will cause a change in oscillator frequency. The frequency information returned in pulse form to the susceptometer is converted into magnetic susceptibility. The spatial resolution of the loop sensor is 23–27 mm and is accurate to within 2%. Magnetic susceptibility data were collected every 4 cm along the core.

P-wave velocity

PWV data can be used to evaluate small-strain moduli, correlate between downhole logging and core data, and evaluate porosity and cementation. *P*-wave (compressional) velocity (V_P) is defined by the time required for a compressional wave to travel a specific distance:

$$V_P = d/t_{core}, \quad (28)$$

where d is the path length of the wave across the core and t_{core} is the traveltime through the core.

PWV transducers on the MSCL-W system measure total traveltime of the compressional wave between transducers. The wave travels horizontally across the whole core and core liner. The total traveltime observed is composed of

t_{delay} = time delay related to transducer faces and electronic circuitry,
t_{pulse} = delay related to the peak detection procedure,
t_{liner} = transit time through the core liner, and
t_{core} = traveltime through the sediment or rock.

The system is calibrated using a core liner filled with distilled water, which provides control for t_{delay}, t_{pulse}, and t_{liner}. From these calibrations, V_P can be calculated for the whole-round specimens in core liners as follows:

$$V_P = (d_{cl} - 2d_{liner})/(t_o - t_{pulse} - t_{delay} - 2t_{liner}), \quad (29)$$

where

d_{cl} = measured diameter of core and liner,
d_{liner} = liner wall thickness, and
t_o = measured total traveltime.

Equation 29 assumes that the core completely fills the core liner.

Electrical resistivity

Within limits, electrical resistivity measurements may be useful for estimating other sediment physical properties, such as porosity, tortuosity, permeability, and thermal conductivity. Bulk electrical resistivity is controlled by solid grain resistivity, pore fluid resistivity, and pore space distribution and connectivity. Electrical resistivity (R) is defined by the electrical resistance and geometry of the core measured:

$$R = \Gamma(A/L), \quad (30)$$

where

Γ = electrical resistance,
L = length of measurement, and
A = cross-sectional area of the core.

The NCR sensor on the MSCL-W system induces a high-frequency magnetic field in the core with a transmitter coil. This induces an electrical current in the bulk sediment that is inversely proportional to its resistivity. A receiver coil measures the secondary magnetic field generated by this induced electrical current. To measure this smaller magnetic field accurately, a differencing technique has been developed that compares readings from the sample core to readings from an identical set of coils operating in air. Electrical resistivity data were obtained at 4 cm intervals on the MSCL-W.

Natural gamma radiation

NGR measurements provide insight into sediment composition and thus can be used to describe lithology. WRCs were monitored for NGR emissions to obtain spatial variability in radioactivity and establish profiles that can be correlated with downhole gamma ray logs. The measurement device utilizes a lead-shielded detector counter optically coupled to a photomultiplier tube and connected to a bias base with a high-voltage power supply and signal preamplifier. Two horizontal and two vertical sensors are mounted in a lead, cube-shaped housing. The NGR system records radioactive decay of long-period isotopes ^{40}K, ^{232}Th, and ^{238}U. NGR has a resolution of 120–170 mm and was measured every 16 cm with a count time of 30 s. Background radiation noise was determined by making measurements on a water-filled calibration core.

Thermal conductivity

Thermal conductivity was measured on the surface of working halves using the half-space line source (Vacquier, 1985), which approximates an infinite line source. The half-space probe was placed directly on the split core and saturated with seawater to provide good contact. The measurements produce a scalar thermal conductivity value in the plane perpendicular to the orientation of the probe. All measurements were made after the cores had equilibrated with room temperature. At the beginning of each measurement, temperature in the sediment was monitored to ensure that thermal drift was <0.4 mK/min (typically within 1–2 min). After it was established that the temperature was near equilibrium, a calibrated heat source was applied and the rise in temperature was recorded for ~80 s. Values of thermal conductivity were based on the observed rise in temperature for a given quantity of heat. The half-space line source probe was calibrated at least once every 24 h. The calibration was performed on one of two Macor samples of known thermal conductivity (1.652 ± 2% W/[m·K]).

Unconfined compressive strength measurements

For stiff indurated sediment, UCS tests were performed on minicores 1.4–2.3 cm in length and 1.98 cm in diameter. These tests provide valuable strength data for sediment when vane shear or penetrometer devices are unsuitable. Samples were drilled from the working half perpendicular to the core axis (in the x-direction with respect to the core reference model; Fig. F20). Care was taken to ensure that the cores were free of defects and the core end surfaces were parallel and planar. Samples were then placed in a

manual hydraulic press (Carver, Inc., model 30-12) with a load capacity of 30 tons and aligned so that the load from the press was applied vertically along the minicore axis. In order to measure force (F), a load cell with a capacity of 300 kN (TEAC Corp., model KR300KN) was placed directly beneath the sample. The sample was loaded to failure manually at a slow rate, and the maximum value registered by the load cell (F_{max}) was recorded. The UCS of the sample is calculated as

$$UCS = F_{max}/A, \quad (31)$$

where A is the cross-sectional area of the sample. The reading resolution of the load cell is 10 N. For a sample 2.0 cm in diameter, this corresponds to a resolution of 0.3 MPa.

Because of the size limitations imposed by the geometry of the working half of the core, our samples have a length/diameter ratio (l/d) close to 1. The uniaxial strength of geologic materials is known to depend inversely on this ratio and asymptotically approaches a steady value at l/d = ~3 (Paterson and Wong, 2005). Based on these data, we use a quadratic function to calculate a correction factor (C_f) from the aspect ratio of the sample (l/d):

$$C_f = -0.04(l/d)^2 + 0.21(l/d) + 0.7. \quad (32)$$

We consider this correction to be valid for $l/d \leq 2.5$.

P-wave velocity and electrical resistivity measurements

Cubic samples (~2 cm × 2 cm × 2 cm) were cut from working halves with a diamond blade saw in order to measure electrical resistivity and *P*-wave velocity for discrete samples (PWVD). For soft sediment, where cubic samples could not be made, only electrical resistivity was measured using the bridge method with a four-pin electrode. All cubes were cut to be consistently oriented with respect to the core reference model (Fig. F20). All samples were immersed in a 3.5% NaCl solution for a few seconds prior to measurement. Carefully controlling the sample orientation during preparation allowed first-order measurements of both PWVD and electrical resistivity, as well as anisotropy of PWVD and electrical resistivity.

PWVD along a given direction was measured using a *P*-wave logger for discrete samples (PWL-D). The PWL-D is equipped with two 230 kHz transducers, one used as a transmitter and one as a receiver. Sample length (L) was measured with a laser distance sensor. During measurement, the sample was placed between the transducers and held in place with a weight of 2.5 kg. The transmitter was connected to a pulse generator, and the receiver was connected to an oscilloscope synchronized with the pulse generator. *P*-wave total traveltime (t) for the first arrival was picked and logged from the digitally displayed oscilloscope signal. The velocity in any direction (e.g., V_{Px}) is calculated from the sample length (e.g., L_x), total traveltime (t_x), and system-calibrated delay time (t_{delay}):

$$V_{Px} = L_x/(t_x - t_{delay}). \quad (33)$$

The traveltime delay and laser distance sensor were calibrated daily. Calibration of traveltime delay was determined by placing the transmitter and receiver in direct contact and measuring traveltime. Similarly, the laser distance was calibrated by placing the transmitter and the receiver in direct contact and also by spacing them using a 2.5 cm long reference specimen. Routine QC measurements were made by measuring velocity on glass and acrylic standards with known lengths and velocities.

Measurements of *P*-wave and *S*-wave velocity were also performed at elevated pressure. Sample size was the same as the PWVD measurements under atmospheric conditions (~2 cm × 2 cm × 2 cm); however, these samples were vacuum-dried at room temperature for ~24 h prior to testing. Piezoelectric transducers (2 MHz) are attached with an adhesive gel cement to opposing faces of the sample, and the remaining sample surfaces are coated in silicone grease to isolate it from the confining medium. The sample is then set inside a pressure vessel, where *P*-wave and *S*-wave velocities are initially calculated according to Equation 33 under atmospheric conditions. Updated velocities are automatically calculated as isotropic confining pressure is applied. The sample length (L) of the dried sample is measured prior to being encased in silicone and loaded in the pressure vessel. Because decreases in sample length caused by increasing pressure during measurement are not recorded, these measurements should be considered the upper bounds on wave velocity.

Electrical resistivity was measured with an Agilent 4294A component analyzer using the bridge method with a two-terminal circuit for cubic samples. The oriented specimen cube was placed between two stainless steel electrodes covered with seawater-saturated filter paper. The magnitude ($|Z|$) and phase (θ) of the complex impedance were measured at 25 kHz between opposite cube faces. The cube was rotated to measure impedance in the x-, y-, and z-directions (Fig. F20). Electrical resistivity for each direction (e.g., R_x) was computed from the complex imped-

ance measured along each direction (e.g., x) and sample dimensions defined by face lengths (L):

$$R_x = |Z_x|\cos\theta_x(L_yL_z/L_x). \quad (34)$$

With P-wave velocity (V_{Px}, V_{Py}, and V_{Pz}) and electrical resistivity measured in the x-, y-, and z-directions, anisotropy is calculated following the approach of Carlson and Christensen (1977). Potential causes of anisotropy include (1) alignment of pores during compaction, (2) fabric development, and (3) microstructures such as microfractures and microcracks. Horizontal and vertical P-wave velocity anisotropy (α_{VPhor}, α_{VPvert}) and electrical resistivity anisotropy (α_{Rhor}, α_{Rvert}) are calculated by comparing the horizontal (x and y) and vertical (z) components of the measurement expressed as a percentage of the mean (e.g., Shipboard Scientific Party, 2001):

$$\alpha_{VPhor}\,(\%) = 200[(V_{Px} - V_{Py})/(V_{Px} + V_{Py})], \quad (35)$$

$$\alpha_{VPvert}\,(\%) = 200[(V_{Px} + V_{Py})/2 - V_{Pz}]/[(V_{Px} + V_{Py})/2 + V_{Pz}], \quad (36)$$

$$\alpha_{Rhor}\,(\%) = 200[(R_x - R_y)/(R_x + R_y)], \quad (37)$$

and

$$\alpha_{Rvert}\,(\%) = 200[(R_x + R_y)/2 - R_z]/[(R_x + R_y)/2 + R_z]. \quad (38)$$

Moisture and density measurements

Discrete samples from the working-half cores were used for determination of index properties (e.g., bulk density, grain density, dry density, water content, porosity, and void ratio). Index properties are determined from phase relations, mass measurements on wet and dry specimens, volume measurements on dry specimens, and corrections for salinity. In general, one discrete sample for index properties was collected from each core section. Sample intervals were occasionally shifted to select minimally disturbed, homogeneous samples. Each discrete index property sample was ~5 cm^3.

Wet and dry masses were measured using a paired electronic balance system, which is designed to compensate for the ship's heave. The sample mass was counterbalanced with a precisely known mass (10 or 40 g) that was within 3–20 g or 20–60 g of the sample mass, respectively. The sample mass was determined to a precision of ±0.005 g. The balance system was calibrated at least once per 24 h.

To minimize desiccation, MAD sample collection was immediately followed by measurement of wet sediment mass (M_{wet}). After M_{wet} measurements, samples were dried in a convection oven at 105° ± 5°C for 24 h. Dry samples were placed in a desiccator for at least 1 h to equilibrate to room temperature (~20°C), and then dry sediment mass (M_{dry}) and dry sediment volume (V_{dry}) were measured. A five-chamber Quantachrome pentapycnometer was used to measure V_{dry} by helium-displacement technique with a precision of ±0.04 cm^3. The five-chamber system allowed the measurement of four sample volumes and one calibration sphere. Each measured volume is the average of five volume measurements. The calibration sphere was rotated between all measurement chambers to monitor for errors in each chamber. The pycnometer was calibrated at least once per 24 h.

Standard ODP/IODP practices were used to determine pore water mass and volume, salt mass and volume, and solid grain mass and volume (Blum, 1997). From these data, bulk density, dry density, grain density, porosity, and void ratio were calculated (Blum, 1997). Standard seawater density (1.024 g/cm^3) and salinity (35 parts per thousand [ppt]) and a constant salt density (2.22 g/cm^3) were assumed for all calculations.

Water content

Water content (W_c) was determined following the American Society for Testing and Materials (ASTM) standard D2216 (ASTM International, 1990). Corrections are required for salt when measuring the water content of marine samples. In addition to the water content calculation in ASTM D2216 (i.e., the ratio of pore fluid mass to dry sediment mass; W_c[dry]), we also calculated the ratio of pore fluid mass to total sample mass (W_c[wet]). The equations for water content are

$$W_c(\text{dry}) = (M_{wet} - M_d)/(M_d - sM_{wet}) \quad (39)$$

and

$$W_c(\text{wet}) = (M_{wet} - M_d)/M_{wet}(1 - s), \quad (40)$$

where

M_{wet} = total mass of the discrete sample,
M_d = mass of the dry sample, and
s = salinity (assumed constant at 0.035).

Bulk density

Bulk density is the density of the discrete core sample ($\rho_b = M_{wet}/V_t$). Total wet sample mass (M_{wet}) was measured immediately after collecting each discrete sample using the dual-balance system. Total sample volume assuming 100% saturation ($V_t = V_g + V_{pw}$) was determined from the pycnometer measurement

of grain volume (V_g) and calculated volume of pore water (V_{pw}). Solid grain and pore water volume are determined as

$$V_g = V_d - (M_{wet} - M_d)s/\rho_{salt}(1 - s) \quad (41)$$

and

$$V_{pw} = (M_{wet} - M_d)/\rho_{sw}(1 - s), \quad (42)$$

where

V_d = dry volume,
ρ_{salt} = salt density, and
ρ_{sw} = standard seawater density.

Porosity and void ratio

Porosity (ϕ) relates the volume of pores to total sample volume; void ratio (e) relates the pore volume to solid grain volume. They are calculated as

$$\phi = \rho_b V_{pw}/M_{wet} \quad (43)$$

and

$$e = V_{pw}/V_g. \quad (44)$$

Grain density

Grain density (ρ_g) was determined from measurements of dry mass and dry volume made with the dual-balance system and the pycnometer, respectively. Mass and volume were corrected for salt, yielding

$$\rho_g = (M_d - M_{salt})/\{V_d - (M_{wet} - M_d)s/[\rho_{salt}(1 - s)]\}, \quad (45)$$

where M_{salt} is the mass of salt and ρ_{salt} is the density of salt (assumed to be constant at 2.22 g/cm^3).

Particle size analysis

Particle size analysis is a tool used to characterize fine-grained sediment by grain size. It can be used to identify different lithologies and locate repeating sections of sediment by comparison of grain size spectra on series of samples. We used the multiwavelength laser particle analyzer (LS; Beckman Coulter, model LS13320) to measure grain size spectra of sediment samples taken from working halves. Laser particle analysis is based on the principle that particles of a given size diffract light at a given angle, which increases with decreasing particle size. A parallel beam of monochromatic light with a 750 nm wavelength is passed through a suspension of sample material, and the diffracted light is focused onto a multielement ring detector. The detector senses the angular distribution of scattered light intensity (Syvitski, 1991; McCave et al., 1995). In addition to this beam, a polarization intensity differential scattering (PIDS) assembly is used to characterize smaller scale particles (<0.4 µm). This assembly illuminates the particles with vertically and horizontally polarized lights of three different wavelengths (450, 600, and 900 nm), and the differential scattering patterns of each wavelength is used to determine the particle size. The laser particle analyzer can provide a rapid, automated, and precise measurement of sediment grain size ranging from 0.375 µm to 2 mm in ~10 min, including a rinse stage. The LS used is equipped with a microvolume module (MVM) system, and the autosampler allows the user to load a run of 30 samples, including two control samples, to be analyzed automatically. The accompanying software calculates the grain size distribution of the sample and appropriate statistics. Data may be exported to external programs.

During this expedition, an aliquot of a 0.5 g sample was used for grain size analysis. One sample per section was taken from the remainder of cube samples used for PWVD and resistivity measurements. Because organic particles may have shapes, geometries, and other surface properties that differ from routine laser particle size analysis of siliciclastic sediment, organic-rich samples were soaked in a 10% v/v H_2O_2 solution for 12 h to oxidize and remove organic matter. Sediment was then dispersed in an aqueous solution using both chemical and mechanical means. Chemical dispersion was performed using a dilute alkaline solution of sodium polyphosphates $(NaPO_3)_6$. Samples were then mechanically dispersed by turbulent mixing using a shaker.

Color spectrometry

Color spectrometry is an IODP standard measurement that is used to quantify visually observed changes in the split core using the MSCL-C. This system is equipped with a color spectrophotometer (Konica-Minolta, CM-2600d) and an aluminum frame that allows operators to load up to seven core sections. The sensor unit, which includes the spectrophotometer and distance laser measuring system, traverses each section and settles at each measurement point on the archive core surface.

Reflected light from the sample surface is collected by the color spectrophotometer's integration sphere. In this case, specular component was excluded (SCE setting) in order to exclude glare; this setting is considered suitable for sediment. The light is divided into wavelengths at a 10 nm pitch (400–700 nm), and the spectral sensors in the sphere convert the light to electrical currents proportional to the light

intensity. The color spectrum of the sample is then normalized by the source light of the reflectance. The obtained spectrum is calibrated with the measurement of a pure white standard and with a black box (zero calibration). Measurements can be calculated based on the 2° or 10° standard observer and any of 11 illuminants. The measured color spectrum is described by the parameters L*, a*, and b*. The parameter L* describes lightness on a white-to-black scale, a* quantifies color on a green-to-red scale, and b* quantifies color on a yellow-to-blue scale. These measurements may be used to recognize relative changes in bulk composition and are therefore useful for correlation between different recovered core sections and to analyze lithologic changes.

Geochemistry

Pore water chemistry

Interstitial water collection

The following description of geochemical methods is based largely on the same methods reported for Expedition 322 (Expedition 322 Scientists, 2010). The sampling locations and frequency were modified in accordance with the core handling plan described in **"Core handling."**

Interstitial water samples were obtained from 15.5 to 31 cm long whole-round sections from cores with >1.4 m of recovery (i.e., more than one section recovered). Samples were collected at a frequency of one per core if recovery was sufficient and interstitial water samples did not conflict with samples needed for visual core description. Sample volume was selected in an attempt to recover the necessary 25 mL of interstitial water to achieve the goals of chemical analyses while minimizing the volume of sample removed from the core.

Whole-round samples were cut and capped as quickly as possible after the core arrived on deck and immediately taken from the core cutting area to be scanned by X-ray CT. A watchdog (shipboard structural geologist) and geochemist viewed the composite X-ray CT scan to select a sample that did not contain potentially important structural features and was suitably free from fracturing and other defects to minimize contamination from drilling fluid. Once approved by the watchdog, the sample was taken to the quality assurance/quality control (QA/QC) laboratory and immediately extruded from the core liner into a nitrogen-flushed glove bag. The exterior of the whole-round sample was thoroughly cleaned with a spatula to remove drilling contamination. The cleaned sediment was placed into a 9 cm diameter Manheim-type titanium squeezer (Manheim and Sayles, 1974) on top of filter paper rinsed with reagent-grade water (18.2 MΩ Millipore water, or "Milli-Q") placed on two 40 mesh titanium screens. Sediment was squeezed at ambient temperatures and pressures no higher than 25,000 psi to prevent the release of interlayer water from within clay minerals during the squeezing process. The interstitial water (4.1–63 mL) was collected through a 0.2 µm disposable polytetrafluoroethylene (PTFE) filter into a 24 or 60 mL acid-washed plastic syringe attached to the bottom of the squeezer assembly.

Interstitial water aliquots were collected for both shipboard and shore-based analyses (Table **T8**). High-density polyethylene (HDPE) sample vials for minor and trace element analysis were cleaned by immersion in 55°C 10% trace metal–grade 12M HCl for a minimum of 24 h and were subsequently rinsed in Milli-Q water and dried in a class 100 laminar flow clean hood. Samples for minor and trace element shipboard analyses were acidified with optima-grade 6M HCl before analysis by inductively coupled plasma–atomic emission spectroscopy (ICP-AES) or inductively coupled plasma–mass spectrometry (ICP-MS). Unless otherwise noted, the samples were stored at 4°C after collection. Aliquots for shore-based Li-B-Sr-Pb isotopic and trace element analyses were acidified with 6M HCl and stored in acid-washed 4 mL HDPE bottles. Aliquots for isotopic analyses of oxygen, hydrogen, and dissolved inorganic carbon (DIC) were placed in 2 mL septum screw-lid glass vials; samples for DIC were treated with 10 µL of a saturated $HgCl_2$ solution at room temperature. Aliquots for nitrogen isotopic analysis were stored in acid-washed 4 mL HDPE bottles with HCl and $HgCl_2$. Aliquots for sulfur isotopic analysis were placed in septum screw-lid glass vials with $ZnCl_2$ and frozen at –20°C. Aliquots for carbon isotopic analysis of dissolved organic carbon and acetate were placed in septum screw-lid glass vials with $HgCl_2$ and sulfamic acid. Aliquots for rare earth element analysis were acidified with optima-grade 6M HCl and stored in acid-washed 8 mL HDPE bottles. After interstitial water extraction was complete, sediment squeeze cakes (24–456 cm^3) were divided and sealed in plastic bags for archive material and shore-based analyses. Squeeze cake samples for shore-based microbiological analysis were stored at –80°C. All other squeeze cake samples were chilled at 4°C.

Correction for drilling contamination

In many intervals, the sedimentary material was extensively fractured by drilling disturbance, making some interstitial water whole rounds extremely difficult to clean prior to processing. In these cases, even after thorough cleaning, the interstitial water sam-

ples may possibly be contaminated with fluid that circulated in the borehole during drilling operations. In continental margin sediment, the sulfate–methane transition (SMT) zone is generally reached at shallow depths in the sediment section, typically shallower than ~40 mbsf. Below this depth, sulfate generally remains depleted. Thus, the presence of sulfate and methane in a sample collected below the SMT zone may be used as an indication of drilling-induced contamination by comparing the ratio of the sulfate measured in the sample to the sulfate concentration of seawater (28.9 mM). Likewise, concentration of the other ionic species can be corrected based on their concentration in surface seawater using the following equation:

$$X_{corrected} = [X_{measured} - (f_{sw} \times X_{sw})]/f_{iw}, \quad (46)$$

where

$X_{corrected}$ = corrected or in situ concentration of the analyte,
$X_{measured}$ = measured concentration of the analyte,
X_{sw} = analyte concentration in surface seawater (used in drilling),
f_{sw} = fraction of seawater introduced into the sample during drilling, and
f_{iw} = fraction of in situ interstitial water in the sample.

The fraction of seawater introduced by drilling disturbance and the fraction of in situ interstitial water are computed using Equations **47** and **48:**

$$f_{sw} = SO_{4\ measured}/SO_{4\ sw} \quad (47)$$

and

$$f_{iw} = 1 - f_{sw}, \quad (48)$$

where $SO_{4\ measured}$ is the measured sulfate concentration and $SO_{4\ sw}$ is the sulfate concentration in surface seawater.

Shipboard analytical results indicate that rather than seawater or drilling-fluid contamination, the presence of sulfate in pore water is derived from mixing with a remote sulfate-rich fluid source (see **"Geochemistry"** in the "Site C0019" chapter [Expedition 343/343T Scientists, 2013]). When corrections were applied to interstitial waters using sulfate concentrations, in some cases the correction resulted in negative values for magnesium and potassium. Potential contamination by seawater or drilling mud was checked using the perfluorocarbon (PFC) contamination tracer method described in **"Microbiology."** Those results indicate that contamination was generally low. Cores 343-C0019E-1R, 4R, 12R, 13R, 14R, 15R, and 19R were not contaminated (Table **T14** in the "Site C0019" chapter [Expedition 343/343T Scientists, 2013]). Cores 5R, 6R, 7R, 8R, and 20R showed minor contamination. Core 6R showed the greatest contamination, and caution should be exercised in interpreting interstitial water data from this sample. Given the entirety of the interstitial water data and the results from the PFC contamination tracer method, no contamination corrections were applied to these samples.

Interstitial water analysis

Interstitial water samples were routinely analyzed for refractive index with a RX-5000α refractometer (Atago) immediately after interstitial water extraction. The refractive index was converted to salinity based on repeated analyses of International Association of Physical Sciences of the Oceans (IAPSO) standard seawater. Precision for salinity was <0.1‰. Also, immediately after interstitial water extraction, samples were analyzed for pH and alkalinity by Gran titration with a pH electrode and a Metrohm autotitrator for the two samples where sufficient fluid was available. Alkalinity titrations had a precision of <2%, based on repeated analysis of IAPSO standard seawater. For sample volumes of ≤14 mL, alkalinity and pH were not measured (Table **T8**).

Sulfate and bromide concentrations were analyzed by ion chromatography (IC) (Dionex ICS-1500) using subsamples that were diluted 1:100 with Milli-Q water. At the beginning and end of each run, several different dilutions of IAPSO standard seawater were analyzed for QC and to determine accuracy. IAPSO standard seawater was analyzed after every seventh sample as a check for instrumental drift and to calculate analytical precision. Precision for the bromide and sulfate analyses was <3% and <0.8%, respectively. Average accuracy of bromide and sulfate analyses was <2% and 1.5%, respectively.

Chlorinity was determined by titration with silver nitrate ($AgNO_3$). We use the convention "chlorinity" for the titration data because it yields not only dissolved chloride but also all of the other halide elements and bisulfide. The average precision of the chlorinity titrations, expressed as 1σ standard deviation of means of multiple determinations of IAPSO standard seawater, is ≤0.5%.

Dissolved ammonium concentration was measured within 24 h of collecting the interstitial water sample by colorimetry, using an ultraviolet-visible (UV-vis) spectrophotometer (Shimadzu UV-2550) at an absorbance of 640 nm. A 0.1 mL sample aliquot was diluted with 1 mL of Milli-Q water, to which 0.5 mL phenol ethanol, 0.5 mL sodium nitroprusside, and 1 mL oxidizing solution (trisodium citrate and so-

dium hydroxide) were added in a capped plastic tube (Gieskes et al., 1991). The solution was kept in the dark at room temperature for >3 h to develop color. Precision and accuracy of the ammonium analyses were <2.5% and 3%, respectively.

Dissolved phosphate concentration was also measured by a colorimetric method using the UV-vis spectrophotometer at an absorbance of 885 nm. Because the phosphate concentration in the analysis solution must be <10 µM, appropriate aliquots of sample or standard solution (100 or 600 µL) were diluted to 1.1 mL with Milli-Q water (1000 or 500 µL) in a plastic tube. The mixed solution (ammonium molybdate, sulfuric acid, ascorbic acid, and potassium antimonyl tartrate) was added to the tube (Gieskes et al., 1991), which was capped and kept at room temperature to develop color. Precision and accuracy of the phosphate analyses were <2% and 2%, respectively.

Concentrations of major cations (sodium, potassium, magnesium, and calcium) were analyzed by IC on samples acidified with 0.4% 6M HCl. Samples were diluted by a factor of 200 with Milli-Q water. Each measurement batch included a Milli-Q water blank, seven standards for calibration prepared from a commercially available cation mixed standard (Kanto Chemical Co. Inc., P/N 07197-96), and IAPSO standard seawater (P-series) as a reference material, in addition to the interstitial water samples. The average precision estimated by repeated measurements of ½₀₀ IAPSO standard seawater were Na^+ < 1.1%, K^+ < 1.2%, Mg^{2+} < 1%, and Ca^{2+} < 1.1%, and the average accuracy of the analyses was Na^+ < 2.4%, K^+ < 0.5%, Mg^{2+} < 0.8%, and Ca^{2+} < 0.4%.

The minor elements (boron, barium, iron, lithium, manganese, silica, and strontium) were analyzed by ICP-AES (Horiba Jobin Yvon Ultima2). The interstitial water sample aliquot was diluted by a factor of 20 (0.5 mL sample added to 9.5 mL of 1% ultrapure double-distilled nitric acid solution spiked with 10 ppm yttrium). Because of the high concentration of matrix salts in interstitial water samples at a 1:20 dilution, matrix matching of the calibration standards is necessary to achieve accurate results by ICP-AES. A matrix solution that approximated seawater major ion concentrations was prepared by dissolving the following salts in 1 L of Milli-Q water acidified with 4 mL of optima-grade 6M HCl: 27 g NaCl, 3.8 g $MgCl_2$, 1.0 g $CaCO_3$, and 0.75 g KCl. Sulfate was not added to the matrix-matching solution because we expected the interstitial water sulfate concentration to decrease rapidly in the upper few tens of meters below seafloor. Because the matrix solution was not a true blank, the procedural blank used was a dilution of the 1% nitric acid solution in the yttrium solution, and only the slope of the calibration curve was used for quantification. A stock standard solution was prepared from ultrapure primary standards (SPC Science PlasmaCAL) in the 1% nitric acid solution. The stock solution was then diluted in the same 1% ultrapure nitric acid solution to concentrations of 50%, 25%, 10%, 5%, and 1%. A 1.25 mL aliquot of each stock solution was added to 8.75 mL of matrix solution to produce a series of standards that could be diluted using the same method as the samples for consistency. The final matrix-matched 100% standard solution contained the following concentrations: B = 3000 µM, Li = 400 µM, Si = 1000 µM, Mn = 50 µM, Fe = 50 µM, Sr = 400 µM, and Ba = 200 µM. A standard prepared in the 10% matrix-matching solution was repeatedly analyzed to calculate the precision of the method. The average precision of the minor element analyses were B < 1%, Ba < 1%, Fe < 1.8%, Mn < 2%, Li < 1%, Si < 2%, and Sr < 1.5%, and the average accuracy of the analyses were B < 1.5%, Ba < 2%, Fe < 2%, Mn < 2%, Li < 2%, Si < 3%, and Sr < 4%.

Vanadium, copper, zinc, molybdenum, rubidium, cesium, lead, and uranium were analyzed by ICP-MS (Agilent 7500ce) equipped with an octopole reaction system to reduce polyatomic and double-charge interferences. To calibrate for interferences by the major ions Na, Cl, K, Ca, and S on some of the transition metals (ClO and SOH on V, Na and CaOH on Cu, and S on Zn), solutions were prepared containing these elements at concentrations similar to IAPSO standard seawater values. These solutions were analyzed at the beginning of each run, and an interference correction was applied based on the average counts per second (cps) measured on the standard solutions divided by the abundance of the interfering elements. This ratio was multiplied by the known concentration of the major ions in the samples based on previous analysis, and the result was subtracted from the measured cps of the sample. A 100 µL aliquot of 500 parts per billion (ppb) indium standard was added to the empty analysis vials before dilution. Sample aliquots were then diluted with the 1% nitric acid solution to 3% in these vials (150 µL sample with 4.85 mL of 1% HNO_3 solution) based on previous determination of the detection limits and the concentrations of the elements of interest. A primary standard solution that matched the maximum range of predicted concentrations was made based on published results of deep-sea interstitial water compositions in a variety of settings. The composition of the standard is as follows: V = 20 ppb; Cu, Mo, Pb, and U = 40 ppb; Zn = 140 ppb; Rb = 500 ppb; and Cs = 5 ppb. This primary standard was diluted in the 1% nitric acid solution to relative concentrations

of 50%, 25%, 10%, 5%, and 1%. These standards were then diluted to 3%, similar to the standard solutions, with the addition of 150 µL of a 560 mM NaCl solution and 4.7 mL of the 1% HNO_3 solution to account for matrix suppression of the plasma ionization efficiency. The 25% standard was diluted accordingly and analyzed every eight samples throughout every analysis series for precision and in order to compare the results from different analysis dates. Blanks were also analyzed every eight samples, and detection limits were determined as three times the standard deviation of a procedural blank of Milli-Q water acidified with 4 mL of optima-grade 6M HCl. The average precision of multiple determinations of the 10% ICP-MS standard was V < 6%, Cu < 14%, Zn < 3%, Mo < 0.8%, Rb < 0.7%, Cs < 12%, Pb < 3%, and U < 0.8%.

Gas chemistry

Safety gas monitoring and H_2 and CO

A 1 cm^3 sediment or deposit was collected with a cut-off plastic syringe or a corkscrew, usually from the exposed ends of every section of the retrieved core, and was extruded into a 20 mL glass vial containing 3 mL of Milli-Q water. Then the vial was placed in an oven at 70°C for 30 min. The evolved gases were analyzed using an Agilent 6890N gas chromatograph (GC) equipped with a flame ionization detector (FID) for CH_4 and other hydrocarbons (C_2–C_4) and a GL Science GC4000 GC equipped with a helium ionization detector (HID) for H_2 and CO. The GC-FID system determined the C_1–C_4 hydrocarbon concentration. Chromatographic response on the GC was calibrated against five different authentic standards with variable quantities of low molecular weight hydrocarbons. The GC-HID was brought on board the *Chikyu* for the JAMSTEC Subsurface Geobiology and Advanced Research (SUGAR) project as a third-party tool. Chromatographic response on the GC was calibrated against the prepared standard gas mixture (10 and 100 ppm of H_2, CH_4, and CO). After the measurement of H_2 and CO concentrations, the vial was again heated at 70°C for 30 min. The evolved gases were analyzed first with the GC-HID and then with the GC-FID.

Organic geochemistry

Total carbon, nitrogen, and sulfur contents of the solid phase

Solid-phase samples were taken at a frequency of 1–3 per core as individual samples for milling and XRF, XRD, carbonate, and CNS analyses. After drying and homogenizing the sample, total carbon, nitrogen, and sulfur concentrations were determined by elemental analysis using a Thermo Finnigan Flash EA 1112 carbon-hydrogen-nitrogen-sulfur (CHNS) analyzer. Calibration was based on the synthetic standard sulfanilamide, which contains 41.81 wt% carbon, 16.27 wt% nitrogen, and 18.62 wt% sulfur. About 20–50 mg of ground sediment was weighed and placed in a tin container for carbon and nitrogen analyses. For sulfur analysis, the same amount of sediment was weighed and put in a tin container with the same amount of V_2O_5 catalyst. Sediment samples were combusted at 1000°C in a stream of oxygen. Nitrogen oxides were reduced to N_2, and the mixture of CO_2, N_2, and SO_2 was separated by gas chromatography and detected by a thermal conductivity detector. The standard deviation of carbon, nitrogen, and sulfur concentrations for the samples is less than ±0.1%. Accuracy for carbon and sulfur analysis was confirmed using two GSJ reference samples.

Inorganic carbon, organic carbon, and carbonate content of the solid phase

In the same set of samples that was used for the analysis of total carbon, nitrogen, and sulfur contents of the solid phase, inorganic carbon concentration was determined using a Coulometrics 5012 CO_2 coulometer. About 10–20 mg of ground sediment was weighed and reacted with 2 M HCl. The liberated CO_2 was titrated, and the change in light transmittance was monitored with a photodetection cell. The weight percentage of calcium carbonate was calculated from the inorganic carbon content, assuming that all the evolved CO_2 was derived from dissolution of calcium carbonate, by the following equation:

$$CaCO_3\ (wt\%) = \text{inorganic carbon}\ (wt\%) \times 100/12. \quad (49)$$

No correction was made for the presence of other carbonate minerals. National Institute of Standards and Technology–Standard Reference Material (NIST-SRM) 88b was used to confirm accuracy. Standard deviation for the samples was less than ±0.1 wt%. Total organic carbon contents were calculated by subtraction of inorganic carbon from total carbon contents as determined by elemental analysis.

Microbiology

Whole-round sampling procedure

WRC samples were taken at a frequency of ~1 sample per 4.5 m of core recovered. A total 150 cm^3 of sediment or deposit was required for the subsequent microbiological investigation (see below), and a ~10 cm

length of whole round was retrieved from a portion of the section showing minimal disruption by drilling after evaluation by X-ray CT scan imaging. All subsampling and processing were carried out within 60 min of core arriving on deck.

Sample preparation for microscopic observations

Approximately 1 cm^3 of sediment or deposit sample was taken with a sterilized spatula. In a clean area of the laboratory, the samples were immediately fixed with 5 mL of 4% paraformaldehyde in a phosphate-buffered saline (PBS) buffer and stored at 4°C for 3 h. Fixed samples were preserved at –80°C. In addition to the chemically fixed samples, another 1 cm^3 of subsample was collected by a sterilized spatula and directly frozen at –80°C.

Sample preparation for molecular analyses

Approximately 20 cm^3 of sediment or deposit was collected with a sterilized spatula into Falcon 50 mL tubes for subsequent DNA/RNA analysis. These tubes were sealed in aluminum bags with oxygen absorbers and indicators in an anaerobic glove box and were stored at –80°C. Approximately 5 cm^3 of sediment or deposit was subsampled by a sterilized spatula into a 15 mL Falcon tube for later RNA analysis. The tubes were frozen with liquid nitrogen and stored at –80°C. Approximately 50 cm^3 of sediment or deposit was also collected into a Falcon 50 mL tube. The tubes were sealed in aluminum bags with oxygen absorbers and indicators in an anaerobic globe box and were then stored at –80°C.

Sample preparation for living microorganisms

Approximately 75 mL of sediment or deposit was subsampled by a sterilized spatula into a Schott 100 mL bottle and sealed with a black butyl rubber stopper in an anaerobic glove chamber. The gas phase of the bottle was exchanged with 100% nitrogen and stored at 4°C.

Contamination test

PFC (perfluoro-methylcyclohexane; MW 350.6) (Matrix Scientific, USA) was used as a chemical tracer for contamination assessment during coring operations. PFC tracer was added to the drilling mud tank every time a new batch of drilling mud fluid was prepared with surface seawater. After each new batch of drilling mud was prepared, a 50 cm^3 sample was collected to determine the concentration of PFC so that the contamination of core samples by drilling fluid could be assessed. Quantification of PFC in the core samples and original drilling mud was carried out following standard IODP procedures (Smith et al., 2000) using an Agilent Technologies model 6890N GC with an electron capture detector. The GC was equipped with a HP-PLOT Al_2O_3 "M" deactivation column (30 m long; 0.53 mm inside diameter [ID]; 15 µm coating thickness). Helium and nitrogen were used as the carrier gas and make-up gas, respectively. The extent of contamination was estimated by comparison of values between the mud fluid in the tank and the subsampled sediment or deposits. Sediment or deposit showing PFC concentrations <0.1% of that in the mud tank fluid are used as standards for reliable samples free from external contamination (Takai, Mottl, Nielsen, and the Expedition 331 Scientists, 2011).

Observatory and downhole measurements

Downhole temperature measurements at Site C0019 were made using independent miniature temperature loggers (MTLs). An observatory of 55 MTLs was installed to study the frictional heat of the fault zone, with the data to be recovered later. In addition, during drilling operations observations of temperature and pressure in the water column and borehole were performed with the temporary deployment of a free-fall MTL string.

MTL observatory

One of the main goals of Expedition 343 is to monitor the fault zone temperature following the 2011 Tohoku-oki earthquake in order to determine the level of frictional stress during the main shock rupture. Monitoring of subsurface temperature is being performed with observatory instrumentation installed in Hole C0019D. Each MTL independently records temperature data (some units also record depth/pressure). The instrument string will be retrieved by the *Kaiko* 7000II remotely operated vehicle (ROV) in February 2013 to obtain the data. The MTL observatory was installed in July 2012 during Expedition 343T.

Sensors

The MTL observatory consists of 55 autonomous MTLs attached to a rope on a recoverable hanger inside tubing. The tubing has one Exway ball valve at the bottom that allows water to be jetted out during installation but restricts influx of overpressured formation fluids. Three different types of MTLs are used: 10 TDR-2050s and 15 TR-1050s manufactured

by RBR Ltd. (Canada; www.rbr-global.com/) and 30 Antares 1357 high-pressure data loggers manufactured by Antares Datensysteme GmbH (Germany; www.antares-geo.de/). The different instrument types are collectively referred to as "the RBRs" and "the Antares." All instruments have temperature sensors and an autonomous data logger and are enclosed within titanium casings pressure rated for up to 10,000 m water depth. The TDR-2050s also have a pressure sensor that effectively records the sensor's water depth inside the cased borehole. The RBRs are 230 mm × 38 mm, and the Antares are 190 mm × 20 mm in dimension. The RBR temperature sensors have a resolution of <0.00005°C and accuracy of <0.001°C. The Antares temperature sensors have a resolution of 0.001°C and accuracy of <0.1°C.

Rope

Roughly 1000 m of rope was prepared on which the MTLs are attached. The rope consists of 10 mm dynama-spectra containing spliced eyelets at predetermined locations for attaching the instruments. The rope is slightly negatively buoyant to prevent tangling with ROV cables if the rope breaks during recovery. The overall length consists of nine separate rope sections (R0–R8) whose length and eyelet positions are listed in Table T9. Each section has loops at the end allowing simple connections to each other. The MTLs are connected to the spliced eyelets with 2 or 3 mm spectra rope cord that is looped through holes in the instrument and knotted with a double fisherman's knot. Rope R8 does not contain pre-spliced eyelets. On this rope section, eyelets were made using 3 mm cord and a series of prusik knots that were wrapped in electrical tape to prevent movement along the rope.

Coverings

The MTLs are surrounded with rubber coverings to help secure them to the rope, protect them from the effects of banging against the tubing wall, and create a smooth edge between the rope and MTL to help avoid getting caught on tubing joints during installation and recovery. The method of covering and attachment of MTLs is adapted from a similar MTL string deployment during IODP Expedition 327. Figure F21 shows pictures of the sensors and their attachment on the rope within their protective coverings. The coverings for the Antares are made of general-purpose air and water service rubber hose with an ID of 1 inch. The coverings for the RBRs have similar form and are cut from sheets of ¼ inch thick black rubber and wrapped around each instrument and the rope. The covering material is cut with tapered ends to lengths a few inches longer than the MTL. The extra space above and below the instrument helps ensure it is protected. A slit is cut down the center of the hose to easily get the MTL in. For the RBR coverings, this slit location marks where the sheeting material is joined when wrapped around the rope and instrument. The slits are on the far side of the instrument away from the rope. Holes were either drilled into the sides of the hose material or poked through the tape material to allow fluid movement around the instruments as a means to help prevent corrosion.

Each MTL is connected to the splice with pieces of cord using a double fisherman's knot. The hose is connected to the rope by a zip tie through two ¼ inch holes drilled through each tapered end of the covering. The zip tie junction is made within the inner part of the covering. Both the MTL and rope are enclosed within the covering. The RBR coverings are kept closed by wraps of duct tape. All coverings are further secured by several wraps of 3M Super 88 electrical tape around both tapered ends and near the center of the covering for the Antares. The wraps of tape on at least the upper ends are also covered in the opposite wrap direction with friction tape (either 3M 1755 or similar "hockey tape"). The maximum diameter of the covered sensors on the string is 55 and 34.5 mm for the RBRs and Antares, respectively.

Hanger

MTL string Rope R7 was payed out from a spool during installation and cut to length to set the configuration of sensors around the target fault zone depth. A loop splice was made of the cut end of rope and attached to a hanger that sits within the wellhead. The hanger has a ring at the end to allow the ROV *Kaiko* to grab and retrieve the entire sensor string several months later. The top of the observatory, including the hanger which sits within the casing hanger wellhead, is illustrated in Figure F22.

Sinker bar

A 0.41 m sinker bar weighing 10 kg (8.73 kg in water) is attached at the bottom of the MTL string to ensure the rope hangs straight and does not bunch up during installation. The configuration at the lower end of the observatory is illustrated in Figure F23 and shown Figure F21E.

Weak links/Rope connections

An issue concerning the eventual retrieval of the MTL string is the potential risk of afterslip along the fault that may constrict the tubing walls and restrict passage of the MTL string out of the borehole. To maximize MTL recovery, three weak links are used to

connect some segments of rope. The weak links were obtained from TLR, Inc. (Carmel, California, USA; www.tlrinc.biz/) and were specifically designed for this expedition in order to have a small diameter and relatively smooth profile to avoid getting caught in the tubing, as well as having breaking strengths below 300 kgf of tension, which is the maximum safety limit for pulling by the ROV *Kaiko* during recovery. The breaking strength is controlled by the number of polyvinyl strands sewn through the connecting members of the two sides of the weak link. The weakest weak link has three strands, and the strongest has six. The positions of the weak links and their tested strengths are listed in Table T9.

Where weak links are not used, most rope sections are connected by passing the rope through the end loop of the adjacent section creating a square knot with the two section loops. Ropes R5 and R6 are connected with a locking carabiner that is then wrapped in tape to ensure a smooth profile along the rope.

Sensor programming

The spacing between instruments is variable, with 1.5 m spacing across the target fault zone area and increased spacing further away. The positions relative to both the target fault zone and seafloor, and accounting for rope stretch, were determined during installation. The calculated positions are listed in Table T9. With a few exceptions, all instruments are programmed to record for at least 6 months until the planned retrieval by the ROV *Kaiko* in February 2013. The instruments are programmed to begin logging at 00:00:00 h Japan Standard Time (JST) on 13 July 2012, with the exception of the RBR sensors on Ropes R4, R5, and R8, which are programmed to begin logging at 00:00:00 h JST on 15 April 2012. All sensors have had their clocks reset to "PC time," which was updated against an Internet timeserver and set to JST. The Antares are programmed to record every 10 min, the TDR-1050s are set to record every 10 s, and the TDR-2050s are set to record every 20 s. The exception to this programming schedule is two TDR-2050s scheduled to record at 1 s intervals for ~16 days; Sensor 32 will start at 00:00:00 h on 15 October 2012 and Sensor 47 will start at 00:00:00 h on 8 February 2013. These times cover the expected duration of the two possible recovery expeditions and will allow profile logs to be taken during extraction of the MTL string. The duration of recording is limited by the memory capacity of the instruments.

Observatory construction

The observatory is constructed of 4½ inch ID steel tubing with a 20 inch casing hanger wellhead on top in which the MTL sensor string was inserted and lowered. The hanger holding the sensor string rests within the casing hanger wellhead. The sensor string was lowered into the entire constructed length of the tubing while it extended beneath the casing hanger wellhead on the rig floor. All ropes with the exceptions of Ropes R6 and R7 were raised and lowered with tuggers that grab sections of the rope with the help of loops of rope temporarily attached to the sensor string using prusik knots. After the lower ropes with dense sensor spacing were lowered, Ropes R6 and R7 were lowered from a spool, and the uppermost sensors were attached on the rig floor as the rope was lowered. When the total estimated length of the sensor string was approached, lowering was completed by tuggers again and the weight of the sensor string was monitored with a load cell. A reduction in weight comparable to the weight of the sinker bar indicated that the sensor string reached the bottom of the tubing. The position of the rope at the top of the wellhead was then marked and cut to make a looped eyelet at a position 4.54 m shorter that will hang from the hanger. This length of shortening allowed 1.18 m for the length of the hanger that lies below the top of the wellhead and an allowance of 3.36 m of free space below the sinker bar and the top of the float collar marking the bottom inside of the tubing. The overall marked length of rope was then compared with the true length of the tubing and casing hanger wellhead to calibrate estimates of rope stretch along the sensor string and to calculate the positions of the sensors relative to each other and the seafloor (Table T9).

Installation

With the sensor string and hanger in the tubing, the casing hanger wellhead was joined to a casing running tool at the bottom of the drill string. Circulation tests were conducted before lowering of the observatory to the floor, and the weight of the entire sensor string was measured before and after to confirm that the weak links survive circulation forces. The casing running tool and drill string was then connected to the casing hanger wellhead again, and the observatory was lowered to the seafloor. Near the seafloor, an underwater television camera system with two television cameras and a sonar device connected to the *Chikyu* by fiber-optic cable was sent down the drill string to the bottom of the observatory to find the seafloor wellhead and guide reentry. Upon reentry of the wellhead by the tubing, the observatory was lowered until the casing hanger wellhead rested securely atop the seafloor wellhead. A dart and sinker bar attached to the core line winch was then lowered down the drill string to plug the

casing hanger running tool, allowing a buildup of pressure within the running tool and causing the running tool to release and the observatory to remain in place.

Free-fall MTL string

Background

Temperature and pressure (depth) measurements in the water and subsurface were conducted using instrumentation deployed within the drill pipe while in Hole C0019E. These measurements allow immediate monitoring of the temperature disturbance caused by drilling and may allow estimation of formation temperatures at different depths. The "free-fall MTL string" consists of 1–3 autonomous MTLs covered in rubber protectors that are tied to one another with spectra cord and installed at the bottom of an empty core barrel with a deplugger nozzle at the end instead of a core catcher. The whole inner core barrel assembly containing the MTLs was dropped to the bottom of the drill string by free fall from the rig floor. The core barrel containing the free-fall MTL string was then recovered as the pipe was recovered or independently by latching onto the inner core barrel with a sinker bar and pulling the assembly up with the core line winch. Pulling it back to the surface allows for a continuous temperature-depth profile that may highlight anomalous intervals.

Sensors

The instruments used were TDR-2050s, as described in **"MTL observatory."** The sampling interval was set to record once every 1 s.

Coverings

The MTLs are covered with rubber sleeves to aid in securing them to one another and protect them from the effects of shock. The sleeve coverings are made of general-purpose air and water service rubber hose with 38 mm (1½ inch) ID. The maximum diameter of the sensors with rubber sleeves is 51 mm (2 inches). The rubber hose is cut to lengths a few inches longer than the sensors and are tapered on each end (Fig. **F24**). Extra space within the covering above and below the MTL helps ensure the MTL is protected. Each hose covering is longitudinally split to allow easy insertion and recovery of the MTLs between deployments. The hose covering has six ½ inch holes drilled into the sides to allow fluid movement around the sensor. To ensure the coverings lie flat length-wise and do not curl and get stuck within the core liner at an arbitrary depth above the bottom, extra slits are cut on the backside of the hose perpendicular to the length and ending in the side holes. The tapered ends are rounded to prevent them from clogging the deplugger nozzle at the bottom of the core barrel or jamming within the core liner.

Connections

Each MTL is connected to the rubber covering with separate loops of 2 and 3 mm Spectra cordage looped through holes in the sensor and two ¼ inch holes drilled into the top of the top taper of rubber hose. The second loop is for backup in case a loop breaks. The cord loops are tied using a double fisherman's knot on the inside of the rubber hose covering. The coverings and MTLs are further secured by several diagonal wraps of 3M Super 88 electrical tape around the covering (Fig. **F24**).

The sensors covered in rubber are connected directly above each other with loops of 3 mm cordage looped through two ¼ inch holes drilled into the tapered ends of coverings, which are oriented in opposing directions. The cord loops are tied within the joint created by the two sleeves with a double fisherman's knot. The final arrangement looks like a snake (Fig. **F24**).

Deployment

The connected MTLs are placed within the bottom of a plastic core liner installed in an empty core barrel (Fig. **F24B**). The MTL string is not secured to anything. Instead of a core catcher at the bottom, the core barrel is closed at the bottom with a narrow tipped deplugger nozzle (Fig. **F24C**). The whole core barrel assemblage is deployed by free fall and recovered with the core line winch or removed from the bottom of the drill string on the rig floor.

Core-log-seismic integration

During Expedition 343, we used LWD data and core measurement data (see **"Physical properties"** and **"Logging while drilling"** for background on data collection and processing) to establish ties to the seismic data obtained in 2011 after the Tohoku-oki earthquake.

Seismic data

The high-resolution seismic data set was obtained by JAMSTEC during the KY11-E05 cruise in October and November 2011 of the R/V *Kaiyo*. The sounding source was a 320 in^3 cluster gun array, and the shot interval was 37.5 m. The receiver was a 1.3 km, 192 channel digital streamer cable with 6.25 m channel spacing. The maximum offset was too short for velocity analysis at the target depth of this expedition.

The velocity model used for stacking and poststack time migration was obtained from analysis of another multichannel seismic survey, KR11-E03, which was obtained with a 6 km streamer cable. Specifically, a velocity model obtained from stacking velocity analysis of Line D05, located 4 km south of our drill site, was used. The above velocity model resulted in a migrated image that was obscured by migration noise, so we adopted a constant velocity model of 1525 m/s, which appropriately migrated the seafloor reflection and resulted in a much better image of the deeper part.

Depth conversion of the seismic data

In order to accurately correlate the core, log, and seismic data, we needed to convert the seismic reflection profiles to depth sections. Sonic logging and a check shot survey were not conducted during Expedition 343, so for initial depth conversion we converted and slightly modified the root mean square velocity model obtained from the prestack time migration velocity analysis of Line D05 to interval velocity. The resulting depth section was later calibrated using the logging and core measurements collected during the expedition. The final calibrated depth section was used for core-log-seismic integration purposes.

Synthetic seismograms

We created synthetic seismograms to help correlate the LWD logs with the high-resolution seismic data. Density and sonic wave velocity were not directly measured during LWD; therefore, in order to create a reflectivity series and synthetic seismograms, these data were estimated using resistivity logs. The method used to calculate density is detailed in **"Logging while drilling."** Velocity was calculated from estimated density with the following empirical relationship:

$$V = 304800/(241.011 - 43.346\rho), \qquad (50)$$

where V is velocity and ρ is the estimated bulk density. This relationship was determined by cross-plotting density and sonic velocity recorded from ODP Leg 186 Sites 1150 and 1151 and later using measurements from discrete core samples. The synthetic seismograms were compared with the seismic section to help match the depth of the main reflectors and provide a quality check of the logging and core measurement data used to calculate the synthetic seismograms. Both Petrel (by Schlumberger) and Geolog/SeisEarth (by Paradigm) software packages were used to construct synthetic seismograms.

References

ASTM International, 1990. Standard method for laboratory determination of water (moisture) content of soil and rock (Standard D2216–90). In *Annual Book of ASTM Standards for Soil and Rock* (Vol. 04.08): Philadelphia (Am. Soc. Testing Mater.). [revision of D2216-63, D2216-80]

Blum, P., 1997. Physical properties handbook: a guide to the shipboard measurement of physical properties of deep-sea cores. *ODP Tech. Note,* 26. **doi:10.2973/odp.tn.26.1997**

Bonner, S., Fredette, M., Lovell, J., Montaron, B., Rosthal, R., Tabanou, J., Wu, P., Clark, B., Mills, R., and Williams, R., 1996. Resistivity while drilling—images from the string. *Oilfield Rev.,* 8(1):4–19. **http://www.slb.com/~/media/Files/resources/oilfield_review/ors96/spr96/composite.ashx**

Bonner, S.D., Tabanou, J.R., Wu, P., Seydoux, J.P., Moriarty, K.A., Seal, B.K., Kwok, E.Y., and Kuchenbecker, M.W., 1995. New 2-MHz multiarray borehole-compensated resistivity tool developed for MWD in slim holes. *Proc.—SPE Annu. Tech. Conf.,* Pap. SPE 30547. **doi:10.2118/30547-MS**

Bourlange, S., Henry, P., Moore, J.C., Mikada, H., and Klaus, A., 2003. Fracture porosity in the décollement zone of Nankai accretionary wedge using logging-while-drilling resistivity data. *Earth Planet. Sci. Lett.,* 209(1–2):103–112. **doi:10.1016/S0012-821X(03)00082-7**

Carlson, R.L., and Christensen, N.I., 1977. Velocity anisotropy and physical properties of deep-sea sediments from the western South Atlantic. *In* Supko, P.R., Perch-Nielsen, K., et al., *Init. Repts. DSDP,* 39: Washington, DC (U.S. Govt. Printing Office), 555–559. **doi:10.2973/dsdp.proc.39.124.1977**

Chang, C., McNeill, L.C., Moore, J.C., Lin, W., Conin, M., and Yamada, Y., 2010. In situ stress state in the Nankai accretionary wedge estimated from borehole wall failures. *Geochem., Geophys., Geosyst.,* 11:Q0AD04. **doi:10.1029/2010GC003261**

Expedition 308 Scientists, 2006. Methods. *In* Flemings, P.B., Behrmann, J.H., John, C.M., and the Expedition 308 Scientists, *Proc. IODP,* 308: College Station, TX (Integrated Ocean Drilling Program Management International, Inc.). **doi:10.2204/iodp.proc.308.102.2006**

Expedition 316 Scientists, 2009a. Expedition 316 methods. *In* Kinoshita, M., Tobin, H., Ashi, J., Kimura, G., Lallemant, S., Screaton, E.J., Curewitz, D., Masago, H., Moe, K.T., and the Expedition 314/315/316 Scientists, *Proc. IODP,* 314/315/316: Washington, DC (Integrated Ocean Drilling Program Management International, Inc.). **doi:10.2204/iodp.proc.314315316.132.2009**

Expedition 316 Scientists, 2009b. Expedition 316 Site C0004. *In* Kinoshita, M., Tobin, H., Ashi, J., Kimura, G., Lallemant, S., Screaton, E.J., Curewitz, D., Masago, H., Moe, K.T., and the Expedition 314/315/316 Scientists, *Proc. IODP,* 314/315/316: Washington, DC (Integrated Ocean Drilling Program Management International, Inc.). **doi:10.2204/iodp.proc.314315316.133.2009**

Expedition 322 Scientists, 2010. Methods. *In* Saito, S., Underwood, M.B., Kubo, Y., and the Expedition 322 Scientists, *Proc. IODP,* 322: Tokyo (Integrated Ocean Drilling Program Management International, Inc.). **doi:10.2204/iodp.proc.322.102.2010**

Expedition 331 Scientists, 2011. Methods. *In* Takai, K., Mottl, M.J., Nielsen, S.H., and the Expedition 331 Scientists, *Proc. IODP,* 331: Tokyo (Integrated Ocean Drilling Program Management International, Inc.). **doi:10.2204/iodp.proc.331.102.2011**

Expedition 343/343T Scientists, 2013. Site C0019. *In* Chester, F.M., Mori, J., Eguchi, N., Toczko, S., and the Expedition 343/343T Scientists, *Proc. IODP,* 343/343T: Tokyo (Integrated Ocean Drilling Program Management International, Inc.). **doi:10.2204/iodp.proc.343343T.103.2013**

Fuller, M., 1969. Magnetic orientation of borehole cores. *Geophysics,* 34(5):772–774. **doi:10.1190/1.1440047**

GE Healthcare, 2006. *LightSpeed Series Learning and Reference Guide-Multi Slice CT:* Waukesha, Wisconsin (GE Healthcare).

Gieskes, J.M., Gamo, T., and Brumsack, H., 1991. Chemical methods for interstitial water analysis aboard *JOIDES Resolution*. *ODP Tech. Note,* 15. **doi:10.2973/odp.tn.15.1991**

Kamikuri, S., Nishi, H., and Motoyama, I., 2007. Effects of late Neogene climatic cooling on North Pacific radiolarian assemblages and oceanographic conditions. *Palaeogeogr., Palaeoclimatol., Palaeoecol.,* 249(3–4):370–392. **doi:10.1016/j.palaeo.2007.02.008**

Kamikuri, S., Nishi, H., Motoyama, I., and Saito, S., 2004. Middle Miocene to Pleistocene radiolarian biostratigraphy in the Northwest Pacific Ocean, ODP Leg 186. *Isl. Arc,* 13(1):191–226. **doi:10.1111/j.1440-1738.2003.00421.x**

Kimura, G., Silver, E.A., Blum, P., et al., 1997. *Proc. ODP, Init. Repts.,* 170: College Station, TX (Ocean Drilling Program). **doi:10.2973/odp.proc.ir.170.1997**

Kirschvink, J.L., 1980. The least-squares line and plane and the analysis of palaeomagnetic data. *Geophys. J. R. Astron. Soc.,* 62(3):699–718. **doi:10.1111/j.1365-246X.1980.tb02601.x**

Kodama, K.P., 1984. Palaeomagnetism of granitic intrusives from the Precambrian basement under eastern Kansas: orienting drill cores using secondary magnetization components. *Geophys. J. R. Astron. Soc.,* 76(2):273–287. **doi:10.1111/j.1365-246X.1984.tb05045.x**

Manheim, F.T., and Sayles, F.L., 1974. Composition and origin of interstitial waters of marine sediments, based on deep sea drill cores. *In* Goldberg, E.D. (Ed.), *The Sea* (Vol. 5): *Marine Chemistry: The Sedimentary Cycle:* New York (Wiley), 527–568.

Mazzullo, J., and Graham, A.G. (Eds.), 1988. Handbook for shipboard sedimentologists. *ODP Tech. Note,* 8. **doi:10.2973/odp.tn.8.1988**

Mazzullo, J.M., Meyer, A., and Kidd, R.B., 1988. New sediment classification scheme for the Ocean Drilling Program. *In* Mazzullo, J.M., and Graham, A.G. (Eds.), *Handbook for shipboard sedimentologists*. ODP Tech. Note, 8:45–67. **doi:10.2973/odp.tn.8.1988**

McCave, I.N., Manighetti, B., and Robinson, S.G., 1995. Sortable silt and fine sediment size/composition slicing: parameters for palaeocurrent speed and palaeoceanography. *Paleoceanography,* 10(3):593–610. **doi:10.1029/94PA03039**

Mees, F., Swennen, R., Van Geet, M., and Jacobs, P., 2003. Applications of X-ray computed tomography in the geosciences. *Geol. Soc. Spec. Publ.,* 215(1):1–6. **doi:10.1144/GSL.SP.2003.215.01.01**

Moore, G.F., Taira, A., Klaus, A., et al., 2001. *Proc. ODP, Init. Repts.,* 190: College Station, TX (Ocean Drilling Program). **doi:10.2973/odp.proc.ir.190.2001**

Nakano, T., Nakashima, Y., Nakamura, K., and Ikeda, S., 2000. Observation and analysis of internal structure of rock using X-ray CT. *Chishitsugaku Zasshi,* 106(5):363–378. **doi:10.5575/geosoc.106.363**

Parés, J.M., Hassold, N.J.C., Rea, D.K., and van der Pluijm, B.A., 2007. Paleocurrent directions from paleomagnetic reorientation of magnetic fabrics in deep-sea sediments at the Antarctic Peninsula Pacific margin (ODP Sites 1095, 1101). *Mar. Geol.,* 242(4):261–269. **doi:10.1016/j.margeo.2007.04.002**

Paterson, M.S., and Wong, T., 2005. *Experimental Rock Deformation—The Brittle Field:* Berlin (Springer-Verlag).

Rothwell, R.G., 1989. *Minerals and Mineraloids in Marine Sediments: An Optical Identification Guide:* London (Elsevier).

Sacks, I.S., Suyehiro, K., Acton, G.D., et al., 2000. *Proc. ODP, Init. Repts.,* 186: College Station, TX (Ocean Drilling Program). **doi:10.2973/odp.proc.ir.186.2000**

Saffer, D., McNeill, L., Byrne, T., Araki, E., Toczko, S., Eguchi, N., Takahashi, K., and the Expedition 319 Scientists, 2010. *Proc. IODP,* 319: Tokyo (Integrated Ocean Drilling Program management International, Inc.). **doi:10.2204/iodp.proc.319.2010**

Sakamoto, T., Kuroki, K., Sugawara, T., Aoike, K., Iijima, K., and Sugisaki, S., 2006. Non-destructive X-ray fluorescence (XRF) core-imaging scanner, TATSCAN-F2. *Sci. Drill.*, 2:37–39. **http://www.iodp.org/iodp_journals/9_Non_Destructive_X_Ray_SD2.pdf**

Sanfilippo, A., Westberg-Smith, M.J., and Riedel, W.R., 1985. Cenozoic Radiolaria. *In* Bolli, H.M., Saunders, J.B., and Perch-Nielsen, K. (Eds.), *Plankton Stratigraphy* (Vol. 2): *Radiolaria, Diatoms, Silicoflagellates, Dinoflagellates, and Ichthyoliths:* Cambridge (Cambridge Univ. Press), 631–712.

Scientific Party, 1980. *Init. Repts. DSDP,* 56, 57: Washington, DC (U.S. Govt. Printing Office). **doi:10.2973/dsdp.proc.5657.1980**

Shepard, F.P., 1954. Nomenclature based on sand-silt-clay ratios. *J. Sediment. Petrol.,* 24(3):151–158. **http://jsedres.sepmonline.org/cgi/reprint/24/3/151.pdf**

Shibuya, H., Merrill, D.L., Hsu, V., and Leg 124 Shipboard Scientific Party, 1991. Paleogene counterclockwise rotation of the Celebes Sea—orientation of ODP cores utilizing the secondary magnetization. *In* Silver, E.A., Rangin, C., von Breymann, M.T., et al., *Proc. ODP, Sci. Results,* 124: College Station, TX (Ocean Drilling Program), 519–523. **doi:10.2973/odp.proc.sr.124.169.1991**

Shipboard Scientific Party, 2001. Explanatory notes. *In* Moore, G.F., Taira, A., Klaus, A., et al., *Proc. ODP, Init. Repts.,* 190: College Station, TX (Ocean Drilling Program), 1–51. **doi:10.2973/odp.proc.ir.190.103.2001**

Shipley, T.H., Ogawa, Y., Blum, P., et al., 1995. *Proc. ODP, Init. Repts.,* 156: College Station, TX (Ocean Drilling Program). **doi:10.2973/odp.proc.ir.156.1995**

Smith, D.C., Spivack, A.J., Fisk, M.R., Haveman, S.A., and Staudigel, H., 2000. Tracer-based estimates of drilling-induced microbial contamination of deep sea crust. *Geomicrobiol. J.,* 17(3):207–219. **doi:10.1080/01490450050121170**

Syvitski, J.P.M. (Ed.), 1991. *Principles, Methods, and Application of Particle Size Analysis*: Cambridge (Cambridge Univ. Press).

Taira, A., Hill, I., Firth, J.V., et al., 1991. *Proc. ODP, Init. Repts.,* 131: College Station, TX (Ocean Drilling Program). **doi:10.2973/odp.proc.ir.131.1991**

Takai, K., Mottl, M.J., Nielsen, S.H., and the Expedition 331 Scientists, 2011. *Proc. IODP,* 331: Tokyo (Integrated Ocean Drilling Program Management International, Inc.). **doi:10.2204/iodp.proc.331.2011**

Vacquier, V., 1985. The measurement of thermal conductivity of solids with a transient linear heat source on the plane surface of a poorly conducting body. *Earth Planet. Sci. Lett.,* 74(2–3):275–279. **doi:10.1016/0012-821X(85)90027-5**

Vrolijk, P., Fisher, A., and Gieskes, J., 1991. Geochemical and geothermal evidence for fluid migration in the Barbados accretionary prism (ODP Leg 110). *Geophys. Res. Lett.,* 18(5):947–950. **doi:10.1029/91GL00913**

Yamano, M., Kinoshita, M., and Goto, S., 2008. High heat flow anomalies on an old oceanic plate observed seaward of the Japan Trench. *Int. J. Earth Sci.,* 97(2):345–352. **doi:10.1007/s00531-007-0280-1**

Zoback, M.D., 2007. *Reservoir Geomechanics:* Cambridge (Cambridge Univ. Press).

Publication: 19 July 2013
MS 343343T-102

Figure F1. IODP conventions for naming sites, holes, cores, and samples. mbsl = meters below sea level, mbsf = meters below seafloor.

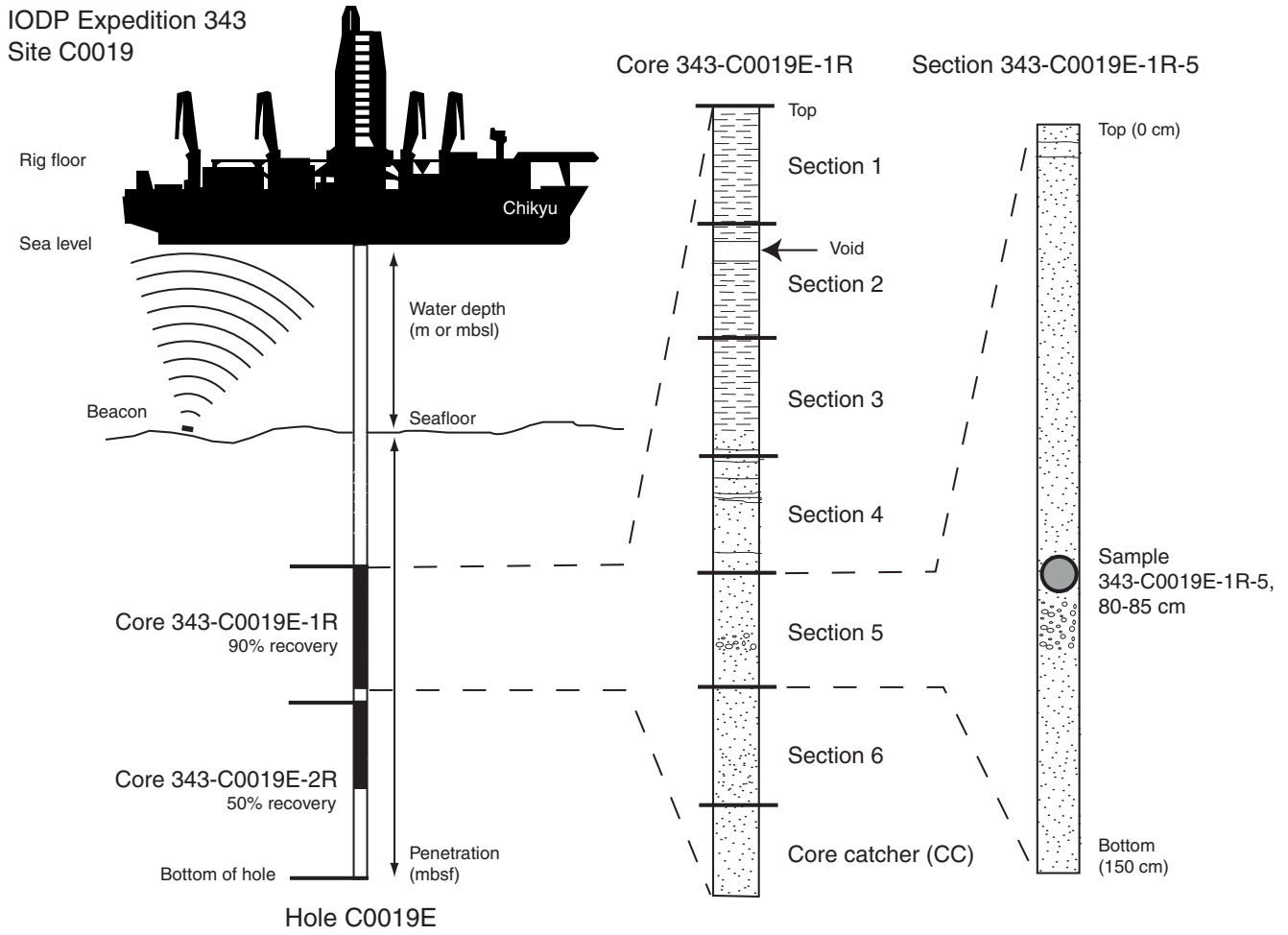

Figure F2. Diagram of the core flow followed during Expedition 343. JFAST = Japan Trench Fast Drilling Project. sect = section. X-CT = X-ray computed tomography. WRC = whole-round core. HS = headspace, MSCL-W = whole-round multisensor core logger, GRA = gamma ray attenuation, PWV = *P*-wave velocity, MS = magnetic susceptibility, NCR = noncontact resistivity, NGR = natural gamma radiation. VCD = visual core description. MSCL-I = photo image logger, MSCL-C = color spectroscopy logger. XRD = X-ray diffraction, XRF = X-ray fluorescence, ICP-AES = inductively coupled plasma–atomic emission spectroscopy, UV = ultraviolet, ICP-MS = inductively coupled plasma–mass spectrometry. MWJ = Marine Works Japan.

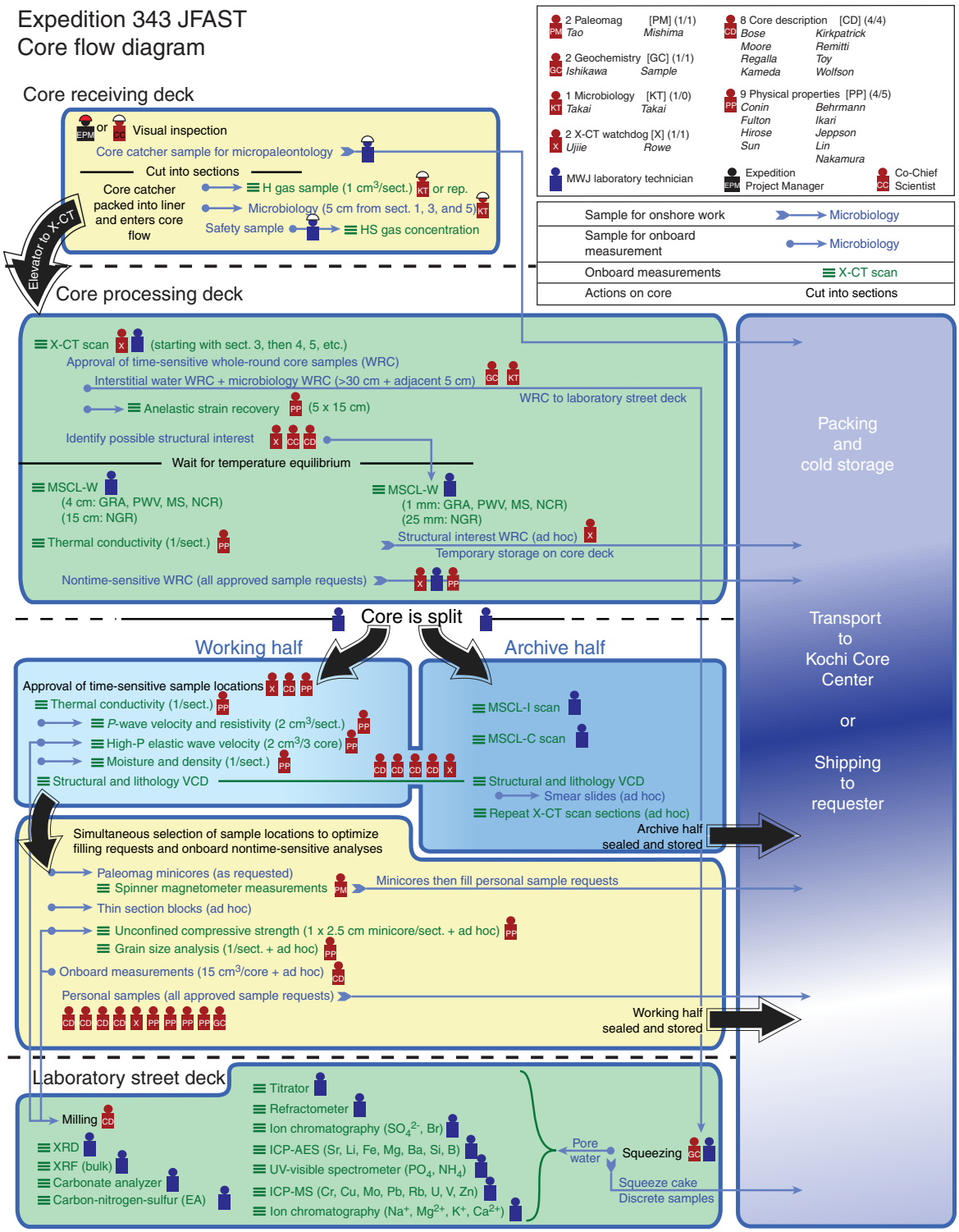

Figure F3. Sketch of the LWD/MWD BHA, Expedition 343. Drill string includes, from the bottom up: an 8½ inch bit, geoVISION sensor, arcVISION sensor, and TeleScope sensor with measurement points attached. D&I = declination and inclination, GR = gamma ray. Additionally, ring, buttons, and resistivity are resistivity measurement points.

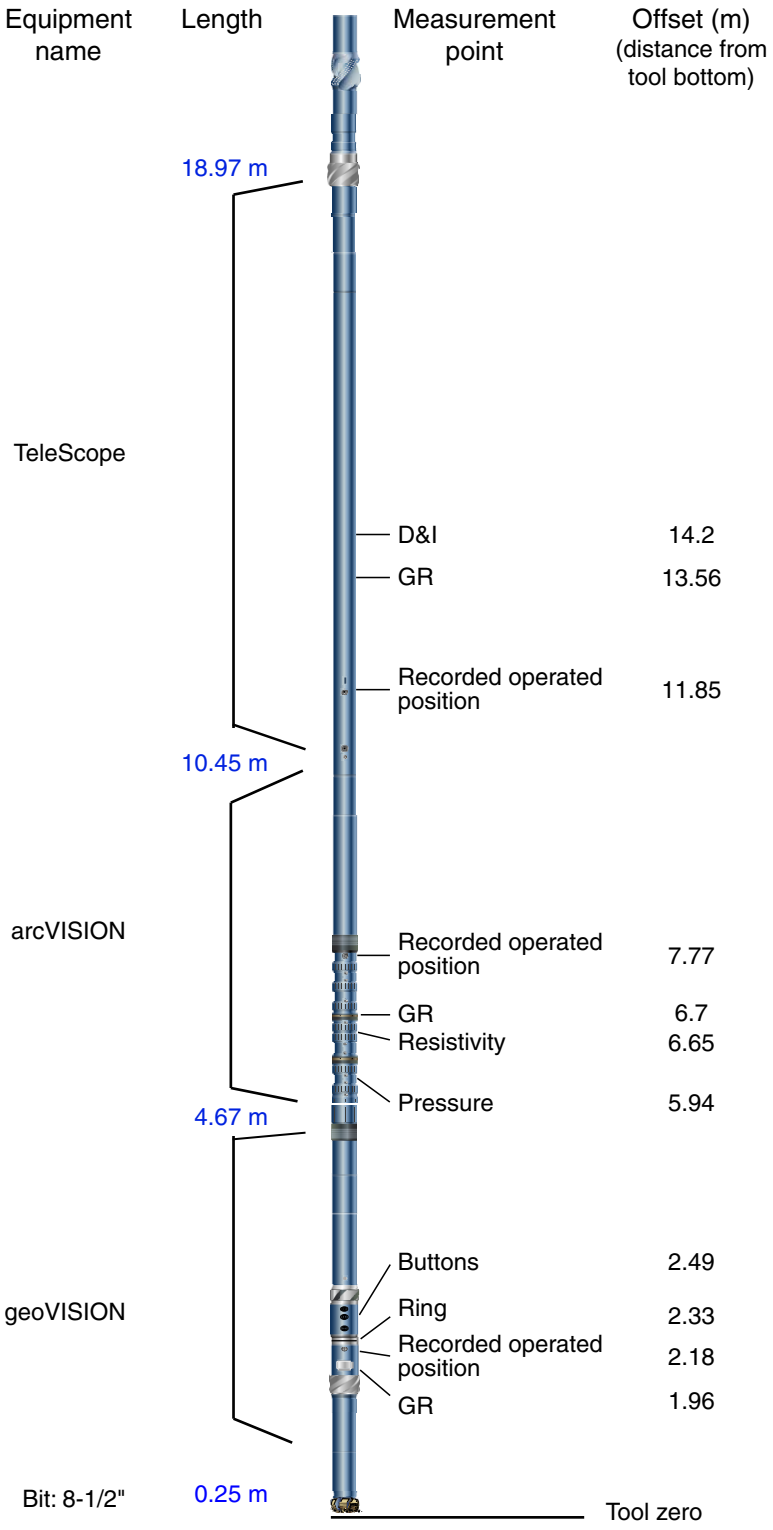

Figure F4. A. Schematic of rig instrumentation, Expedition 343. Crown-mounted motion compensator increases the accuracy of bit weight measurement and decreases heave influence on the drill string. MWD = measurement while drilling. **B.** Photo showing depth tracking system at "Deadline anchor" position in A.

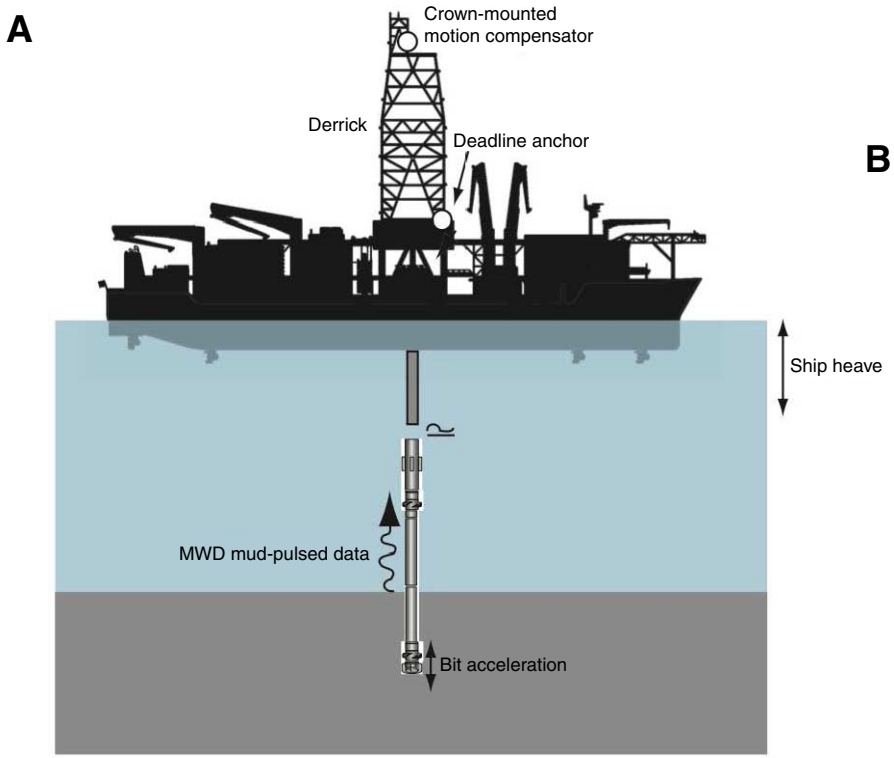

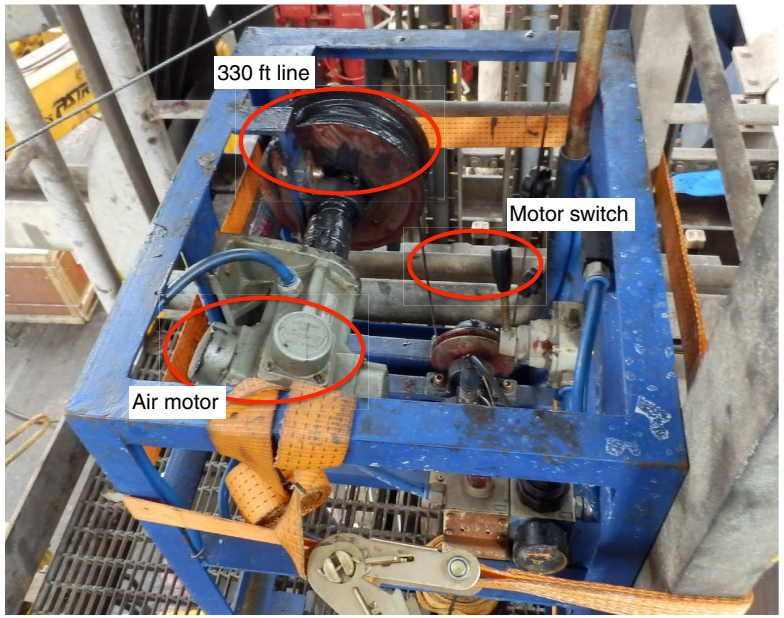

Figure F5. Position and components of the LWD/MWD tools, Expedition 343. GR = gamma ray, D&I = declination and inclination. **A.** geoVISION tool. **B.** arcVISION tool. **C.** TeleScope tool.

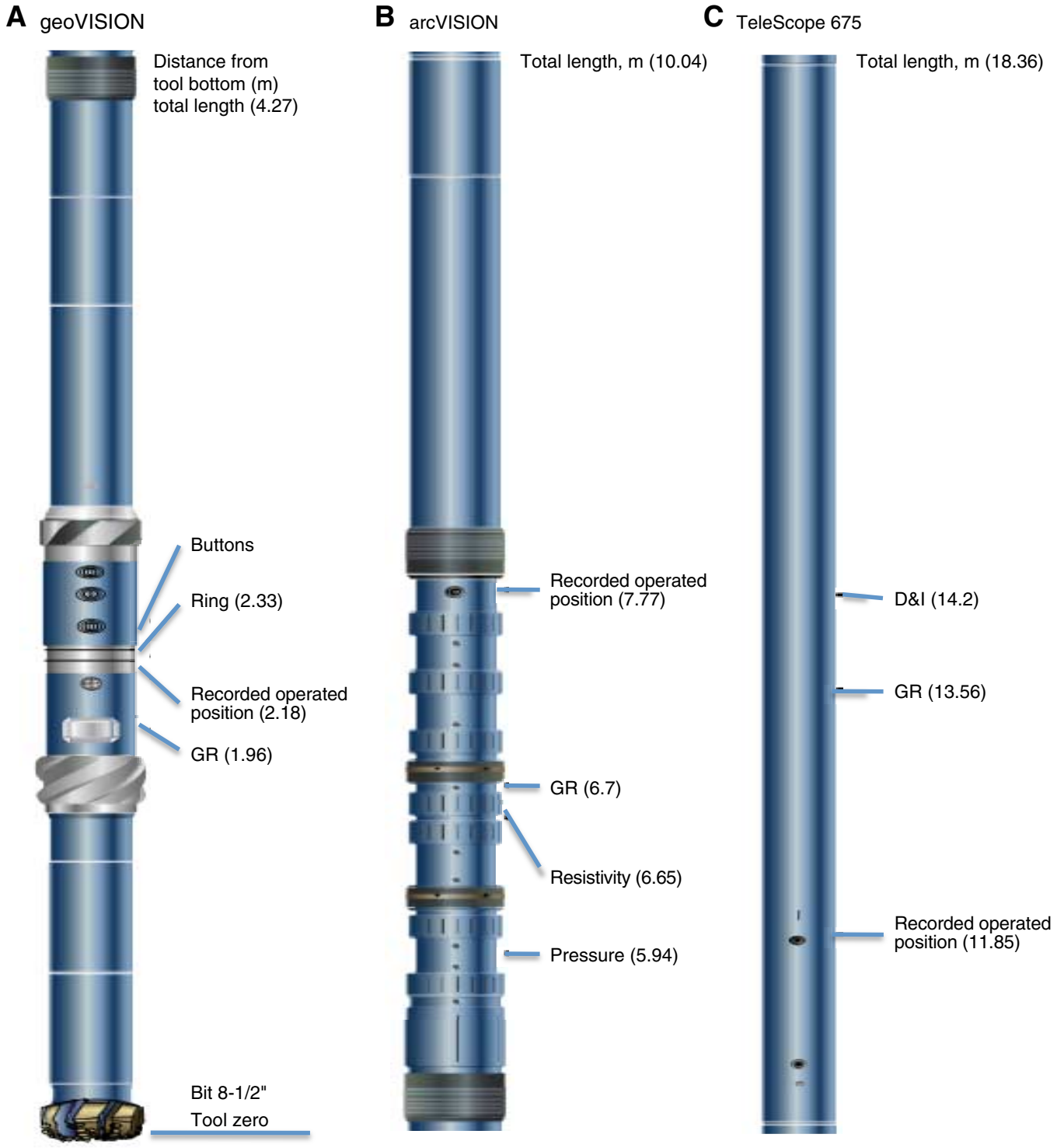

Figure F6. Shipboard structure and data flow, Expedition 343. MWD = measurement while drilling, LWD = logging while drilling, RT = real-time, RM = retrieved memory, PDF = portable document format, LAS = log ASCII standard, DLIS = digital log information standard, DCS = data consulting service, CDEX = Center for Deep Earth Exploration.

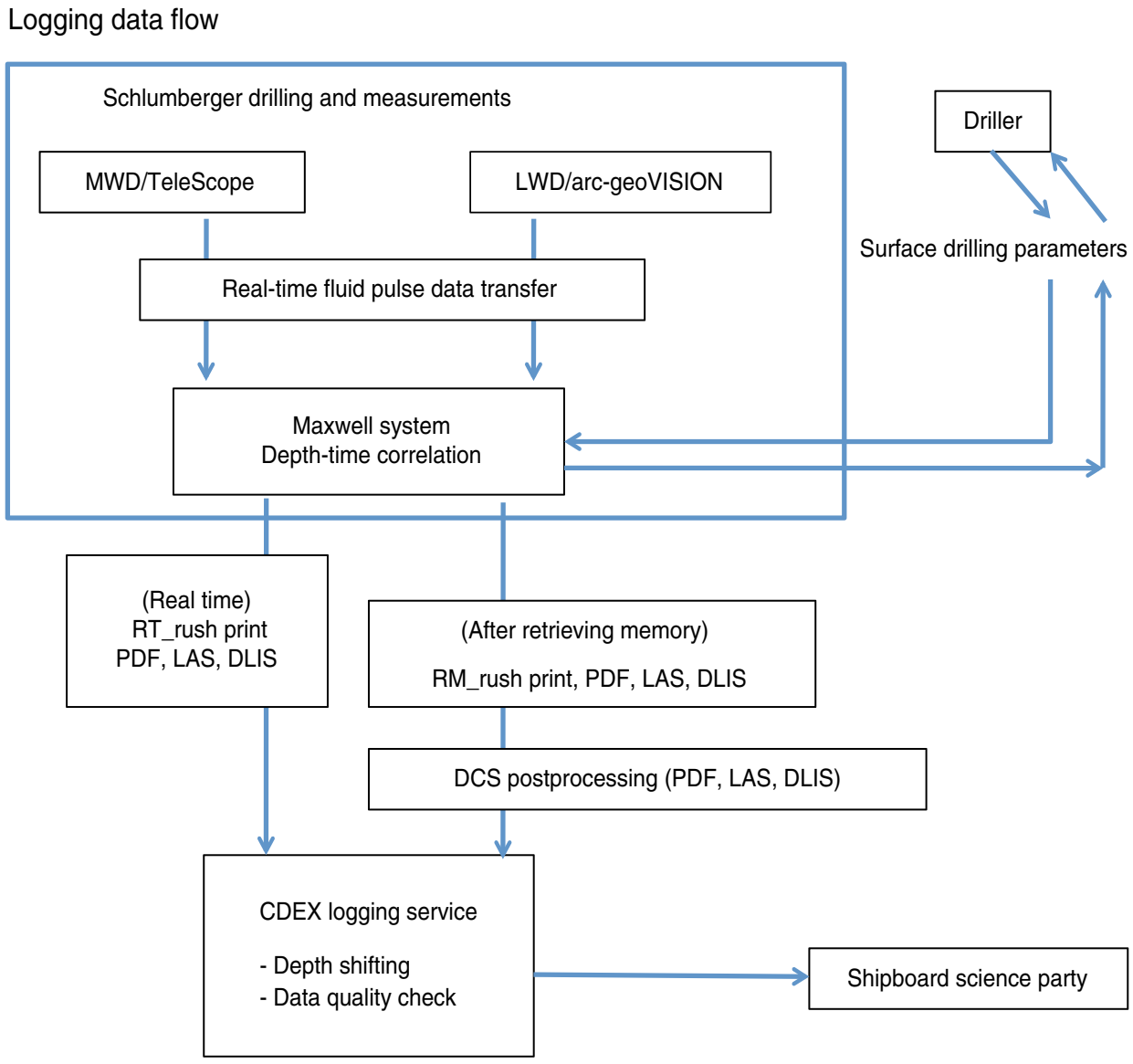

Figure F7. Classification scheme for sedimentary rocks based on proportions of siliciclastic, siliceous microfossil, and volcaniclastic lithologies, Expedition 343. Siliciclastic (terrigenous) deposit subdivision after Expedition 308 Scientists (2006), as modified from Shepard (1954). Suffix or name in parentheses indicates name for lithified equivalent, if present. Ash refers to volcaniclastic components with a grain size <4 mm.

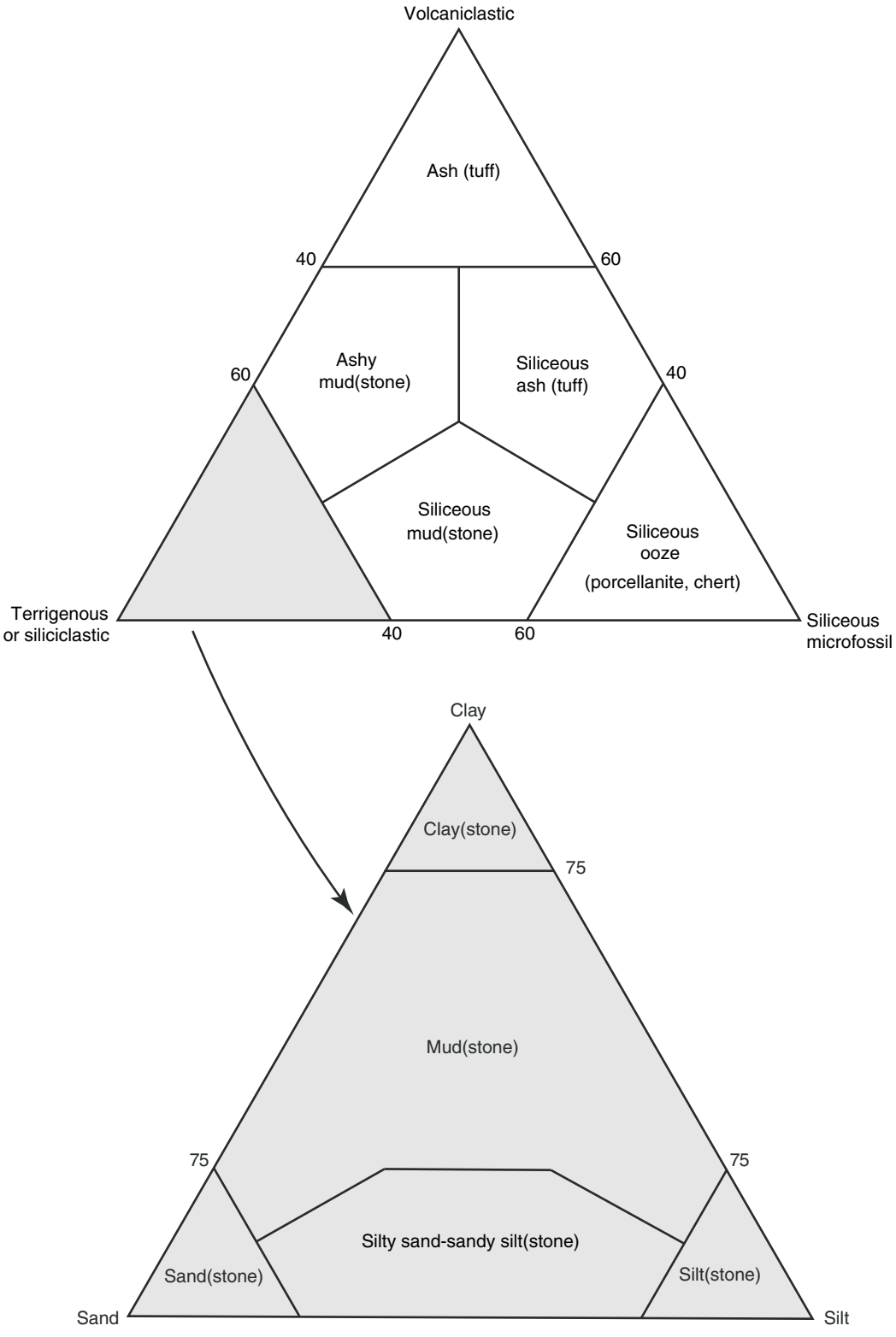

Figure F8. Graphic patterns and symbols used on visual core descriptions during Expedition 343.

Figure F9. Diagram of core reference frame for VCD and X-ray computed tomography (CT) and the xyz coordinate system used in orientation data calculations, Expedition 343. Orientations of planar features identified in X-ray CT scans can be calculated from the trend and plunge (α and β) of the lineation formed by the intersection of the plane with the slice and coronal CT images. α_1 is the angle between 000° and the intersection of the plane with the slice CT image (plane perpendicular to the core axis), and β_1 = 0°. β_2 is the plunge of the intersection of the planar feature with the coronal CT image, and α_2 = 90° or 270°.

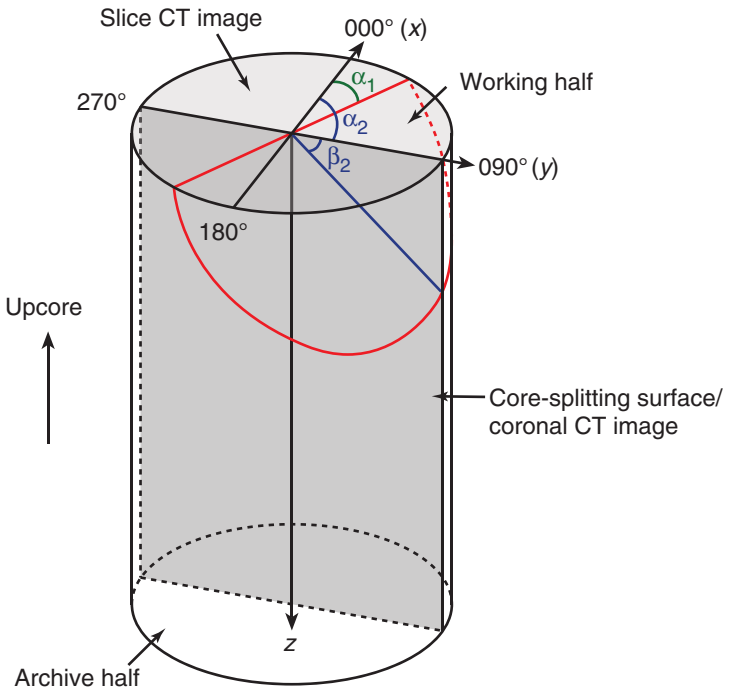

Figure F10. Log sheet used to record structural data and observations from working half of split core, Expedition 343.

Structural geology observation sheet

No.

Exp. : Site : Hole : Core : Observer : Summary:

Section no.	Structure ID	Top of struct	Bottom of struct	Avg. depth	Thickness of struct	Core face app. dip		2nd app. dip		Striation on surface		Coherent interval (for P-mag)		P-mag pole		Notes
						az.	dip	az.	dip	rake (≤90)	from (+1,90 or 2 "Top"1" Bottom	top	bottom	az./trend	dip	

Figure F11. Photograph of modified protractor used to measure apparent dips, trends, plunges, and rakes on planar and linear features in a split core, Expedition 343.

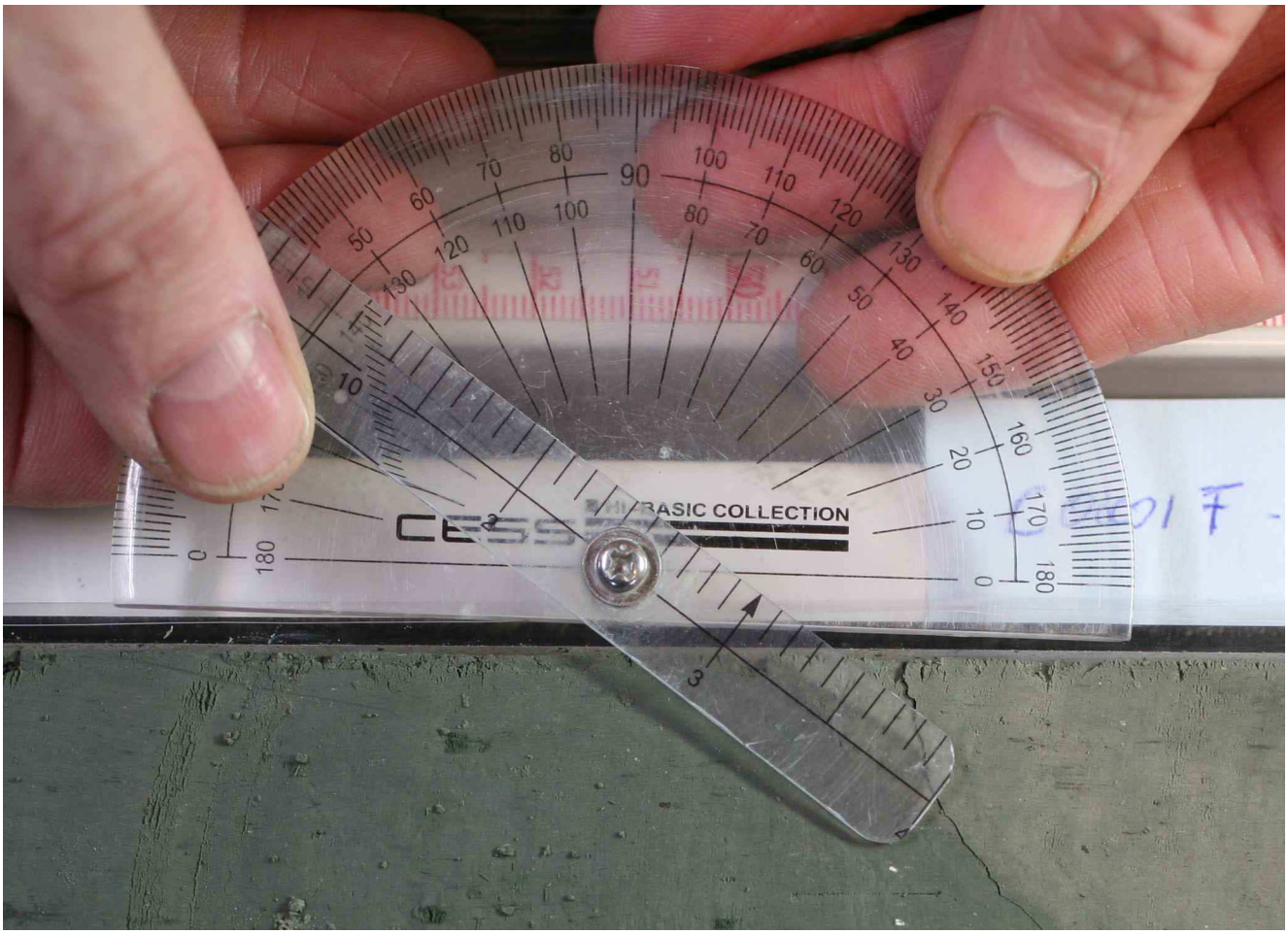

Figure F12. Layout of the spreadsheet used for recording and calculating orientation data, Expedition 343.

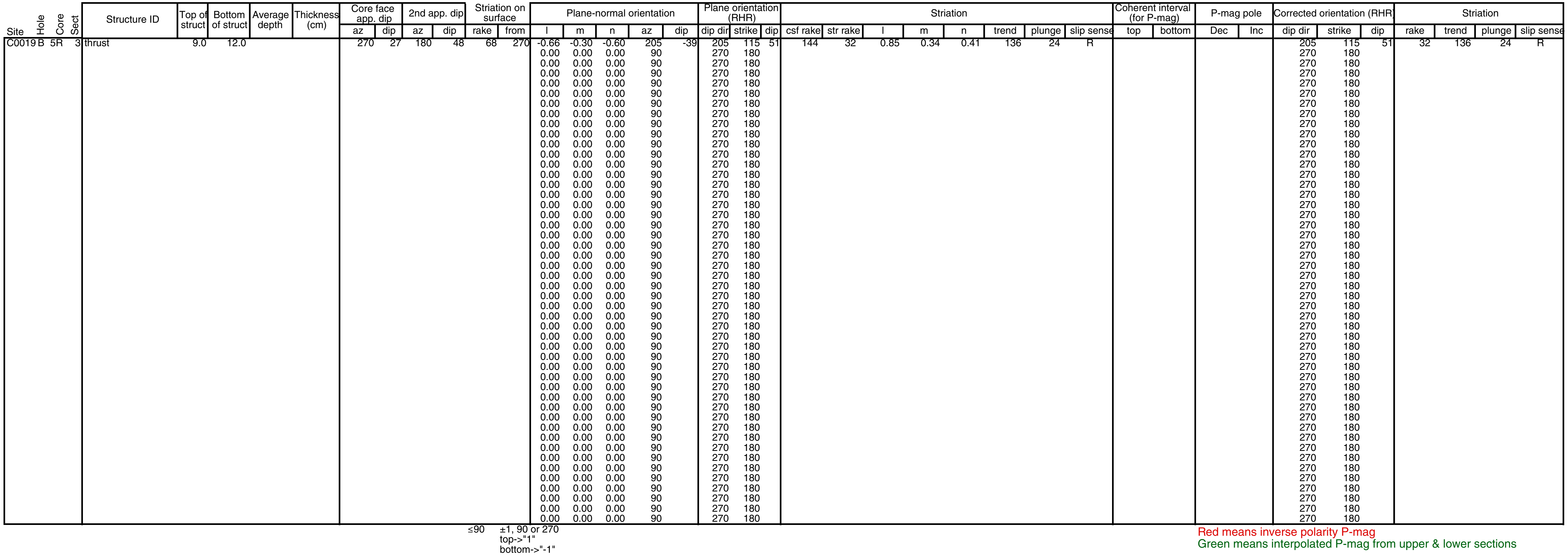

Site	Hole	Core	Sect	Structure ID	Top of struct	Bottom of struct	Average depth	Thickness (cm)	Core face app. dip		2nd app. dip		Striation on surface		Plane-normal orientation					Plane orientation (RHR)			Striation								Coherent interval (for P-mag)		P-mag pole		Corrected orientation (RHR)			Striation			
									az	dip	az	dip	rake	from	l	m	n	az	dip	dip dir	strike	dip	csf rake	str rake	l	m	n	trend	plunge	slip sense	top	bottom	Dec	Inc	dip dir	strike	dip	rake	trend	plunge	slip sense
C0019	B	5R	3	thrust	9.0	12.0			270	27	180	48	68	270	-0.66	-0.30	-0.60	205	-39	205	115	51	144	32	0.85	0.34	0.41	136	24	R					205	115	51	32	136	24	R
															0.00	0.00	0.00	90		270	180														270	180					
															0.00	0.00	0.00	90		270	180														270	180					
															0.00	0.00	0.00	90		270	180														270	180					
															0.00	0.00	0.00	90		270	180														270	180					
															0.00	0.00	0.00	90		270	180														270	180					
															0.00	0.00	0.00	90		270	180														270	180					
															0.00	0.00	0.00	90		270	180														270	180					
															0.00	0.00	0.00	90		270	180														270	180					
															0.00	0.00	0.00	90		270	180														270	180					
															0.00	0.00	0.00	90		270	180														270	180					
															0.00	0.00	0.00	90		270	180														270	180					
															0.00	0.00	0.00	90		270	180														270	180					
															0.00	0.00	0.00	90		270	180														270	180					
															0.00	0.00	0.00	90		270	180														270	180					
															0.00	0.00	0.00	90		270	180														270	180					
															0.00	0.00	0.00	90		270	180														270	180					
															0.00	0.00	0.00	90		270	180														270	180					
															0.00	0.00	0.00	90		270	180														270	180					
															0.00	0.00	0.00	90		270	180														270	180					
															0.00	0.00	0.00	90		270	180														270	180					
															0.00	0.00	0.00	90		270	180														270	180					
															0.00	0.00	0.00	90		270	180														270	180					
															0.00	0.00	0.00	90		270	180														270	180					
															0.00	0.00	0.00	90		270	180														270	180					
															0.00	0.00	0.00	90		270	180														270	180					
															0.00	0.00	0.00	90		270	180														270	180					
															0.00	0.00	0.00	90		270	180														270	180					
															0.00	0.00	0.00	90		270	180														270	180					
															0.00	0.00	0.00	90		270	180														270	180					
															0.00	0.00	0.00	90		270	180														270	180					
															0.00	0.00	0.00	90		270	180														270	180					
															0.00	0.00	0.00	90		270	180														270	180					
															0.00	0.00	0.00	90		270	180														270	180					
															0.00	0.00	0.00	90		270	180														270	180					
															0.00	0.00	0.00	90		270	180														270	180					
															0.00	0.00	0.00	90		270	180														270	180					
															0.00	0.00	0.00	90		270	180														270	180					
															0.00	0.00	0.00	90		270	180														270	180					
															0.00	0.00	0.00	90		270	180														270	180					
															0.00	0.00	0.00	90		270	180														270	180					
															0.00	0.00	0.00	90		270	180														270	180					
															0.00	0.00	0.00	90		270	180														270	180					
															0.00	0.00	0.00	90		270	180														270	180					
															0.00	0.00	0.00	90		270	180														270	180					
															0.00	0.00	0.00	90		270	180														270	180					
															0.00	0.00	0.00	90		270	180														270	180					
															0.00	0.00	0.00	90		270	180														270	180					
															0.00	0.00	0.00	90		270	180														270	180					
															0.00	0.00	0.00	90		270	180														270	180					
															0.00	0.00	0.00	90		270	180														270	180					
													≤90	±1, 90 or 270 top->"1" bottom->"-1"																											

Red means inverse polarity P-mag

Green means interpolated P-mag from upper & lower sections

Figure F13. Diagram of calculation of the orientation of a plane (shaded) from two apparent dips, Expedition 343. Intersections of split core surface and section perpendicular to split core surface and parallel to core direction with plane of interest are shown as an example. (α_1, β_1) and (α_2, β_2) = azimuths and apparent dips of traces of the plane on two sections, v_1 and v_2 = unit vectors parallel to traces of the plane on two sections, v_n = unit vector normal to plane.

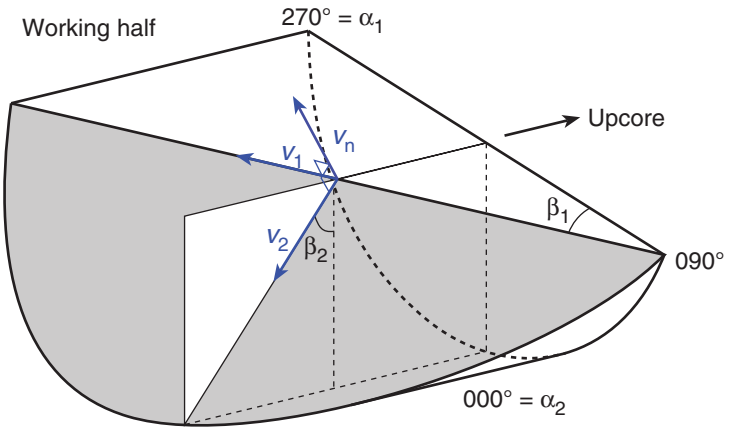

Figure F14. Diagrams of dip direction (α_d), right-hand rule strike (α_s), and dip (β) of a plane deduced from its normal azimuth (α_n) and dip (β_n), Expedition 343. **A.** $\beta_n < 0°$. **B.** $\beta_n \geq 0°$. v_n = unit vector normal to plane.

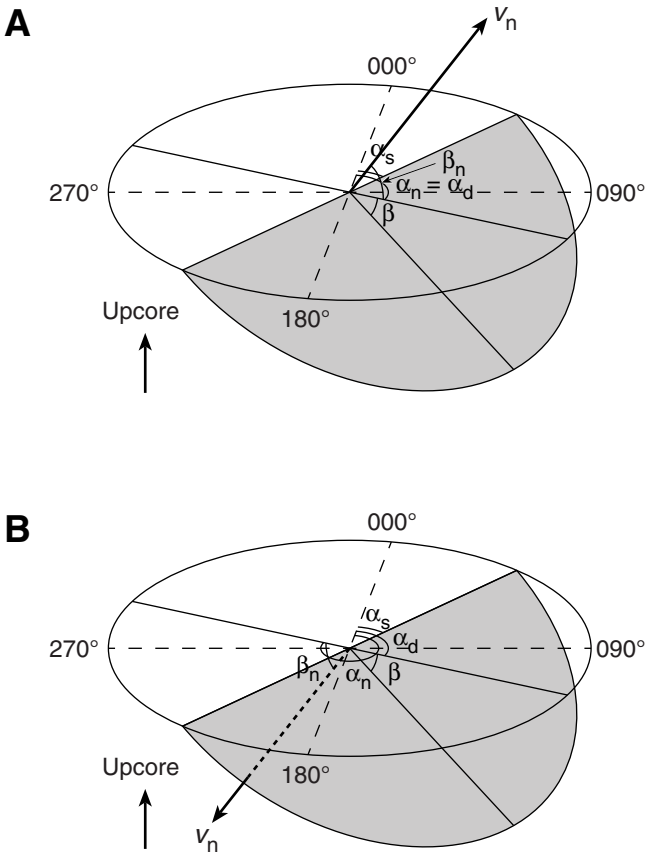

Figure F15. Diagram of apparent rake measurement of slickenlines on a fault surface from 270° direction of split core surface trace, Expedition 343. ϕ_a = apparent rake, v_n = unit vector normal to fault plane, v_c = unit vector normal to split core surface, v_i = unit vector parallel to the intersection line between fault plane and split core surface.

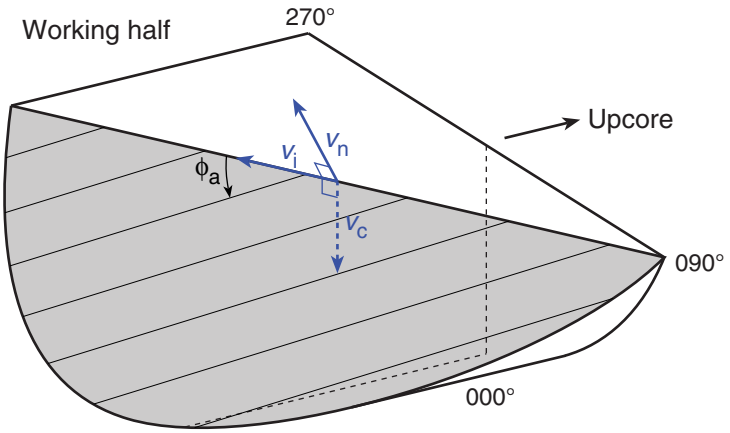

Figure F16. Diagrams of rake of slickenlines (ϕ) deduced from the rake of intersection line between fault plane and split core surface (ϕ_i) and apparent rake measured (ϕ_a), Expedition 343. **A.** ϕ_a from top or 90° direction where fault plane dips toward 270°. **B.** ϕ_a from bottom or 90° direction where fault plane dips toward 90°. **C.** ϕ_a from top or 270° direction where fault plane dips toward 90°. **D.** ϕ_a from bottom or 270° direction where fault plane dips toward 270°. α_s = right-hand rule strike of fault plane, v_n = unit vector normal to fault plane, v_c = unit vector normal to split core surface, v_i = unit vector parallel to intersection line between fault plane and split core surface, v_s = horizontal unit vector in the right-hand rule strike direction of fault plane.

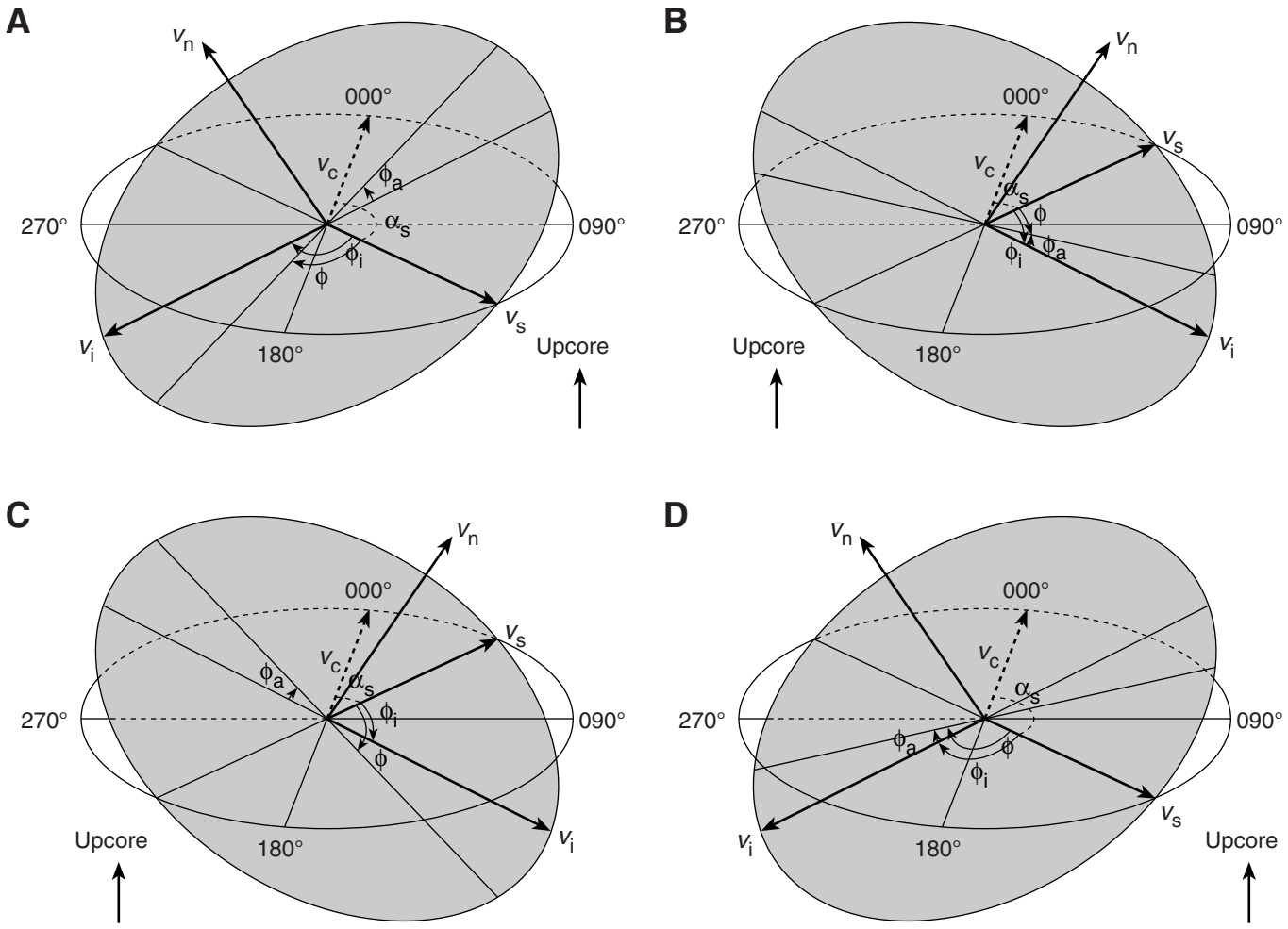

Figure F17. Diagrams of azimuth correction based on paleomagnetic data, Expedition 343. **A.** Paleomagnetic inclination $\beta_p \geq 0°$. **B.** $\beta_p < 0°$. α_p = paleomagnetic declination, α_d and α_s = dip direction and right-hand rule strike of a plane.

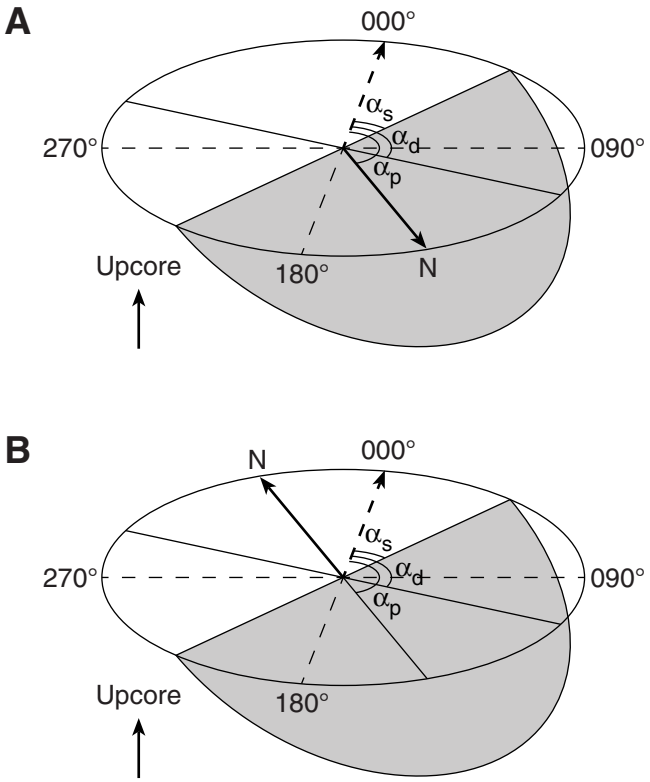

Figure F18. Example of structural geology window in J-CORES visual core description program, Expedition 343. Fault data are entered in two ways: fault and slickenline data separately or fault data including slickenline parameters as a comment.

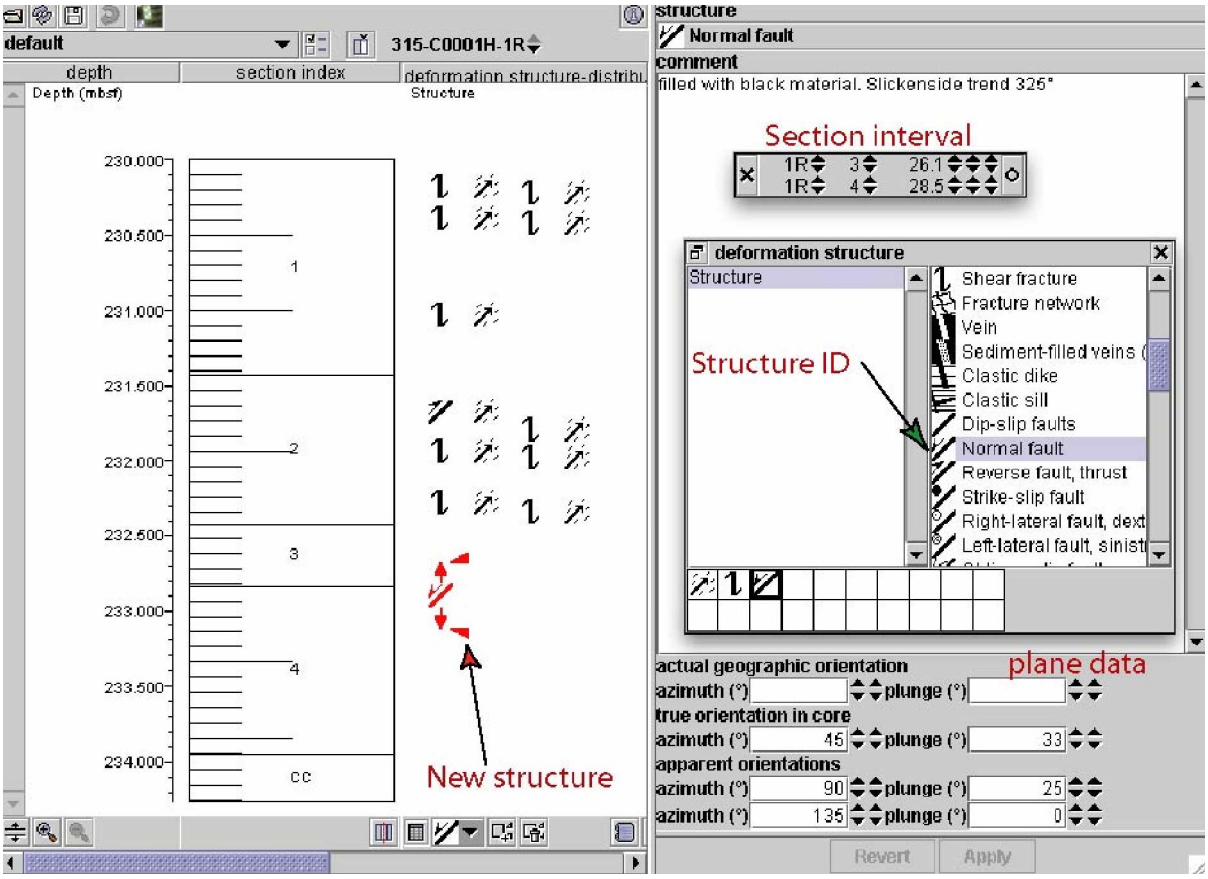

Figure F19. Diagram of orientation system of cores, discrete samples, and superconducting rock magnetometer used during Expedition 343. SQUID = superconducting quantum interference device.

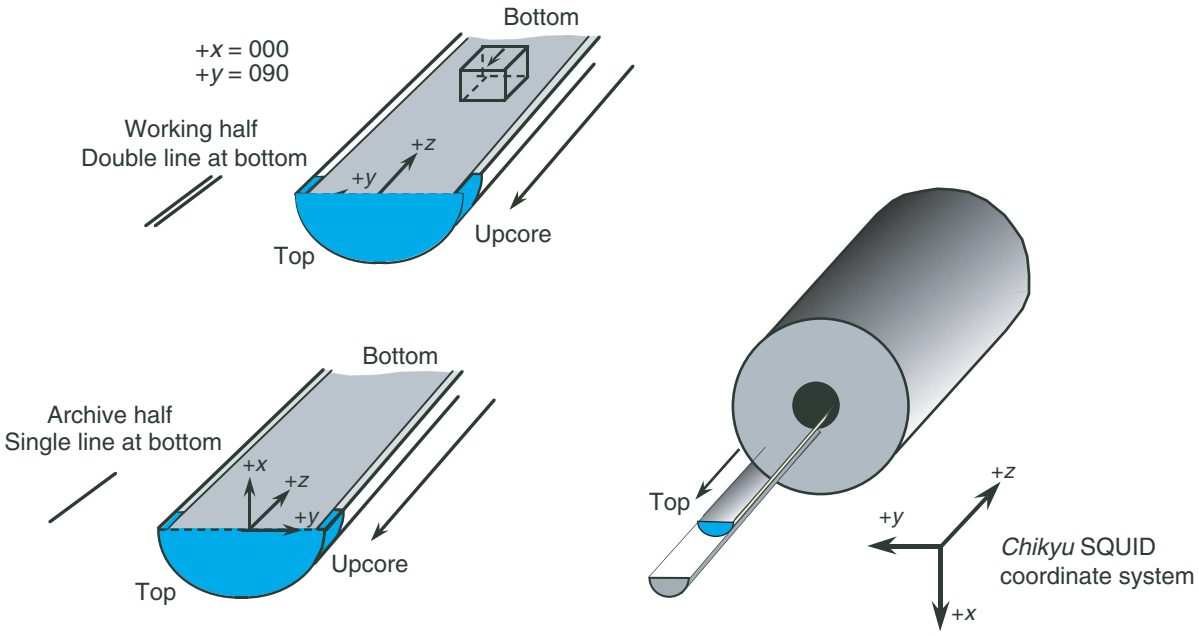

Figure F20. Sketch of core reference frame used in physical properties sampling, Expedition 343.

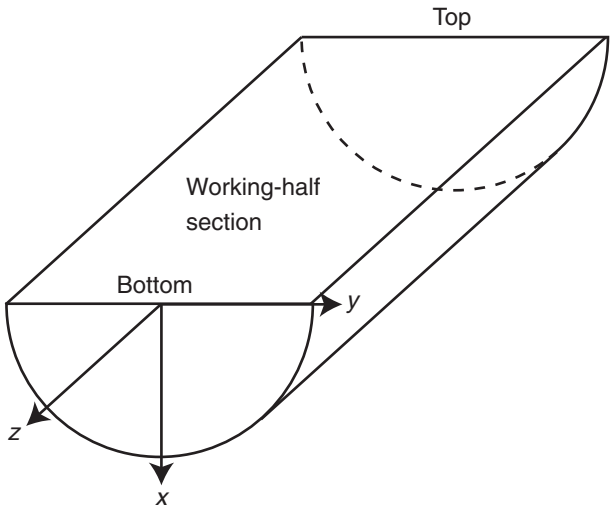

Figure F21. Photographs of the observatory MTL string and components, Expedition 343T. **A.** An RBR being attached to a rope splice, Expedition 343T. The black rubber covering beneath the MTL is wrapped around the rope and MTL for protection. **B.** Antares sensors outside of their coverings waiting to be reprogrammed. The sensors are slipped back into their red coverings and sealed with tape for deployment. **C.** All 55 MTL sensors. The RBRs are the larger ones in the foreground and the Antrares the smaller ones. **D.** An RBR on the rope in its protective covering. **E.** Bottom of the MTL sensor string showing, from right to left, the sinker bar, a covered RBR sensor, a weak link, and a covered Antares sensor.

Figure F22. Diagram of casing hanger wellhead at the top of the miniature temperature logger (MTL) observatory with the removable hanger and hanger ring from which the MTL sensor string hangs, Expedition 343T. The remotely operated vehicle (ROV) *Kaiko* will grab hold of the hanger ring to remove the sensor string and recover the data recorded within each MTL.

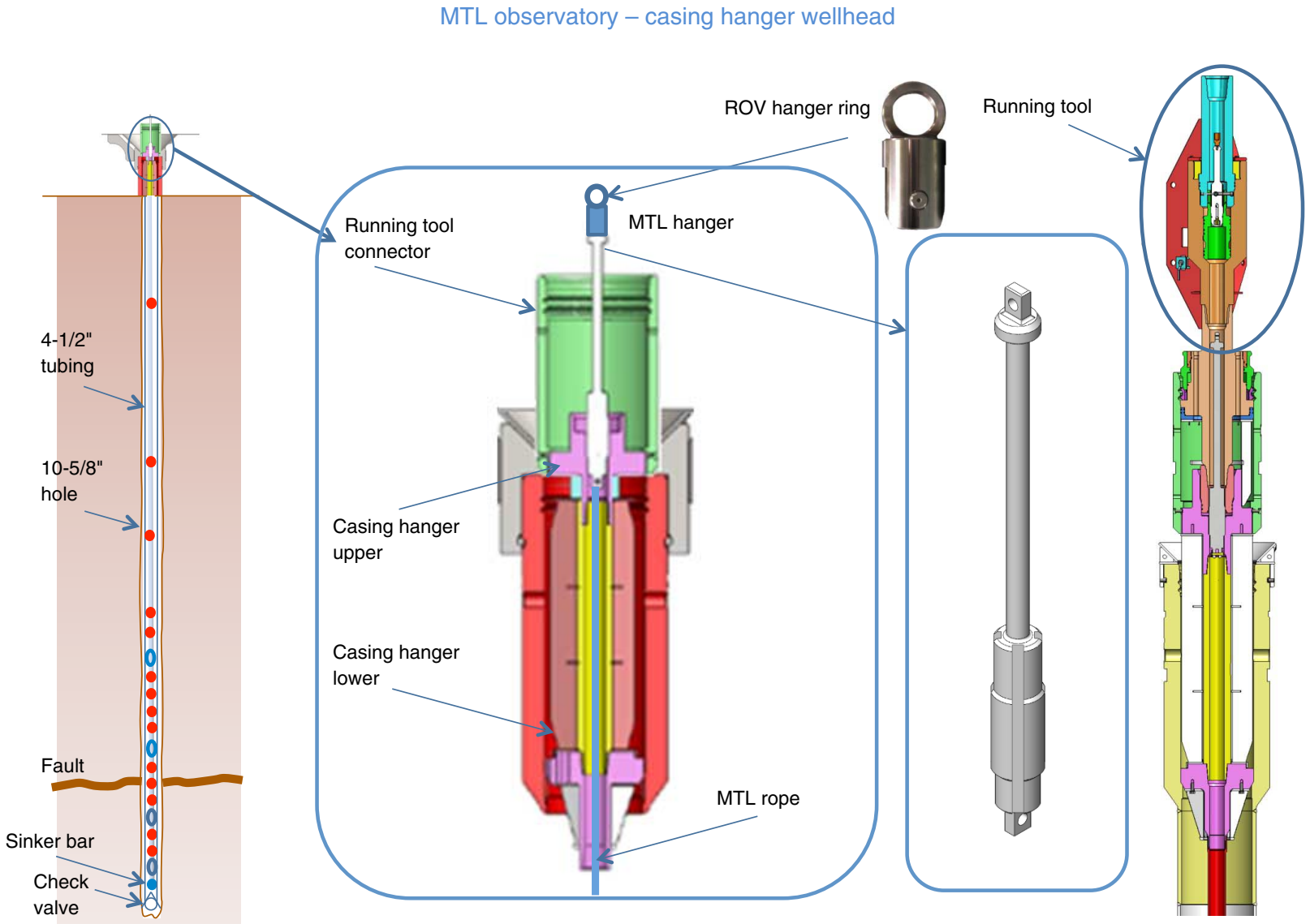

Figure F23. Diagram and positions of the lower portion of the miniature temperature logger (MTL) observatory, Expedition 343T. A corresponding photograph of the lower part of the sensor string is shown in Figure **F21E.** TD = total depth. Locations of the lowermost sensors are shown as yellow dots.

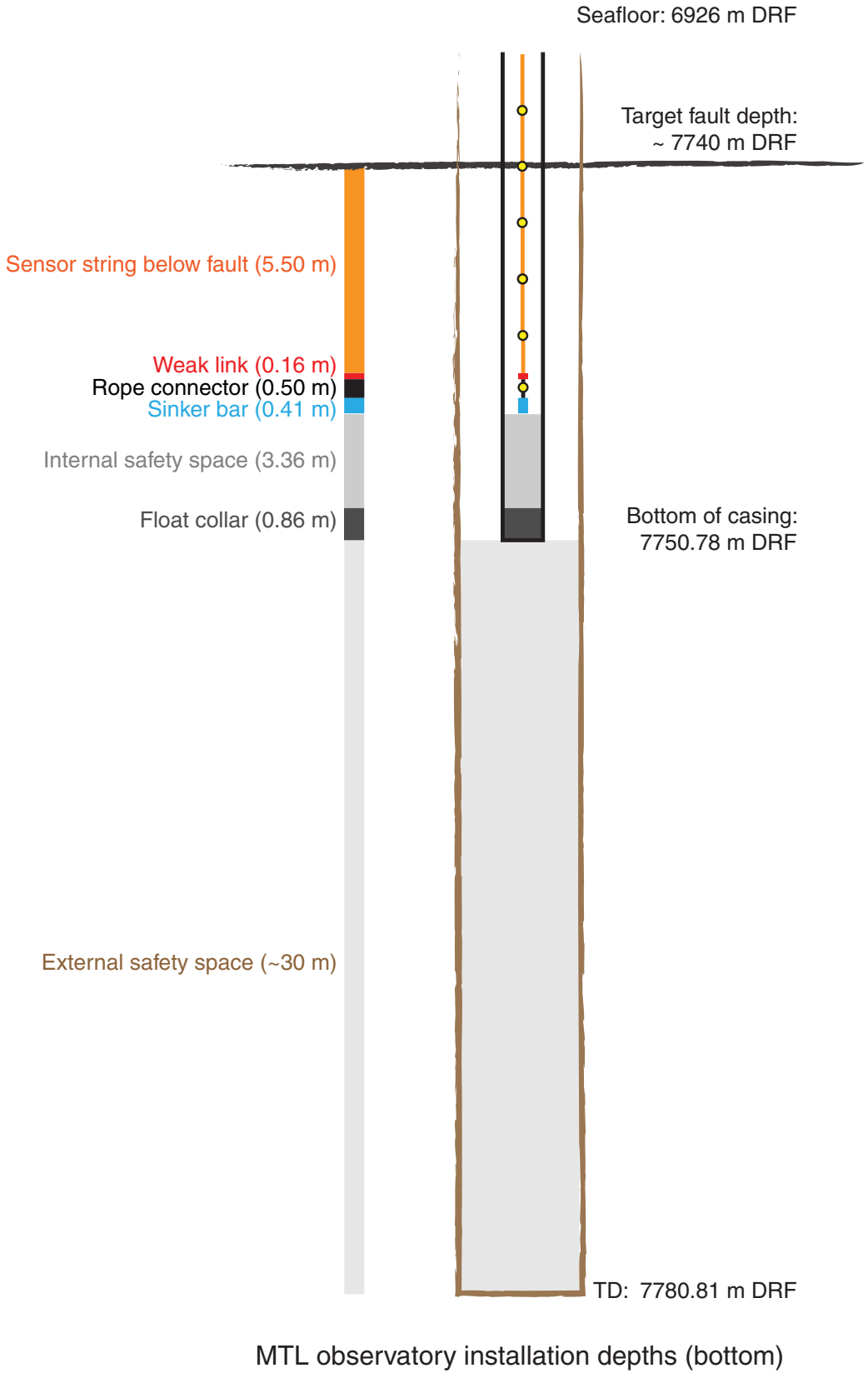

Figure F24. Photographs of the free-fall MTL installation and retrieval, Expedition 343T. **A.** Free-fall MTL string ready for installation in the core barrel. **B.** Free-fall MTL string placed in the bottom of an empty core liner and installed in the core barrel. **C.** Closing the core barrel with a deplugger nozzle. **D.** A TDR-2050s instrument after being taken out of the rubber covering following deployment and retrieval. The image highlights the connecting cord loops between instrument and rubber covering and between covering sleeves.

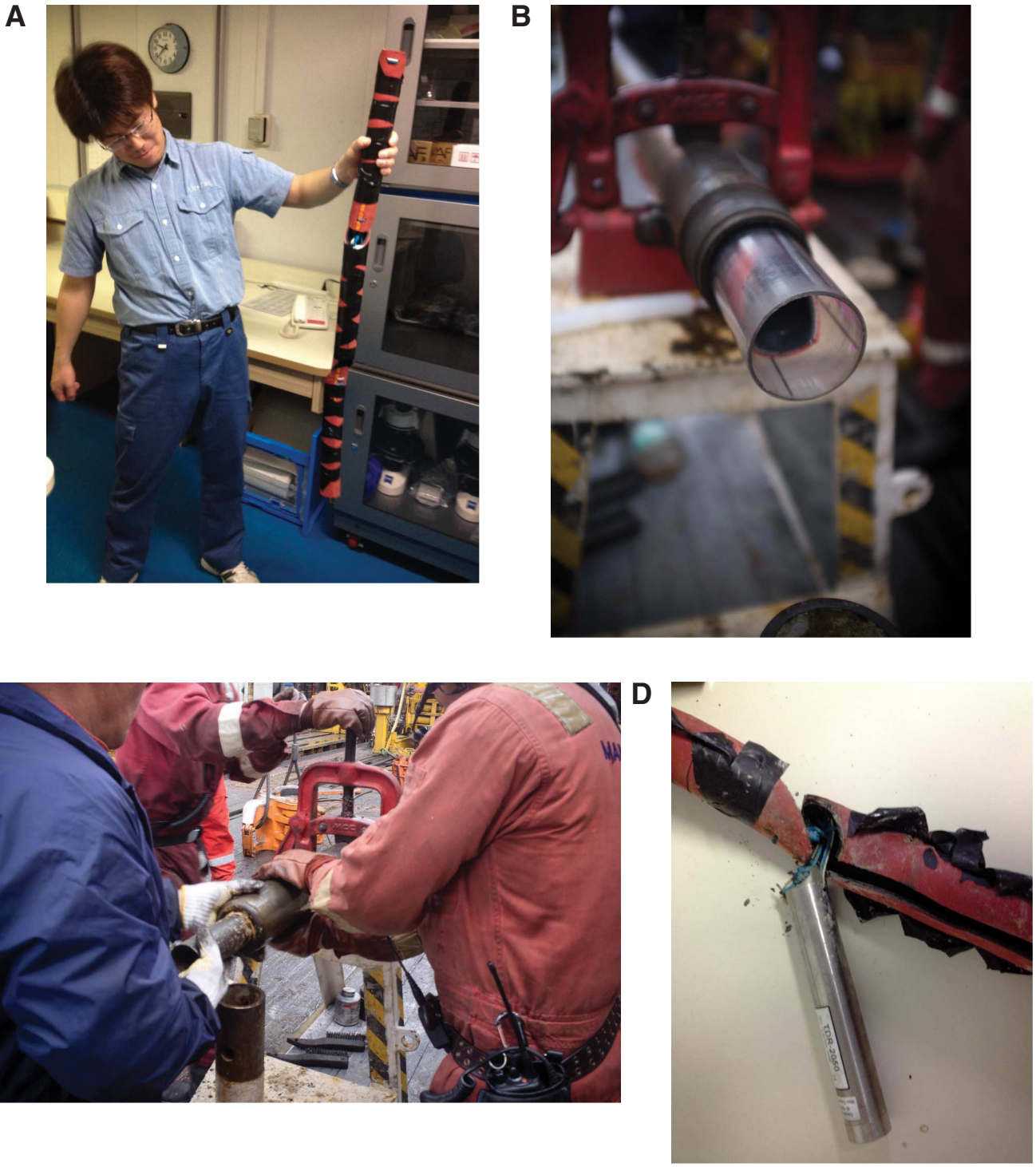

Table T1. BHA configuration, Expedition 343.

Component	Description	OD (inch)	ID (inch)	Max OD (inch)	Length (m)	Cumulative length (m)
1	8-1/2 inch Smith PDC bit	6.000	2.250	8.500	0.25	0.25
2	6-3/4 inch bit sub	6.750	3.500	6.750	0.91	1.16
3	6-3/4 inch crossover sub	6.750	2.250	6.750	0.44	1.60
4	GVR-6 2 × 8-1/4 inch stabilizers	6.750	4.880	8.250	3.07	4.67
5	arcVISION6	6.750	2.810	7.500	5.77	10.45
6	TeleScope 675	6.750	5.109	6.890	8.52	18.97
7	Nonmagnetic drill collar	6.688	2.813	6.688	8.12	27.09
8	8-1/4 inch OD stabilizer	6.500	2.500	8.250	1.75	28.84
9	Crossover	6.750	2.250	6.750	1.52	30.36

OD = outside diameter, ID = inside diameter. PDC = polycrystalline diamond compact, GVR = geoVISION resistivity.

Table T2. MWD-APWD tool acronyms, descriptions, and units, Expedition 343. (Continued on next page.)

Tool	Output	Description	Unit
Surface		Drilling parameters	
	BD	Bit depth	m
	TD	Total depth	m
	HKLD	Hook load	kkgf
	ROP	Rate of penetration	m/h
	WOB	Surface weight on bit	kkgf
	TRQ	Power swivel torque	kNm
	HPS	Power swivel speed	rpm
	FR	Flow-in	L/m
MWD		Measurement while drilling	
	RGX	Rotating axial accelerometer	rpm
	RHX	Rotating axial magnetometer	rpm
	A_JAM	Anti-jam counter	
	TUR_RPM	Turbine rotation	rpm
	SHOCK	Shock counter	
	CRPMS	Average MWD collar rotation	rpm
	STICKNSLIP	Peak-to-peak collar rotation	rpm
APWD/arcVISION real-time		Annular pressure while drilling/Array resistivity tool	
	APRS	Annular pressure	kPa
	ATMP	Annular temperature	°C
	CRPM	Average collar rotation	rpm
	ECD	Equivalent circulating density	g/cm^3
	INCL_CONT	Continuous inclination (hole deviation)	Degrees
	AZIM_CONT	Continuous hole azimuth	Degrees
	SHKRSK	Shock risk	
	SPPA	Surface pumpout pressure	kPa
	STICKNSLIP	Peak-to-peak slimpulse stick-slip	rpm
	STUCK	Time stuck	%
arcVISION memory		Array resistivity tool	
	DHAP	Downhole annular pressure	kPa
	DHAT	Downhole annular temperature	°C
	ECD	Equivalent circulating density	g/cm^3
geoVISION real-time		geoVISION resistivity tool	
	GR_RAB_RT	Natural gamma radiation	gAPI
	RES_RING_RT	Ring resistivity	Ωm
	RES_BIT_RT	Bit resistivity	Ωm
	RES_BS_RT	Shallow button resistivity	Ωm
	RES_BM_RT	Medium button resistivity	Ωm
	RES_BD_RT	Deep button resistivity	Ωm
	RB_RT		Degrees
	HAZI_RT	Hole azimuth from well survey	Degrees
	DEVI_RT	Hole deviation from well survey	Degrees

Table T2 (continued).

Tool	Output	Description	Unit
	SHK_RAB_TRANS_RT	Transverse shock	—
	SHK_RAB_AX_RT	Axial shock	—
geoVISION memory		geoVISION resistivity tool	
	GR	Total natural gamma radiation	gAPI
	GR_IMG	Total natural gamma radiation image	gAPI
	RES_RING	Ring resistivity	Ωm
	RES_BIT	Bit resistivity	Ωm
	RES_BS	Shallow button resistivity	Ωm
	RES_BM	Medium button resistivity	Ωm
	RES_BD	Deep button resistivity	Ωm
	RES_BS_IMG	Shallow button resistivity image	Ωm
	RES_BM_IMG	Medium button resistivity image	Ωm
	RES_BD_IMG	Deep button resistivity image	Ωm
	TAB_RAB_BS	Shallow button resistivity time after bit	s
	TAB_RAB_BM	Medium button resistivity time after bit	s
	TAB_RAB_BD	Deep button resistivity time after bit	s
	AZIM	Measured azimuth from well survey	Degrees
	P1AZ	Pad 1 azimuth in horizontal plane (0 = true north)	Degrees
	P1NO	Pad 1 azimuth in horizontal orthogonal to tool axis (0 = true north)	Degrees
	ROP5	Rate of penetration averaged over the last 5 ft (1.5 m)	Degrees
	P1NO	Pad 1 rotation relative to north azimuth	Degrees
	TAB_GR	Gamma ray time after bit	h
	TAB_RES_BIT	Bit resistivity time after bit	h
	TAB_RES_RING	Ring resistivity time after bit	h
	TAB_RES_BS	Shallow button resistivity time after bit	h
	TAB_RES_BM	Medium button resistivity time after bit	h
	TAB_RES_BD	Deep button resistivity time after bit	h
	RPM	Rotational speed	rpm
	SHKL_AXL	Axial shock level	
	SHKL_RAD	Radial shock level	

Table T3. Measurement performance specifications of the arcVISION, Expedition 343.

Measurement	Transmitter-receiver spacing (inch)					Transmitter-receiver spacing (inch)					Accuracy (%, mS/m)	Range (Ωm)
	16	22	28	34	40	16	22	28	34	40		
R = 1.0 Ωm	Depth of investigation (radius, inch)					Vertical resolution (ft)						
Phase shift resistivity at 2 MHz	13	14	15	17	18	0.7	0.7	0.7	0.7	0.7	±2, ±0.3	0.2–60/60–3000
Phase shift resistivity at 400 kHz	17	19	22	25	27	1	1	1	1	1	±2, ±2.0	0.1–10/10–100
Attenuation resistivity at 2 MHz	19	22	24	26	29	1.8	1.8	1.8	1.8	1.8	±3, ±1.5	0.2–25/25–50
Attenuation resistivity at 400 kHz	27	30	33	36	38	3	3.5	4	4	4	±3, ±10	0.1– 3/3–10
R = 10.0 Ωm	Depth of investigation (radius, inch)					Vertical resolution (ft)						
Phase shift resistivity at 2 MHz	18	22	25	28	30	1	1	1	1	1		
Attenuation shift resistivity at 2 MHz	31	34	36	38	40	4	5	6	6	6		

Table T4. Measurement performance specifications of the arcVISION gamma ray LWD tools, Expedition 343.

Specification	Unit	Value
Measurement range	API	0–250
Accuracy	%	±3
Vertical resolution	Inch	6
Statistical repeatability	gAPI	±2 at 100 gAPI and 100 ft/h, 3 point average

Table T5. Measurement performance specifications of the geoVISION, Expedition 343.

Measurement	Vertical resolution (inch)	Depth of investigation (inch)	Diameter of investigation (inch)		Horizontal resolution (inch)		Midpoints of extremes (inch)
			R_t/R_{xo} = 10	R_t/R_{xo} = 0.1	R_t/R_{xo} = (10 × π)/56	R_t/R_{xo} = (0.1 × π)/56	
Resistivity at the bit	12–24*	12	32	32			
Ring resistivity	2–3	7	22	25			
Button resistivity							
Shallow focused	2–3	1	19	24	1.07	1.35	1.2
Medium focused	2–3	3	15	21	0.84	1.18	1
Deep focused	2–3	5	11	16	0.62	0.9	0.75
Gamma radiation	12	10					

* = depends on bit subs. Vertical penetration rate: m/h = 30, inches/h = 1371.6, inches/min = 22.86. At a penetration rate of 30 m/h and typical rotation rate (e.g., 50 rpm) we are oversampling vertically. R_t = true resistivity of formation, R_{xo} = resistivity of zone invaded by drilling fluid. If invasion is minimal because of measuring resistivity soon after cutting of hole, then R_t/R_{xo} = 1. Resistivity of our drilling fluid, seawater, is 0.19 Ωm. Formation resistivity is ~0.4–0.6 Ωm. Horizontal resolution for each of tools intermediate between extremes of R_t/R_{xo} in table above. Imaging tools record 56 times with each revolution of tool. Accuracy of segment location is ±1°.

Table T6. Shipboard XRF (TATSCAN-F2) results for standard JSd-2 and JB-1b.

	JSd-2	Na_2O	MgO	Al_2O_3	SiO_2	P_2O_5	S	K_2O	CaO	TiO_2	MnO	Fe_2O_3
Reference value	Without S:	2.6	2.9	12.9	63.6	0.1		1.2	3.8	0.6	0.1	12.2
	With S:	2.5	2.8	12.7	62.7	0.1	1.4	1.2	3.8	0.6	0.1	12.0
	Average:	1.5	2.3	11.8	63.5	0.7		1.5	4.0	0.8	0.2	13.8
	STD (2σ, n = 5):	0.7	0.1	0.8	0.5	0.1		0.1	0.2	0.1	0.0	0.9

STD = standard deviation.

Table T6 (continued).

	JB-1b	Na_2O	MgO	Al_2O_3	SiO_2	P_2O_5	S	K_2O	CaO	TiO_2	MnO	Fe_2O_3
Reference value	Without S:	2.7	8.3	14.7	52.2	0.3	0	1.3	9.8	1.3	0.2	9.2
	With S:	2.7	8.3	14.7	52.2	0.3	0.001	1.3	9.8	1.3	0.2	9.2

Table T7. Settings for the X-ray CT scanner, Expedition 343.

Parameter	Setting
Scan type	Helical-full-0.6 s
Interval (mm)	0.625
Gantry tilt	S0.0
SFOV	Small
Tube voltage (kV)	120
Tube current (mA)	100
Detector rows	16
Helical thickness (mm)	0.625
Pitch	0.562:1
Speed	5.62
DFOV (cm)	9.6
R/L center (mm)	R0.0
A/P center (mm)	A0.0
Recon type	Detail
Matrix type	512
Recon option	Full
Auto apps	Off

Protocol name = IODP-liner version 100622. SFOV = scan field of view, DFOV = dual field of view. R/L center = distance right or left of the center line, A/P center = distance anterior or posterior of the center line.

Table T8. Shipboard and shore-based chemical analyses conducted on interstitial water based on the volume of interstitial water collected from each whole-round core sample, Expedition 343.

Sample code:	IWIC						IWICP			343TIIW
	Shipboard						Shipboard			Shore-based
Type of analysis:	Refractive index	pH/Alk	Cl	NH_4	PO_4	IC anion	IC cation	ICP-AES	ICP-MS	Li, B, Sr, and Pb isotopes
Shore-based investigator:										Ishikawa
Volume and container:										4 mL HDPE, add HCl
>55 (mL)*	0.1†	3	0.2	0.2	0.2	0.02	0.01	1	1	2
50	0.1	3	0.2	0.2	0.2	0.02	0.01	1	1	2
45	0.1	3	0.2	0.2	0.2	0.02	0.01	1	1	2
40	0.1	3	0.2	0.2	0.2	0.02	0.01	1	1	2
35	0.1	3	0.2	0.2	0.2	0.02	0.01	1	1	2
30	0.1	3	0.2	0.2	0.2	0.02	0.01	1	1	2
25	0.1	3	0.2	0.2	0.2	0.02	0.01	1	1	2
20	0.1	3	0.2	0.2	0.2	0.02	0.01	1	1	2
15	0.1	3	0.2	0.2	0.2	0.02	0.01	1	1	2
10	0.1		0.2	0.2	0.2	0.02	0.01	1	1	2
5			0.1	0.1	0.1	0.01	0.005	0.5	0.5	1
2			0.1	0.1	0.1	0.01	0.005	0.5		0.5
1			0.1	0.1	0.1	0.01	0.005			0.5

* = range of possible interstitial volumes recovered (mL), † = volume of water used in each analysis (mL), ‡ = used the residue after pH/alkalinity measurement. Blank cells = not analyzed because of insufficient sample volume. IC = ion chromatography, ICP-AES/MS = inductively coupled plasma–atomic emission spectroscopy/mass spectrometry, DOC = dissolved organic carbon, DIC = dissolved inorganic carbon, REE = rare earth elements, HDPE = high-density polyethylene.

Table T8 (continued).

Sample code:	343KTIWC	343KTIWN	343KTIWSO	343JSIWO	343JSIWC	343JSIWRE	
	Shore-based						
Type of analysis:	$\delta^{13}C$ (DOC and acetate)	δN (NH_4 and NO_x)	δS^{33-36} (SO_4 and H_2S)	$\delta^{18}O$ and δD	$\delta^{13}C$ (DIC)	REE	
Shore-based investigator:	Takai	Takai	Takai	Sample	Sample	Sample	
Volume and container:	Septum screw-lid glass vial, add $HgCl_2$ and sulfamic acid	4 mL HDPE, add HCl and $HgCl_2$	Septum screw-lid glass vial, add $ZnCl_2$, frozen	2 mL septum screw-lid glass vial (1 or 0.5 mL for smaller samples)	2 mL septum screw-lid glass vial, add $HgCl_2$	8 mL HDPE, add HCl	Total volume used
>55 (mL)*	‡	3	5	2	2	8	24.7
50	‡	3	5	2	2	8	24.7
45	‡	3	5	2	2	8	24.7
40	‡	3	5	2	2	8	24.7
35	‡	3	5	2	2	8	24.7
30	‡	3	5	2	2	8	24.7
25	‡	3	5	2	2	5	24.7
20	‡	3	5	2	1		18.7
15	‡	2		2	1		12.7
10		2		2	1		9.7
5				1	1		4.3
2				0.5			1.8
1				0.2			1.0

Table T9. Installed miniature temperature logger (MTL) positions and rope connections, Expedition 343T. (Continued on next page.)

Rope number	Rope label	MTL number	Marked scale position from bottom of Rope R1 (m)	Estimated depth installed corrected for stretch (mbsf)	Remarks
R7	219.11		835.96		Rope cut mark
	215.71		**832.57**	**–4.42**	**Casing hanger top**
	210		826.85	1.23	
	200		816.85	11.12	
	190		806.85	21.00	
	180		796.85	30.89	
	170		786.85	40.78	
	160		776.85	50.67	
	150		766.85	60.56	
	140		756.85	70.45	
	130		746.85	80.33	
	120		736.85	90.22	
	110		726.85	100.11	
	100		716.85	110.00	
	90		706.85	119.89	
	80		696.85	129.77	
	70		686.85	139.66	
	60		676.85	149.55	
	50		666.85	159.44	
	40		656.85	169.32	
	30		646.85	179.21	
	20		636.85	189.10	
	10		626.85	198.99	
			616.85	208.87	
R6		55	560.85	264.25	
		54	464.85	359.17	
		53	368.85	454.09	
		26	272.85	549.01	
		51	176.85	643.93	
		50	146.85	673.59	
		49	137.85	682.49	
		48	128.85	691.38	
		47	119.85	700.28	
			116.85	703.25	

Table T9 (continued).

Rope number	Rope label	MTL number	Marked scale position from bottom of Rope R1 (m)	Estimated depth installed corrected for stretch (mbsf)	Remarks
R5		46	113.85	706.21	
		45	110.85	709.18	
		44	107.85	712.15	
		43	104.85	715.11	
		42	101.85	718.08	
		41	98.85	721.04	
		40	95.85	724.01	
		39	92.85	726.97	
		37	89.85	729.94	
		35	86.85	732.90	
		33	83.85	735.87	
			83.10	736.61	
R4		31	80.85	738.83	
		29	77.85	741.80	
		27	74.85	744.77	
		25	71.85	747.73	
			71.10	748.47	
R8		36	68.80	750.80	
		34	62.35	757.31	
		30	56.40	763.32	
		28	50.35	769.43	
		52	44.35	775.49	
		32	38.50	781.40	
			36.25	783.67	
R3		24	35.50	784.41	
		23	34.00	785.90	
		22	32.50	787.38	
		21	31.00	788.86	
		20	29.50	790.34	
		19	28.00	791.83	
		18	26.50	793.31	
		17	25.00	794.79	
			24.25	795.53	Weak link (248 ± 10 kg)
R2		16	23.50	796.28	
		15	22.00	797.76	
		14	20.50	799.24	
		13	19.00	800.72	
		12	17.50	802.21	
		11	16.00	803.69	
		10	14.50	805.17	
		9	13.00	806.65	
			12.25	807.39	Weak link (166 ± 10 kg)
R1		8	11.50	808.13	
		7	10.00	809.62	
		6	8.50	811.10	
		5	7.00	812.58	
		4	5.50	814.06	
		3	4.00	815.55	
		2	2.50	817.03	
		1	1.00	818.51	
			0.00	819.50	Weak link (124 ± 5 kg)
R0		38	–0.31	819.81	
			–1.07	820.57	Sinker bar bottom
				823.93	Float collar top
				824.78	Shoe bottom